

NANOINDENTATION INVESTIGATION IN POLYMERS WITH CYLINDRICAL
CURVATURE AND PLANAR SURFACE AREA FOR ENHANCED MECHANICAL
CHARACTERIZATION

By

HINAL R. PATEL

A thesis submitted to the

School of Graduate Studies

Rutgers, The State University of New Jersey

In partial fulfillment of the requirements

For the degree of

Master of Science

Graduate Program in Mechanical and Aerospace Engineering

Written under the direction of

Assimina A. Pelegri

And approved by

New Brunswick, New Jersey

May, 2019

ABSTRACT OF THE THESIS

NANOINDENTATION INVESTIGATION IN POLYMERS WITH CYLINDRICAL CURVATURE AND PLANAR SURFACE AREA FOR ENHANCED MECHANICAL CHARACTERIZATION

by HINAL R. PATEL

Thesis Director:

Dr. Assimina A. Pelegri

Investigation of the transverse properties in anisotropic Kevlar[®] fibers are conducted via instrumented indentation methods. The K29, KM2, and K119 fibers are comprised of a skin and core with distinct indentation moduli. Indentations performed at different loads contributed ample data to obtain depth dependent indentation moduli. Indentation moduli are characterized at a depth 10% of fiber diameter to avoid effects from the substrate and additionally at the skin level, 2-13%, 7-13%, and 25-40% of fiber diameter. To account for the curvature of the single fiber, a previously developed modified curved area function was incorporated in comparison to the common flat area function extracted from the Oliver-Pharr method. The indentation moduli derived from the flat area function were undervalued than ones determined from the modified curved area function. The transverse indentation moduli of single Kevlar fibers varied at depths across their diameters. As expected from material composition, the KM2 fiber possessed the largest indentation moduli of 5.28 GPa, whereas the K119 fiber exhibited the lowest at 2.21 GPa. Two polymers of unique compositions, polydimethylsiloxane (PDMS) and shape memory polymer (SMP), are also examined for their frequency and depth dependent

mechanical properties via single and multiple cycle loading. PDMS is a hydrophobic elastomer and exhibits greater elasticity than the hydrophilic SMP, but similarities in material response were distinguished. During single cycle nanoindentation, both planar polymers exhibited smoother loading curves at the lowest frequency as opposed to the higher frequencies. At 3mN load-controlled tests, PDMS and SMP had an average indentation modulus value of 3.94 ± 0.06 MPa and 2.07 ± 0.08 GPa, respectively. Their indentation moduli differed by a factor of 525, supporting the conclusion that PDMS is physically softer than the SMP. As loads and maximum depths increased, the mechanical properties decreased for both materials.

To study periodic response behavior in both polymers, the frequencies for multiple cycle tests were varied at 1, 0.5, and 0.033 Hz for different cycles. During these small-scale fatigue tests on PDMS, 5 and 50 cycle experiments demonstrated a linear trend with a negative slope for indentation moduli, whereas 100 cycle experimental data conformed to power law curves. Contrarily, all cycles and frequencies tested on SMP followed power law curve fitting. As the frequencies decreased, the change in maximum depths increased along with a further depreciation of indentation modulus for both materials. The multiple cycle indentation tests confirmed the consistent trends identified in the single cycle indentations. Overall, the two polymers experienced comparable trends in mechanical properties despite their extensive disparity in chemical composition, indentation modulus, and hardness.

ACKNOWLEDGEMENTS

I would like to proclaim my sincere gratitude for my thesis advisor and role model, Dr. Mina Pelegri, who has generously supported and granted me the opportunity to conduct research with her since 2015 as an undergraduate student. Her words of encouragement guided me throughout my research and motivated me to obtain my MS at Rutgers University.

Additionally, I want to thank Dr. Pelegri's research group, especially Max Tenorio and Hermise Raju, for their assistance in nanoindentation whenever I needed it. I am grateful for Professor Howon Lee's research group permitting me to test and analyze their polymer specimens in conjunction for my thesis paper. Special thanks to Chen Yang for assisting with sample preparation and analysis feedback. I would also like to acknowledge my thesis committee: Prof. Mina Pelegri, Prof. Howon Lee, and Prof. Rajiv Malhotra, for their time during the defense.

Finally, I want to thank my family, especially my mother and father, for their continuous emotional and financial support. I would not be able to continue my education without their encouragement and appreciation. I am so thankful for their unconditional love and support.

TABLE OF CONTENTS

ABSTRACT OF THE THESIS	ii
ACKNOWLEDGEMENTS	iv
LIST OF TABLES	vii
LIST OF FIGURES	ix
LIST OF ACRONYMS AND SYMBOLS	xiv
Chapter 1 – INTRODUCTION	1
Chapter 2 – BACKGROUND	5
2.1 – Indentation Theory	5
2.2 – Indentation Theory for Polymers	10
2.3 – Berkovich Tip	13
2.4 – Area functions	14
Chapter 3 – EXPERIMENTAL SETUP	16
3.1 - Specimen Preparation	16
3.2 – Single and Multiple Cycle Loading Experimental Setup	18
3.3 – Table of Experiments	21
Chapter 4 – RESULTS AND DISCUSSION	24
4.1 – Indentation Moduli at 10% Kevlar Fiber Diameter	25
4.1.1 Kevlar K29 Fiber	27
4.1.2 Kevlar KM2 Fiber	30
4.1.3 Kevlar K119 Fiber	32
4.2 – Indentation Moduli at Various Percentages of Fiber Diameter	34
4.2.1 Kevlar K29 Fiber	36

4.2.2 Kevlar KM2 Fiber	38
4.2.3 Kevlar K119 Fiber	39
4.3 PDMS Experimental Results	40
4.3.1 PDMS – Single Cycle Loading	41
4.3.2 PDMS – Multiple Cycle Loading	44
4.4 SMP Experimental Results	60
4.4.1 SMP – Single Cycle Loading	60
4.4.2 SMP – Multiple Cycle Loading	66
Chapter 5 – CONCLUSION	81
APPENDICES	83
Appendix A – Kevlar 29 Supplementary Graphs	83
Appendix B – Kevlar KM2 Supplementary Graphs	85
Appendix C – Kevlar K119 Supplementary Graphs	87
Appendix D – PDMS Supplementary Graphs	89
Appendix E – SMP Supplementary Graphs	97
REFERENCES	105

LIST OF TABLES

Table 3.1: Experiments on specimens of significant curvature (Kevlar fibers).	21
Table 3.2: Experiments on polymer specimens of planar surface area and minimal surface roughness.	23
Table 3.3: Frequencies tested and their respective relationships to each other, listed as A:B ratio.	23
Table 4.1: The loads tested on three different types of fibers. The symbol (*) denotes the load tested which reached 10% of fiber diameter.	26
Table 4.2: Average indentation moduli computed from both mCAF and FAF at 10% of Kevlar fiber diameter.	26
Table 4.3: Indentation modulus computed with mCAF at skin, 2-13%, 7-13%, and 25-40% of fiber diameter for Kevlar fibers.	35
Table 4.4: Indentation modulus computed with FAF at skin, 2-13%, 7-13%, and 25-40% of fiber diameter for Kevlar fibers.	35
Table 4.5: Two nanoindentation methods listed with the load-controlled tests on PDMS.	40
Table 4.6: PDMS characterization of indentation modulus and hardness over a range of depths through 1 mm specimen thickness.	42
Table 4.7: Multiple cycle indentation load-controlled tests for PDMS at frequencies of 1, 0.5, and 0.033Hz. Each frequency test was performed with 5, 50, and 100 cycles. Each test had a corresponding maximum and minimum indentation modulus.	45
Table 4.8: Two nanoindentation methods listed with the load-controlled tests on SMP.	60

Table 4.9: SMP characterization of indentation modulus and hardness over a range of depths through 1 mm specimen thickness.	64
Table 4.10: Multiple cycle indentation load-controlled tests for SMP at frequencies of 1, 0.5, and 0.033Hz. Each frequency test was performed with 5, 50, and 100 cycles. Each test had a corresponding maximum and minimum indentation modulus.	66

LIST OF FIGURES

Figure 2.1: Nanoindentation loading and unloading curve with thermal drift collection. At the maximum load, the dwell period is included with evidence of creep behavior.	6
Figure 2.2: Stiffness is extrapolated from the slope of the unloading curve. The stiffness is used in the calculation of the reduced modulus material property.	7
Figure 2.3: Specimen profile before, during, and after loading from the indenter tip. A depression from the indenter tip is typically left after the maximum load is applied.	8
Figure 2.4: Schematic of indentation marks from Berkovich indenter with (a) pile-up, (b) no pile-up or sink-in, and (c) sink-in. The pile-up and sink-in effects can cause inaccuracies in mechanical property calculations.	11
Figure 2.5: Multiple cycle loading hysteresis curve with five cycles. Each cycle has the same frequency although the displacements between the cycles may vary.	12
Figure 2.6: The Berkovich indenter tip with a face half angle of 65.3° . The indenter tip is made of diamond with a three-sided pyramidal geometry.	13
Figure 2.7: Circled in red is an indent made by the Berkovich indenter. Its size is in the same order of magnitude of the Kevlar fiber diameter; thus, incorporation of fiber curvature is paramount to the accuracy of measurements.	14
Figure 3.1: The single Kevlar fiber was carefully hang between two notches where the adhesive was applied. In order for the steel washers to hang freely, pliers were utilized to suspend the SEM puck stem on the edge of a table.	17
Figure 3.2: The pendulum components from the low load head in the Vantage. The depth-sensing capacitor and electromagnetic coils provide precise control of the load and	

depth. The balance weight is used for load calibration, which needs to be done whenever the pendulum is removed from the low load head.	19
Figure 3.3: SMP mounted on Vantage in front of the Berkovich indenter.	20
Figure 4.1: Indentation moduli from the mCAF measured at indentation depth equal to 10% of the fiber diameter.	27
Figure 4.2: SEM picture of K29 fiber before treatment in denatured alcohol. The fiber has a rough surface, which is clearly visible.	28
Figure 4.3: Kevlar K29 single cycle nanoindentation at (a) 3mN (6 curves) and (b) 5mN (6 curves) with respect to a depth of 10% fiber diameter.	29
Figure 4.4: SEM picture of KM2 fiber with clear distinction of a smoother surface than the K29 fiber.	31
Figure 4.5: Kevlar KM2 single cycle nanoindentation at 5mN (7 curves) with respect to a depth of 10% fiber diameter.	32
Figure 4.6: SEM picture of KM2 fiber with clear distinction of a smoother surface than the K29 fiber.	33
Figure 4.7: Kevlar K119 single cycle nanoindentation at 5mN (4 curves) with respect to a depth of 10% fiber diameter.	34
Figure 4.8: K29 indentation modulus at various percentages of fiber diameter.	37
Figure 4.9: KM2 indentation modulus at various percentages of fiber diameter.	39
Figure 4.10: K119 indentation modulus at various percentages of fiber diameter.	40
Figure 4.11: PDMS single cycle nanoindentation at (a) 1mN (8 curves), (b) 2mN (10 curves), (c) 3mN (10 curves), and (d) 4mN (10 curves).	41

Figure 4.12: Behavior of PDMS indentation modulus across a range of average maximum depths.	43
Figure 4.13: Behavior of PDMS hardness across a range of average maximum depths.	44
Figure 4.14: PDMS multiple cycle nanoindentation at 1mN and 5 cycles with varying frequencies of (a) 1Hz (5 curves), (b) 0.5Hz (5 curves), (c) 0.033Hz (5 curves).	46
Figure 4.15: PDMS indentation modulus graphs at 1mN with various frequencies at (a) 5 cycles, (b) 50 cycles, and (c) 100 cycles.	48
Figure 4.16: PDMS indentation modulus graphs at 1mN with various cycles at (a) 1Hz, (b) 0.5Hz, and (c) 0.033Hz.	49
Figure 4.17: PDMS hardness graphs at 1mN with various frequencies at (a) 5 cycles, (b) 50 cycles, and (c) 100 cycles.	50
Figure 4.18: PDMS hardness graphs at 1mN with various cycles at (a) 1Hz, (b) 0.5Hz, and (c) 0.033Hz.	51
Figure 4.19: PDMS indentation modulus graphs at 2mN with various frequencies at (a) 5 cycles, (b) 50 cycles, and (c) 100 cycles.	52
Figure 4.20: PDMS indentation modulus graphs at 2mN with various cycles at (a) 1Hz, (b) 0.5Hz, and (c) 0.033Hz.	53
Figure 4.21: PDMS hardness graphs at 2mN with various frequencies at (a) 5 cycles, (b) 50 cycles, and (c) 100 cycles.	54
Figure 4.22: PDMS hardness graphs at 2mN with various cycles at (a) 1Hz, (b) 0.5Hz, and (c) 0.033Hz.	55
Figure 4.23: PDMS indentation modulus graphs at 3mN with various frequencies at (a) 5 cycles, (b) 50 cycles, and (c) 100 cycles.	56

Figure 4.24: PDMS indentation modulus graphs at 3mN with various cycles at (a) 1Hz, (b) 0.5Hz, and (c) 0.033Hz.	57
Figure 4.25: PDMS hardness graphs at 3mN with various frequencies at (a) 5 cycles, (b) 50 cycles, and (c) 100 cycles.	58
Figure 4.26: PDMS hardness graphs at 3mN with various cycles at (a) 1Hz, (b) 0.5Hz, and (c) 0.033Hz.	59
Figure 4.27: SMP single cycle nanoindentation at (a) 2mN (9 curves), (b) 3mN (8 curves), (c) 4mN (6 curves), and (d) 5mN (7 curves).	61
Figure 4.28: SMP single cycle nanoindentation at (a) 10mN (5 curves), (b) 20mN (10 curves), (c) 30mN (10 curves), and (d) 50mN (9 curves).	62
Figure 4.29: SMP single cycle nanoindentation at (a) 100mN (6 curves), (b) 200mN (10 curves), (c) 250mN (10 curves), and (d) 300mN (8 curves).	63
Figure 4.30: Behavior of SMP indentation modulus across a range of average maximum depths.	65
Figure 4.31: Behavior of SMP hardness across a range of average maximum depths. ...	65
Figure 4.32: SMP multiple cycle nanoindentation at 3mN and 5 cycles with varying frequencies of (a) 1Hz (7 curves), (b) 0.5Hz (7 curves), (c) 0.033Hz (7 curves).	67
Figure 4.33: SMP indentation modulus graphs at 3mN with various frequencies at (a) 5 cycles, (b) 50 cycles, and (c) 100 cycles.	69
Figure 4.34: SMP indentation modulus graphs at 3mN with various cycles at (a) 1Hz, (b) 0.5Hz, and (c) 0.033Hz.	70
Figure 4.35: SMP hardness graphs at 3mN with various frequencies at (a) 5 cycles, (b) 50 cycles, and (c) 100 cycles.	71

Figure 4.36: SMP hardness graphs at 3mN with various cycles at (a) 1Hz, (b) 0.5Hz, and (c) 0.033Hz.	72
Figure 4.37: SMP indentation modulus graphs at 10mN with various frequencies at (a) 5 cycles, (b) 50 cycles, and (c) 100 cycles.	73
Figure 4.38: SMP indentation modulus graphs at 10mN with various cycles at (a) 1Hz, (b) 0.5Hz, and (c) 0.033Hz.	74
Figure 4.39: SMP hardness graphs at 10mN with various frequencies at (a) 5 cycles, (b) 50 cycles, and (c) 100 cycles.	75
Figure 4.40: SMP hardness graphs at 10mN with various cycles at (a) 1Hz, (b) 0.5Hz, and (c) 0.033Hz.	76
Figure 4.41: SMP indentation modulus graphs at 50mN with various frequencies at (a) 5 cycles, (b) 50 cycles, and (c) 100 cycles.	77
Figure 4.42: SMP indentation modulus graphs at 50mN with various cycles at (a) 1Hz, (b) 0.5Hz, and (c) 0.033Hz.	78
Figure 4.43: SMP hardness graphs at 50mN with various frequencies at (a) 5 cycles, (b) 50 cycles, and (c) 100 cycles.	79
Figure 4.44: SMP hardness graphs at 50mN with various frequencies at (a) 1Hz, (b) 0.5Hz, and (c) 0.033Hz.	80

LIST OF ACRONYMS AND SYMBOLS

PDMS	Polydimethylsiloxane
SMP	Shape memory polymer
BMA	Benzyl methacrylate
BPA	Bisphenol A ethoxylate dimethacrylate
FEM	Finite element method
P_{max}	Maximum load
h_{max}	Maximum depth
S	Stiffness
P	Load
h	Depth
A	Contact area
H	Hardness
m	Dimensionless constant for power law curve fitting
α	Dimensionless constant for power law curve fitting
h_f	Final indentation depth
h_c	Contact depth
ε	Geometric constant for the indenter tip
E_r	Reduced modulus
β	Beta factor for the indenter tip
$A(h_c)$	Contact area as a function of contact depth
E_s	Indentation modulus of specimen
ν_s	Poisson's ratio of specimen

ν_i	Poisson's ratio of indenter tip
Y	Initial yield stress
E	Elastic modulus
FAF	Flat area function
d	Average diameter
mCAF	Modified curved area function
$A_{mCAF}(h_c)$	Modified curved area function as a function of contact depth
DMA	Dynamic mechanical analysis

Chapter 1 – INTRODUCTION

Polymers have viscoelastic properties and distinct mechanical behavior that further deviate from ceramics and metals. Remarkably, they also have the foremost applications in 3D printing, military equipment, aeronautical, and automotive equipment. In the present study, three types of polymers are investigated: Kevlar fibers, polydimethylsiloxane (PDMS), and shape memory polymer (SMP), for their extensive capabilities in commercial applications. The nanoindentation instrumented method is employed on these materials to further understand their response behavior emerging from unique polymer structures under localized stress.

Kevlar is the trade name of a para-aramid high strength [1] synthetic material, typically produced in the form of fibers. It is a versatile material used in both military grade and commercial applications. The high-performance fiber exhibits a liquid–crystalline behavior originating from a solution synthesizing process of 1,4-phenylenediamine (para-phenylenediamine) and terephthaloyl chloride monomers, and a mechanical process that orients its polymeric chains to different degrees depending on the post-processing conditions [2]. For example, the high tensile strength [1] of spun Kevlar develops from the hydrogen bonds that form between the carbonyl groups and the NH roots. Controlled variations of these synthesizing processes lead to different grades of Kevlar that exhibit distinct stiffness, elongation, strength, and physical structures.

Specifically, Kevlar K29 [2] enjoys targeted industrial applications, such as sheathing of cable wires, tire and vehicle armor reinforcement. While, both K29 and KM2 fibers are used in the manufacturing of body armor, KM2 displays superior ballistic resistance and is the preferred material for warfighter protection systems [2]. Kevlar

K119 is incorporated into clothing to protect against abrasions and heat. Fatigue resistant K119 fibers elongate significantly and are a viable material for protective clothing [2]. Overall, the practical application of Kevlar, for both military and commercial uses, confirms the need for continued research on the deformation of individual fibers as they are exposed to concentrated forces.

As a well-known elastomer, PDMS, exhibits rubbery elasticity and is commonly used in contact lenses [4] and biomechanical devices due to its nonbiodegradability [3]. This material's unique viscoelastic properties are correlated with the combination of silicone compounds and polymeric chains [3]. PDMS is incredibly soft, even the slightest force causes major deformations. Conventionally, this material is a baseline comparison with polymer behavior because of its chemical and mechanical stability and low loss modulus [5].

The smart material, SMP, conforms temporarily upon external forces until an external stimulus, such as heat, causes the polymer to restore its original form [6]. This mechanical restoration response is a unique attribute of SMPs. Urinary catheters and orthopedic braces require materials like SMPs that designate the medical device as mendable and custom fit for a patient [7, 8]. Ge's research group studied 4D printing applications with SMPs in manufacturing of polymer grippers and springs [9]. These mechanical tools adjust to a variety of sizes and prove crucial in systems that require soft materials to maintain form. Yang et al. further investigated the viability of shock absorbance on SMPs for aerospace structures and biomedical devices [10]. Evidently, SMPs provide an extensive list of medical and commercial applications.

Experimental and computational techniques have been proposed to explore the complex behavior and mechanical response of polymers. Compression and indentation tests are few of the numerous methods employed to understand material behavior. Indentation testing evaluates the indentation moduli of specimen at specified loads and depths. Pressure from applied load is localized on the contact area between the specimen and indenter tip. Meanwhile, compression testing relies on globally deforming the specimen to find stress and strain relations. The procedure is generally performed with two flat plates pushing together on both sides of the specimen to induce elastic deformation. The stress is globalized on the surface area of the specimen that is in contact with the plates. The specimen may yield causing plastic deformation and ultimately lead to fracture in both testing methods if loads are increased. These methods offer valid techniques for measuring mechanical properties of polymers and their unconventional behavior.

Depth-sensing techniques are incorporated in nanoindentation to track indenter tip depth during experimentation [11, 12]. The contact area between the indenter tip and the specimen is calculated from the contact depth. Typically, most specimens tested with nanoindentation have a planar surface area with small variations in surface roughness. Two polymers, PDMS and SMP, with planar surface area are mechanically tested with nanoindentation in the present study to characterize their behavior with frequency and cyclic dependency. Specimens with significant curvature, such as Kevlar fibers, are additionally tested and studied using area correction factors determined from finite element method (FEM) [13].

McAllister, Gillespie, VanLandingham, Cole, Strawhecker, Bencomo-Cisneros, Tejeda-Ochoa, García-Estrada, Herrera-Ramírez, Hurtado-Macías, Martínez-Sánchez, and Herrera-Ramírez have similarly tested Kevlar's mechanical performance via nanoindentation testing methods [14, 15, 16, 17]. However, their analysis lacked a proper area correction function. Likewise, Kawabata, Wollbrett-Blitz, Joannès, Bruant, Le Clerc, De La Osa, Bunsell, and Marcellan [18, 19] employed compression testing on single Kevlar fibers to calculate their elastic modulus. Mechanical response, specifically for Kevlar, from these two testing methods are compared with the findings from the newly identified area correction factor. Although compression tests are a distinct method of determining the elastic modulus of a material, they provide adequate comparisons to the indentation modulus. The indentation modulus and elastic modulus are equivalent in most materials where pile-up and sink-in are not present [20]. Caution must be taken when comparing the same mechanical property measured from indentation and compression testing because the specimens are distinctly compressed in each method.

Carillo's research group analyzed the wet and fully cured states of PDMS via nanoindentation testing [21]. Their research group additionally studied the different variations between base to crosslinker ratios. The indentation moduli differences between cracked and pristine PDMS elastomers was studied by Maji's research group examined with nanoindentation [22]. The present study of PDMS nanoindentation is compared to these literature reports. Subsequently, the mechanical behavior of PDMS is additionally compared to the newly formulated SMP specimen as a baseline comparison for polymer behavior. Although these two polymers have distinct differences in softness, their comparison provides further insight in material strength and applications.

Chapter 2 – BACKGROUND

2.1 – Indentation Theory

Indentation measurements rely on an applied load and contact depth between the tip and the specimen to determine hardness and indentation modulus. This applied load on the specimen results in elastic-plastic deformation that depends on the material properties, load, and the depth. During the process of a single indent, the user inputs either a maximum load or depth for the indenter tip to apply on a small specimen. Small volume specimens are typically tested via nanoindentation at the sub-micron scale. The indentations completed on thin films must provide that the indentation depth does not surpass 10% of the specimen thickness to avoid the substrate effect [23]. The substrate effect can influence the indentation modulus measurements and cause them to deviate from their true values.

During the indentation test, the indenter tip applies a load on the specimen at a single point and unloads after it reaches the maximum load. Each indent corresponds to a loading and unloading curve (Fig. 2.1) and provides information of the maximum load, P_{max} , and the maximum depth, h_{max} . It also displays the dwell period, or the holding time, when the indenter tip reaches the maximum load. During the dwell period, creep takes place in the material and is physically represented by the increase of depth as the load remains constant. A small holding time may lead to little or no creep depending on the material [24]. Located on the unloading curve, the thermal drift correction exhibits creep behavior and measures the change in thermal effects as the depth decreases and the load is held constant. It is crucial to collect thermal drift data because the material may exhibit

different pre-indentation and post-indentation conditions due to friction, energy loss, and environmental changes [25].

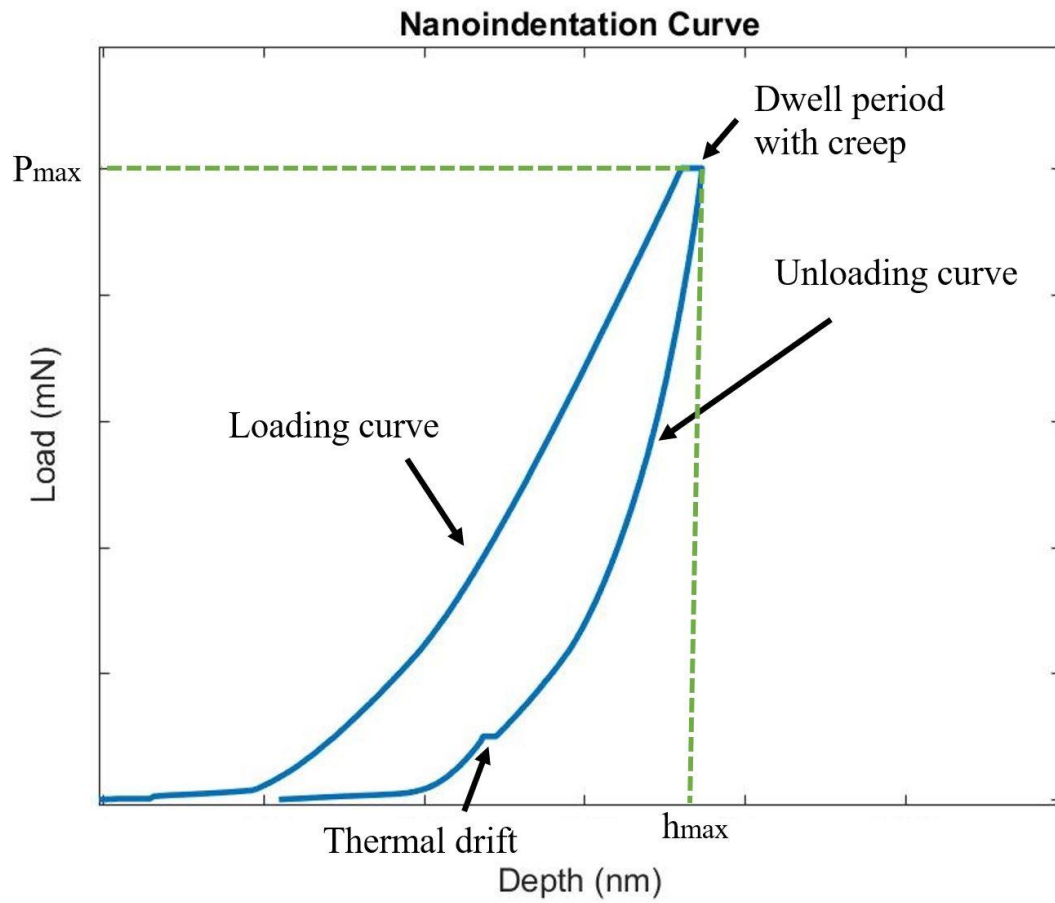


Figure 2.1: Nanoindentation loading and unloading curve with thermal drift collection. At the maximum load, the dwell period is included with evidence of creep behavior.

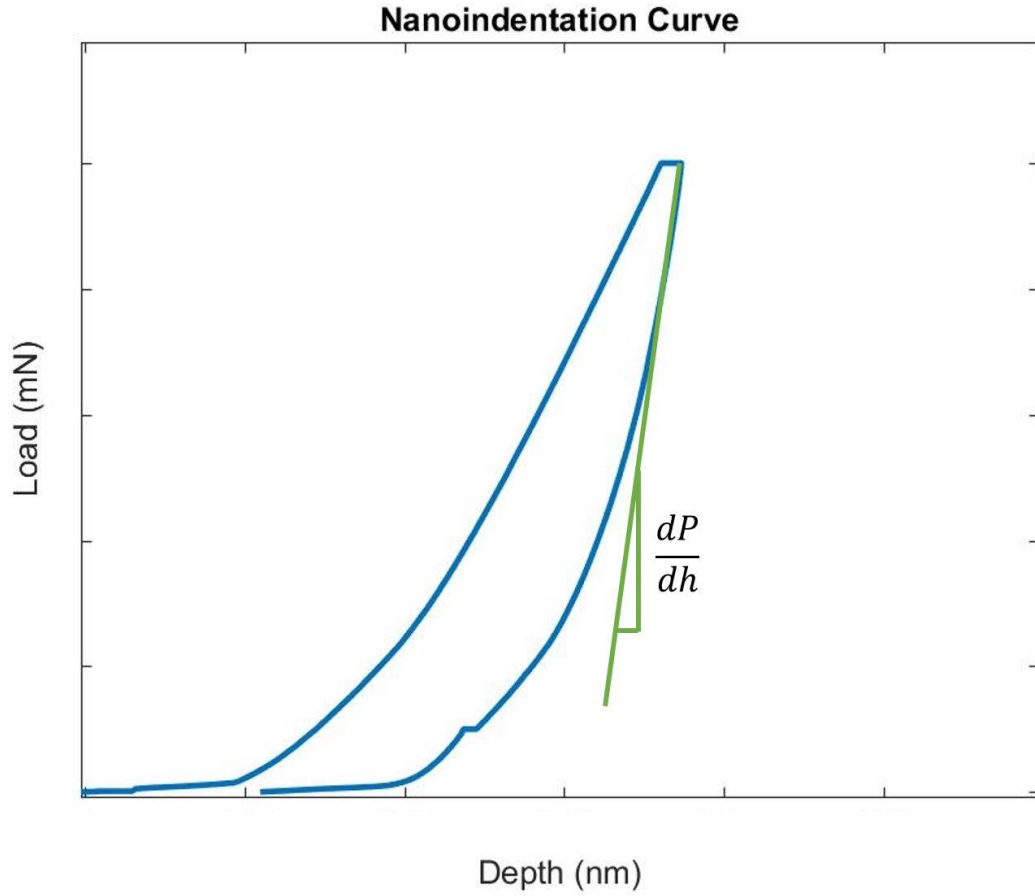


Figure 2.2: Stiffness is extrapolated from the slope of the unloading curve. The stiffness is used in the calculation of the reduced modulus material property.

The most common methods governing indentation theory are Oliver-Pharr [26] and Doerner-Nix [27]. Regarding these methods, the slope of the unloading curve is equal to the stiffness, S , of the specimen at the indentation location (Fig. 2.2). The formula for the stiffness in terms of the load, P , and the indentation depth, h , is expressed as

$$S = \frac{dP}{dh} \quad (1)$$

The hardness, H , is calculated with the maximum load and the contact area, A from

$$H = \frac{P_{max}}{A} \quad (2)$$

The specimen is assumed to be completely flat and comparable to a semi-infinite plane in both Oliver-Pharr [26] and Doerner-Nix [27] analysis. During an experiment, the indenter tip depresses the specimen surface and an indent mark is formed (Fig. 2.3). Typically, higher loads and indentation depths are correlated with larger contact areas and indent sizes. Ultimately, indent size yielded from the localized plastic deformation process depends on the maximum depth, load, and material properties.

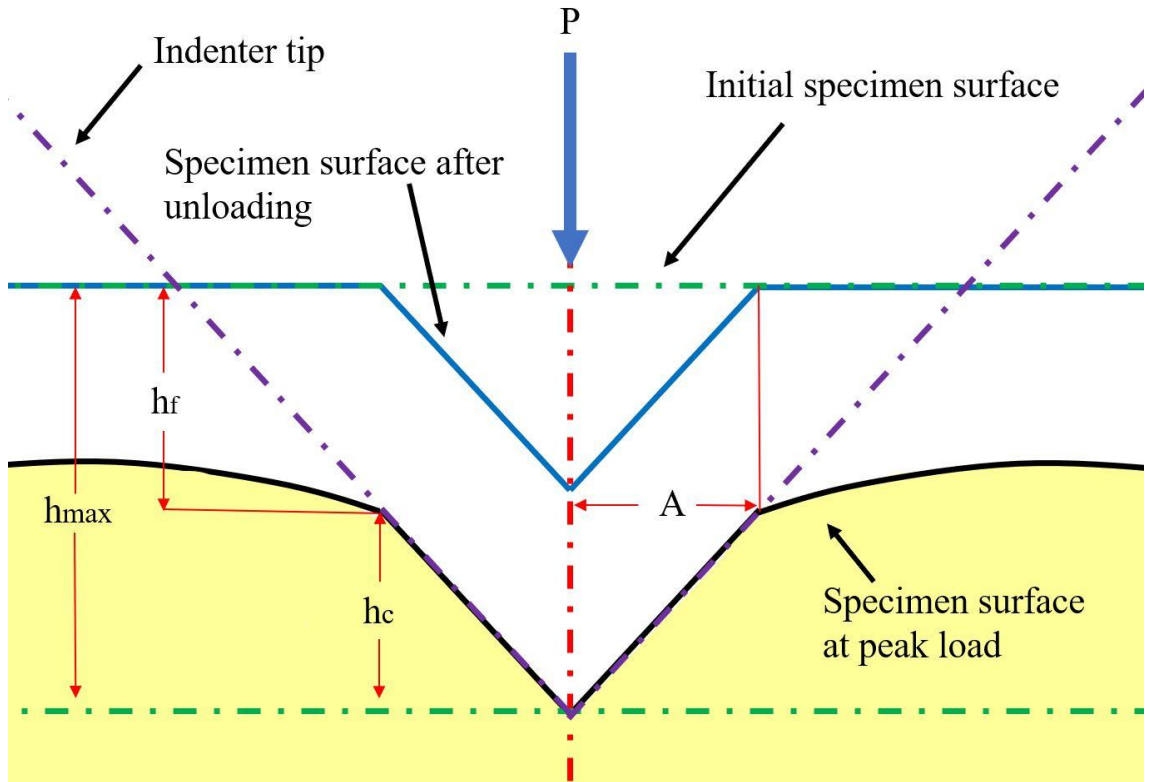


Figure 2.3: Specimen profile before, during, and after loading from the indenter tip. A depression from the indenter tip is typically left after the maximum load is applied.

The Oliver-Pharr method [26] relies on a power law function

$$P = \alpha(h - h_f)^m \quad (3)$$

for characterization of the unloading curve in which m and α are dimensionless constants.

The final indentation depth, h_f , is assumed to be zero only at elastic loads.

Depth-sensing techniques are necessary to calculate contact depth, h_c , from

$$h_c = h_{max} - \varepsilon \frac{P_{max}}{S} \quad (4)$$

where the geometric constant, ε , is unique to the indenter tip shape. The contact depth refers to the deformation that occurs on the specimen's surface during indentation (Fig 2.3). The indentation stiffness, S , is directly proportional to the material's reduced modulus, E_r , and its relationship is given by

$$E_r = \frac{S}{2\beta} \sqrt{\frac{\pi}{A(h_c)}} \quad (5)$$

This relationship was discovered from the extended Hertzian theory and nanoindentation elastic field analysis [28]. Beta factor, β , is distinct for each indenter tip geometry and is required to calculate the reduced modulus of the material. The contact area, $A(h_c)$, is evaluated at the specific contact depth for that individual indent. Furthermore, reduced modulus of the specimen is converted to the indentation modulus of the specimen, E_s , [29] from

$$\frac{1}{E_r} = \frac{1 - \nu_s^2}{E_s} + \frac{1 - \nu_i^2}{E_i} \quad (6)$$

The Poisson's ratios of the specimen, ν_s , and the indenter tip, ν_i , are necessary to convert between the reduced and indentation moduli. The Poisson's ratio for the Berkovich diamond indenter tip is 0.07 and its elastic modulus, E_i , is 1141 GPa [30].

2.2 – Indentation Theory for Polymers

Indentation tests on polymers yield slightly different results than on ceramics and metals. Primarily, the indentation tip shape and size drastically impact the indentation moduli and hardness values. The hardness is seen to decrease with an increase in maximum depth in most polymers [31]. As the maximum depth increases, the indentation size increases as well and results in a smaller hardness value. It is crucial to be cautious with indentation size because of accuracy limitations from indentation pile-up and sink-in (Fig. 2.4). These two phenomena can lead to inaccurate readings of hardness and indentation modulus [32, 33]. However, since polymers experience viscoelastic recovery during unloading, pile-up measured in this region was not significant enough to alter material property measurements [32].

To minimize pile-up and sink-in effects, the dwell time of at least 10 sec is recommended at the maximum load for viscoelasticity recovery in polymers to take place [32, 34]. Among soft materials, such as polymers, pile-in is more likely to occur than sink-in [35]. The initial yield stress to elastic modulus, Y/E , determines whether the residual indent will sink-in or pile-up and a low ratio corresponds to sink-in effects [36]. These effects can lead to inaccuracies of up to 60% in hardness and indentation modulus calculations [36, 37]. The indentation moduli were reduced when deformations were given time to equilibrate during the unloading curve [32]. The indentation size effect also causes critical concerns in area correction factors because the Berkovich indenter tip exhibits depth dependence in determining the hardness of the material [33, 38].

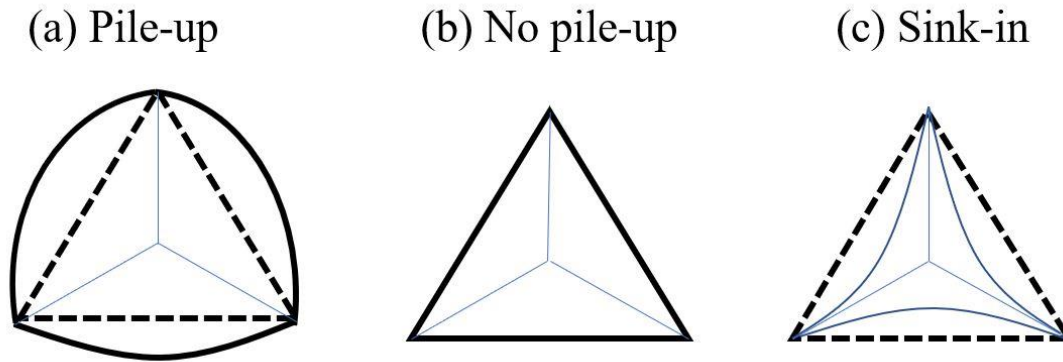


Figure 2.4: Schematic of indentation marks from Berkovich indenter with (a) pile-up, (b) no pile-up or sink-in, and (c) sink-in. The pile-up and sink-in effects can cause inaccuracies in mechanical property calculations.

Typically, the indentation modulus for most materials is acknowledged to be identical to the elastic modulus [39]. Elastic modulus and indentation modulus are comparable, but effects of pile-up and sink-in must be carefully examined when referring to the indentation modulus as the elastic modulus. It is preferred to consider differences in moduli based on testing methods that include globally and locally compressing the specimens. Compression and tensile testing globally test the specimen, whereas indentation tests locally compresses the specimen. Pile-up can cause an overestimation of indentation modulus but permitting for an adequate dwell time for a steady strain rate can mitigate the problem [32, 34, 39]. Specifically, the indentation modulus of polymers is a combination of the elastic and the viscous response of the material [40]. Even though time-dependent viscoelastic recoveries of the polymer are not isolated in nanoindentation, the indentation modulus unequivocally bestows practical information about the quasi static material behavior response.

Multiple cycle loading combines nanoindentation with cyclic loading to measure the changes in viscoelastic response found from depth vs. hysteresis tests (single cycle loading) [25, 30]. The frequency and number of cycles are varied throughout different tests to establish frequency-based behavior on the polymer. For example, a multiple cycle loading hysteresis graph consisting of five cycles is represented in Fig. 2.5. Each of the cycles occur at the same physical location on the specimen and the indenter tip remains on the specimen surface throughout the entire experiment. The period and frequency for each cycle is equivalent even though the displacements between cycles may differ. At higher cycles, multiple cycle loading can resemble a small-scale fatigue test localized at the indentation position on the specimen.

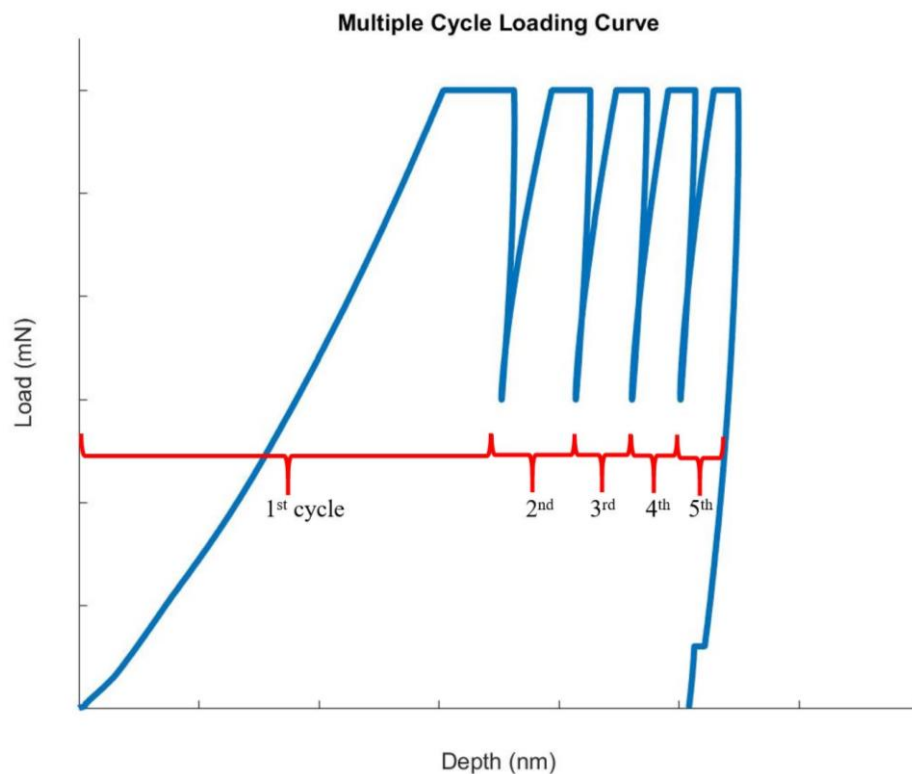


Figure 2.5: Multiple cycle loading hysteresis curve with five cycles. Each cycle has the same frequency although the displacements between the cycles may vary.

2.3 – Berkovich Tip

Berkovich and conical tips are few of the many geometries available for indenter tips. Typically, they consist of sharpened diamond for its hardness, granting it the ability to pierce almost any other material. Consequently, the diamond indenter tip is a feasible material for running thousands of indents because it has a high life expectancy. The Berkovich tip has a pyramidal geometry with a half angle of 65.3° [41] (Fig. 2.6). The geometric constant, Berkovich value, and beta factor are 0.72, 24.50, and 1.034, respectively [30].

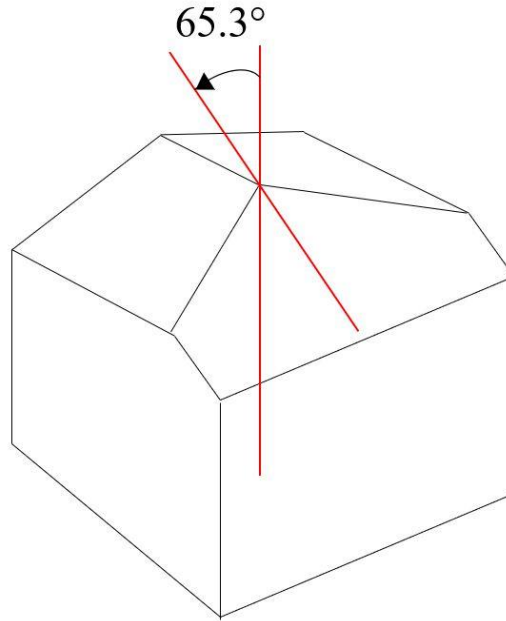


Figure 2.6: The Berkovich indenter tip with a face half angle of 65.3° . The indenter tip is made of diamond with a three-sided pyramidal geometry.

The theoretical diamond area function for the Berkovich indenter tip [41] given by

$$A(h_c) = 24.675h_c^2 + 0.562h_c + 0.003216 \quad (7)$$

is necessary for determining area contact between the specimen and tip. Commonly, the diamond area function is calibrated on quartz since Berkovich tips may vary in shapes after a plethora of indents.

The radius of the indenter tip is comparable to both the nanometer scale and Kevlar fiber diameter of micrometers [20, 39]. For comparison, a Berkovich indent on a SEM stub next to a single Kevlar K29 fiber is displayed in Fig. 2.7. The indent size is commensurable to the fiber diameter; therefore, indicating the importance of an area correction factor between the fiber's significant curvature and the indenter tip.

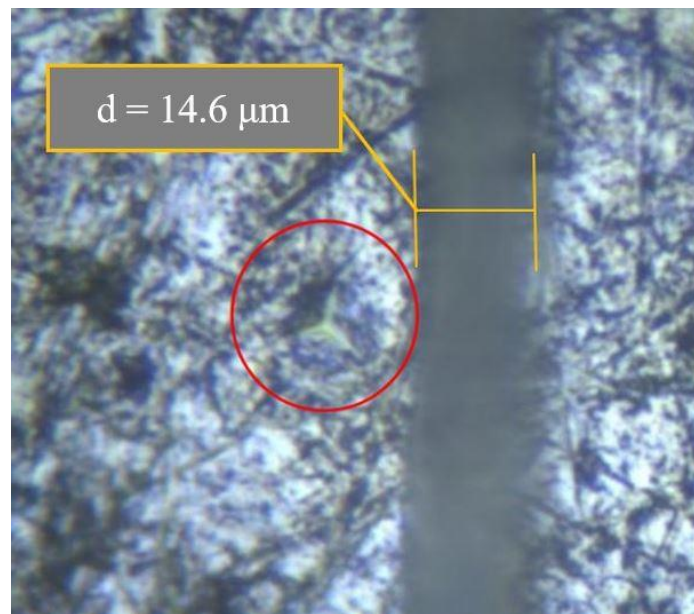


Figure 2.7: Circled in red is an indent made by the Berkovich indenter. Its size is in the same order of magnitude of the Kevlar fiber diameter; thus, incorporation of fiber curvature is paramount to the accuracy of measurements.

2.4 – Area functions

Accuracy in applying proper area functions is crucial to calculate the correct contact area and reduced modulus. The contact area depends on the contact depth,

constants relative to the geometry of the indenter tip, and the specimen surface roughness. Area correction is necessary for specimens, such as a single Kevlar fiber, with significant curvature and diameter comparable to the indent size (Fig. 2.7).

The standard Oliver-Pharr analysis considers the specimen to be a perfect semi-infinite plane and is applicable for planar specimens with small changes in surface roughness [26]. In cases where the specimen contains significant curvature, a modified user-defined area function must be determined to correctly calculate mechanical properties of the specimen.

The area function corresponding to the standard Oliver-Pharr method uses Eq. (7) and a fitted diamond area polynomial function (calibrated with quartz). The combined function is referred to as the flat area function (FAF) because it assumes that the surface geometry of the specimen is a semi-infinite plane. The order of the polynomial depends on the depth; if the maximum depth is less than 1,000nm, the order used is five, otherwise the order used is two. The FAF calculates the correct contact area for the SMP and PMDS (planar) specimens, but not the Kevlar samples due to significant curvature.

The modified user-defined function was developed with finite element analysis by considering the curvature of the fiber and Berkovich tip shape to establish the modified curved area function (mCAF) [13] as

$$A_{mCAF}(h_c) = [2.791 \ln(d) - 1.9447]h_c^2 + [1.547 \ln(d) + 1.9323]10^3 h_c \quad (8)$$

where the mCAF depends on the average diameter, d . Therefore, each type of Kevlar fiber tested will have its own unique mCAF coefficients. The indentation moduli, specifically for Kevlar fibers, found from both the mCAF and FAF are compared to literature to provide insight on the significance of modified contact area.

Chapter 3 – EXPERIMENTAL SETUP

3.1 - Specimen Preparation

Three different types of specimens were prepared: single Kevlar fibers (K29, KM2, and K119), polydimethylsiloxane (PDMS), and shape memory polymer (SMP). All single Kevlar fiber specimens were primed in the same methods, except Kevlar K29. Prior to mounting, the K29 fiber was pretreated in denatured alcohol for 12 hours to smoothen its uneven surface roughness. PDMS and SMP specimens were fabricated in the laboratory, while the Kevlar fibers were obtained directly from DuPont.

Preparing the Kevlar fiber specimens required the SEM stub to be prepped before the fibers were attached. A hand file was used to create two notches on the SEM stub which were located 180° apart from each other. The SEM stub was roughly sanded using a metallographic manual wheel polisher. After the SEM stub surface was leveled, the SEM stub was attached to a hand drill to be polished on 1000, 1500, 2000, and 2500 grit sandpaper. Sanding pads with higher grit of 3200, 3600, 4000, 6000, and 12000 were used for fine sanding. To provide a smooth surface for the fiber to lay, the SEM stub was finished with polishing compound and a Dremel.

Each type of Kevlar fiber yarn (K29, KM2, and K119) was cut to five inches in length and a single fiber was diligently extracted using tweezers. Each ends of the single fiber were adhered to two 1.1g steel washers with Loctite 495 Super Bond Instant Adhesive glue. Approximately after 24 hours, the fiber was placed between the notches on the SEM stub with the two washers suspended off each side. The same adhesive was used to glue the fiber to the SEM stub near the notches (Fig. 3.1). The washers were

clipped off when the adhesive dried in 24 hours. This method was adopted from the nanoindentation Kevlar studies by Turla, Raju, and Pelegri [13, 42].

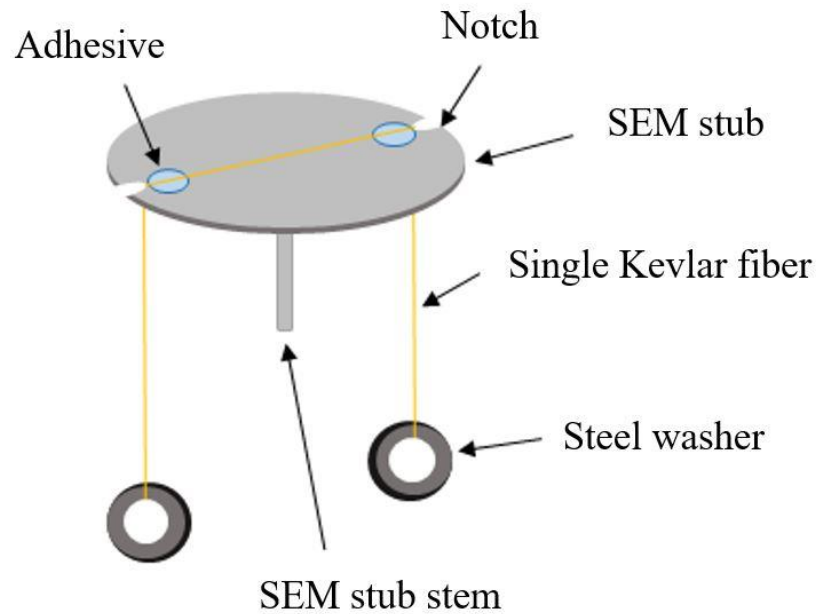


Figure 3.1: The single Kevlar fiber was carefully hung between two notches where the adhesive was applied. In order for the steel washers to hang freely, pliers were utilized to suspend the SEM puck stem on the edge of a table.

The polydimethylsiloxane (PDMS, $(C_2H_6OSi)_n$) specimen was cured with a Sylgard 184 silicone elastomer base and silicone elastomer crosslinker (10:1 weight ratio) [43]. The mixed polymer was degassed for 30 minutes to remove air bubbles trapped during mixing. Then the mixture was injected between two glass microscope slides separated by 1mm spacers and was heated at 70°C for 5 hours. The cured elastomer was carefully extracted from the glass slides using a razor blade and cut into a square with a length of 1cm. It was mounted on a polished SEM stub with Loctite 495 Super Bond Instant Adhesive glue and left to dry for 12 hours.

The shape memory polymer (SMP) was prepared with a 4:1 (weight ratio) mixture of Benzyl-methacrylate (BMA, $C_{11}H_{12}O_2$) and Bisphenol A ethoxylate dimethacrylate (BPA, $[H_2C=C(CH_3)CO_2(CH_2CH_2O)_n C_6H_4-4-]_2C(CH_3)_2$). The SMP precursor resin was injected between two glass slides separated by 1mm spacers. The solution was set to cure in 365 nm UV oven for 20 minutes, similarly done by Safranski and Gall [44]. The glass slides were removed using a razor blade and cut to an identical size as the PDMS specimens to be mounted on a SEM stub with the same adhesive.

3.2 – Single and Multiple Cycle Loading Experimental Setup

The Micro Materials NanoTest Vantage was operated to investigate the mechanical properties of the polymer specimens via nanoindentation. The Vantage contains three main components: a microscope (with lenses of 5x, 10x, 20x, and 40x magnification), sample stage, and low load head (contains the pendulum and indenter tip). A depth-sensing capacitor near the indenter tip measures the indentation depth and the load is applied using an electromagnetic force from the magnet and coils (Fig. 3.2). The load limits for the Vantage range from 0.5mN to 500mN and the maximum available depth is around 20,000nm.

The environmental testing chamber was held at a constant temperature of 28°C with 20% humidity and the Berkovich diamond indenter tip was fitted in the indenter shaft for all indentation tests. The focal plane and cross hair calibrations were performed for nanoindentation accuracy. Before each experiment, a pendulum balance test was conducted to ensure the pendulum had a full-range of motion. Before data collection, the specimen on the SEM stub was mounted to the Vantage's sample stage. The specimen

was focused on the microscope with the 40x magnification and the location of the indents were precisely chosen to avoid any indentations on surface imperfections.

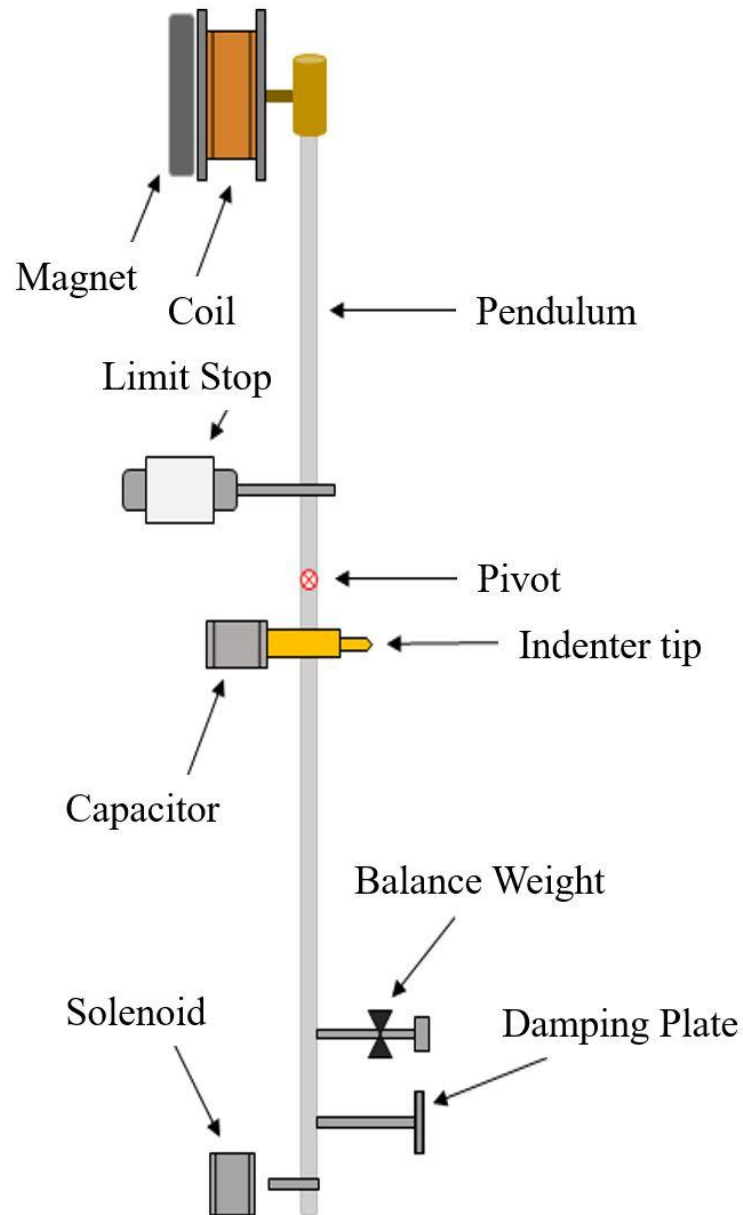


Figure 3.2: The pendulum components from the low load head in the Vantage. The depth-sensing capacitor and electromagnetic coils provide precise control of the load and depth. The balance weight is used for load calibration, which needs to be done whenever the pendulum is removed from the low load head.

To setup the single cycle indentations, the depth vs. load hysteresis experiment type was chosen. The single cycle indentations were performed on all the specimens (Kevlar, PDMS, and SMP). The multiple cycle loading indentations were exclusively performed on the PDMS and SMP specimens to study viscoelastic response. A picture of the SMP specimen in front of the Berkovich indenter is shown in Fig. 3.3. The thermal drift correction was chosen to collect post-indentation data and the number of indents for each test varied from 5 to 20, depending on the repeatability of the tests. Each of the indents were separated by a distance greater than $15\mu\text{m}$, to ensure that there was no stress field overlap between each indent (higher loads had a larger separation distance).

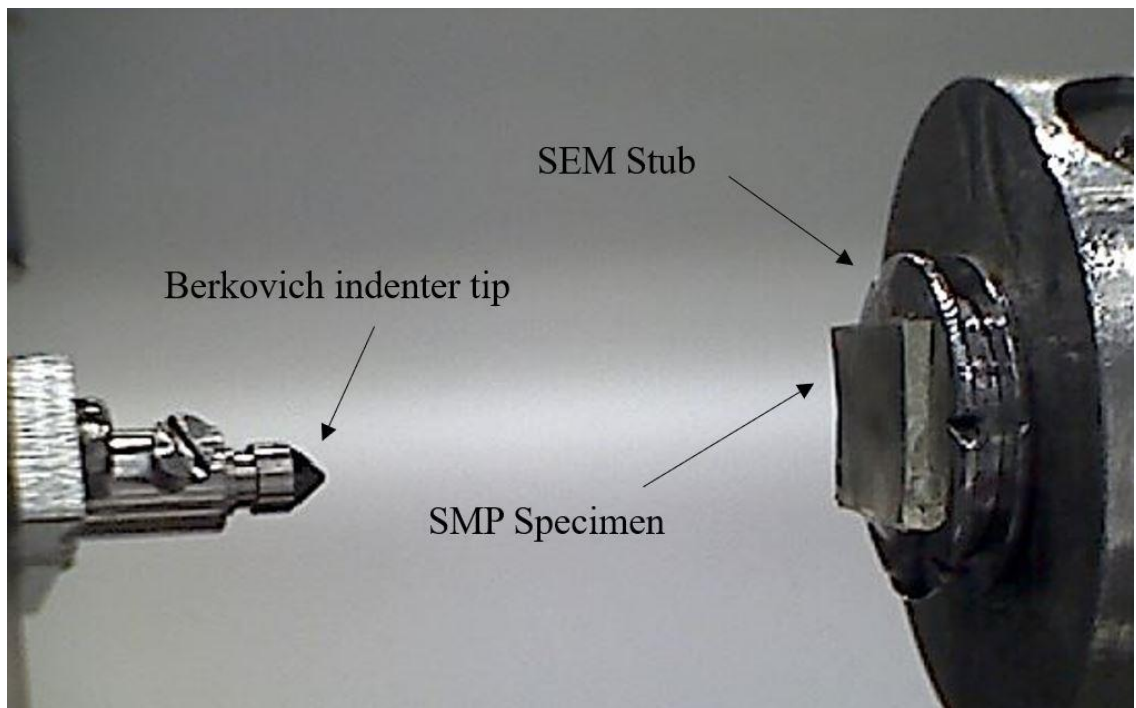


Figure 3.3: SMP mounted on Vantage in front of the Berkovich indenter.

3.3 – Table of Experiments

Single cycle loading was the only method tested on the Kevlar fibers to study the variation of indentation modulus along the fiber diameter (Table 3.1). The parameters used for each single cycle loading test included loading and unloading periods of 50 sec. The extended loading and unloading times encouraged adjustments within fiber dislocations to prevent slipping. The dwell time at maximum load and thermal drift correction were 10 sec and 30 sec, respectively for all fibers. Kevlar K29 fibers were tested at the following loads: 1 mN through 3mN (increments of 1 mN) and 5mN through 40mN (increments of 5mN). The KM2 fiber was tested at the same loads at the K29 fiber excluding any loads greater than 25mN. Finally, loads ranging from 3mN through 40mN were tested on the K119 fibers. Caution was taken with loads exceeding 50mN to prevent breaking the fiber. The reduced modulus was calculated with the mCAF for cylindrical area correction.

Table 3.1: Experiments on specimens of significant curvature (Kevlar fibers).

Specimens	K29	KM2	K119
Diameter (μm)	14.6	12	15.33
Physical form	Single fiber extracted from yarn and treated in denatured alcohol	Single fiber extracted from yarn	
Experimental Methods	Single cycle indentation		
Parameters for single cycle indentation	Load time (sec): 50 Dwell period (sec): 10 Unload time (sec): 50 Loads (mN): 1, 2, 3, 5, 10, 15, 20, 25, 30, 35, 40	Load time (sec): 50 Dwell period (sec): 10 Unload time (sec): 50 Loads (mN): 1, 2, 3, 5, 10, 15, 20, 25	Load time (sec): 50 Dwell period (sec): 10 Unload time (sec): 50 Loads (mN): 3, 5, 10, 20, 25, 30, 35, 40
Caution	Loads exceeding over 50mN may cause the fiber to break Area correction is needed for all fibers in analysis		

The experimental methods employed on specimens of planar surface geometry were single and multiple cycle loading to study the significance of frequency dependence (Table 3.2). The loading, unloading, and dwell times during the single cycle loading tests were 10 sec to prevent ‘nosing’ in the hysteresis graphs [34]. These parameters resulted in smoother unloading curves because the viscoelastic effects developed within that time interval. Lower loads from 1 to 4mN were tested on the PDMS because it was very soft. Contrarily, the SMP specimens were tested at a larger range of loads from 2mN through 300mN because it was able to maintain its form at higher loads.

Multiple cycle loading on the planar specimens were necessary to determine the changes in viscoelastic response found in the hardness and indentation modulus values [25]. During the multiple cycle indentation tests, the frequency ranges were varied at 1, 0.5, and 0.033Hz to examine the influence of frequency on the polymer specimens. During 0.5Hz tests, the loading and unloading portions ran for 2 sec each with no hold time at maximum load. Similarly, the 1 Hz tests consisted of a loading and unloading time of 0.5 sec each and no dwell period. Finally, the 0.033Hz tests carried out loading, unloading, and hold time for 10 sec each. The comparison between frequencies for ease are provided in Table 3.3, where the frequencies in column A are compared to those from row B (A:B ratio). The cycles tested were 5, 50, and 100 for both specimens to study cyclic dependency on polymers. The loads tested on PDMS with multiple cycle loading were 1, 2, and 3mN, while SMP specimens were tested with 3, 10, and 50mN loads.

Table 3.2: Experiments on polymer specimens of planar surface area and minimal surface roughness.

Specimens	PDMS	SMP
Thickness (mm)	1	1
Physical form	Fully cured in room temperature air	Fully cured in room temperature air
Experimental Methods	Single cycle indentation Multiple cycle indentation	
Parameters for single cycle indentation	<i>Load time (sec): 10</i> <i>Dwell time (sec): 10</i> <i>Unload time (sec): 10</i> <i>Loads (mN): 1, 2, 3, 4</i>	<i>Load time (sec): 10</i> <i>Dwell time (sec): 10</i> <i>Unload time (sec): 10</i> <i>Loads (mN): 2, 3, 4, 5, 10, 20, 30, 50, 100, 200, 250, 300</i>
Parameters for multiple cycle indentation	<i>5 cycles: 1mN, 2mN, 3mN for 0.5Hz, 1Hz, 0.033Hz</i> <i>50 cycles: 1mN, 2mN, 3mN for 0.5Hz, 1Hz, 0.033Hz</i> <i>100 cycles: 1mN, 2mN, 3mN for 0.5Hz, 1Hz, 0.033Hz</i> Frequency breakdowns: 0.5Hz: <i>Load time (sec): 1</i> <i>Dwell time (sec): 0</i> <i>Unload time (sec): 1</i> 1Hz: <i>Load time (sec): 0.5</i> <i>Dwell time (sec): 0</i> <i>Unload time (sec): 0.5</i> 0.033Hz: <i>Load time (sec): 10</i> <i>Dwell time (sec): 10</i> <i>Unload time (sec): 10</i>	<i>5 cycles: 3mN, 10mN, 50mN for 0.5Hz, 1Hz, 0.033Hz</i> <i>50 cycles: 3mN, 10mN, 50mN for 0.5Hz, 1Hz, 0.033Hz</i> <i>100 cycles: 3mN, 10mN, 50mN for 0.5Hz, 1Hz, 0.033Hz</i> Frequency breakdowns: 0.5Hz: <i>Load time (sec): 1</i> <i>Dwell time (sec): 0</i> <i>Unload time (sec): 1</i> 1Hz: <i>Load time (sec): 0.5</i> <i>Dwell time (sec): 0</i> <i>Unload time (sec): 0.5</i> 0.033Hz: <i>Load time (sec): 10</i> <i>Dwell time (sec): 10</i> <i>Unload time (sec): 10</i>

Table 3.3: Frequencies tested and their respective relationships to each other, listed as A:B ratio.

		B		
		1 Hz	0.5 Hz	0.033 Hz
A	1 Hz	1	2	30.3
	0.5 Hz	0.5	1	15.15
	0.033 Hz	0.033	0.066	1

Chapter 4 – RESULTS AND DISCUSSION

For completeness of fiber characterization, the Kevlar single fibers are reported at 10% and up to 40% of the single fiber diameter in the present study. The fiber is treated as a thin film because surface roughness is not comparable to the magnitude of its diameter [15, 45, 46] and 0.1 ratio (depth to fiber diameter) rule was the basis for assessing indentation moduli, originating from the substrate effect [45, 46]. Indentation moduli corresponding to depths greater than 10% of fiber diameter were included in the analysis, but the reliability of these results were taken with caution.

Two different area functions defined for fiber characterization, flat area function (FAF) and modified curved area function (mCAF), were applied to compute the Kevlar fiber indentation moduli. Error comparison was the sole purpose of tabulating the fiber moduli yielded from the FAF. The polydimethylsiloxane (PDMS) and shape memory polymer (SMP) planar specimens solely required the FAF for calculating indentation moduli because they were relatively flat specimens with miniscule changes in surface roughness.

Literature results from compression tests were compared to those of indentation tests in the present study, but data was loosely considered because of differences in methodology [20, 39, 47]. Studies indicating moduli results from indentation were also examined for differences in material type, specimen preparation, and analysis. For instance, some literature reports did not include area correction factors for their indentation analysis of fibers [15]. Small discrepancies may arise between data with variations in testing methods and analysis, hence they must be acknowledged as approximations.

The transverse Poisson's ratio for Kevlar fibers that did not have reported values in literature were closely assessed based on bond composition. The estimation of this ratio in anisotropic fibers is derived from the transverse angles formed between bonds and crystalline geometry. Cheng, Chen, Weerasooriya, Muhammed, and Ismaeel reported the transverse Poisson's ratio of 0.35 for Kevlar KM2 [48] and K29 [49]. In respect to their crystalline geometry, it is commonly estimated that both KM2 and K29 have a Poisson's ratio of 0.30 and K119 embodies a lower ratio of 0.27 [50]. Both ratios for KM2 and K29 fibers are included for analysis to determine the importance of accuracy in Poisson's ratio. Conceptually, the requirement of exact Poisson's ratios for Eq. (6) proved to be insignificant in FEM analysis [13]. Similar trends with Poisson's ratio insignificance were observed in compression tests on single monofilament fibers [51, 52].

4.1 – Indentation Moduli at 10% Kevlar Fiber Diameter

Single cycle loading indentation method was performed on Kevlar fibers at varying loads (Table 4.1). The asterisk (*) in Table 4.1 indicates that the corresponding load-controlled test achieved a maximum depth neighboring 10% of fiber diameter. The indentation tests designated with asterisks in Table 4.1 are separately examined for each fiber at 10% diameter, while the rest of the loads are discussed from skin depth to 40% of fiber diameter.

Table 4.1: The loads tested on three different types of fibers. The symbol (*) denotes the load tested which reached 10% of fiber diameter.

Loads (mN)	K29	KM2	K119
1	X	X	
2	X	X	
3	X*	X	X
5	X*	X*	X*
10	X	X	X
15	X	X	
20	X	X	X
25	X	X	X
30	X		X
35	X		X
40	X		X

The two Poisson's ratios of 0.30 and 0.35 (for KM2 and K29) are tabulated with their corresponding indentation moduli computed from the mCAF and FAF in Table 4.2. It was a common trend of 5mN load reaching a depth around 10% of fiber diameter across all types of Kevlar tested, except 3mN was an additional load for K29. The indentation moduli values analyzed from the FAF strayed further away from literature values presented in Table 4.2. Rather, moduli computed with the mCAF were closer in respect to reported literature and also larger in value than the ones calculated with the FAF.

Table 4.2: Average indentation moduli computed from both mCAF and FAF at 10% of Kevlar fiber diameter.

Fiber	Fiber Diameter (μm)	Poisson's Ratio, ν	E_s from mCAF (GPa)	E_s from FAF (GPa)	Literature Modulus (GPa)
KM2	12	0.30 [50]	5.10 ± 0.4	3.34 ± 0.3	6.2 ± 1.0 [15]
		0.35 [48,49]	4.91 ± 0.4	3.22 ± 0.3	
K29	14.6	0.30 [50]	2.95 ± 0.3	1.82 ± 0.3	2.59 [18]
		0.35 [48,49]	2.84 ± 0.3	1.76 ± 0.3	
K119	15.33	0.27 [50]	2.43 ± 0.4	1.61 ± 0.4	2.31 [18]

The indentation moduli determined from the mCAF in Table 4.2 is illustrated in Fig. 4.1 as bar graphs. The KM2 fibers exhibited the highest indentation moduli when compared to the other two fibers. Conversely, the K119 fibers had the lowest indentation modulus of 2.43 ± 0.4 GPa, confirming it is highly flexible and softer than the other fibers. The indentation moduli determined from $\nu=0.30$ were slightly higher for both KM2 and K29 fibers in relation to their respective values for $\nu=0.35$.

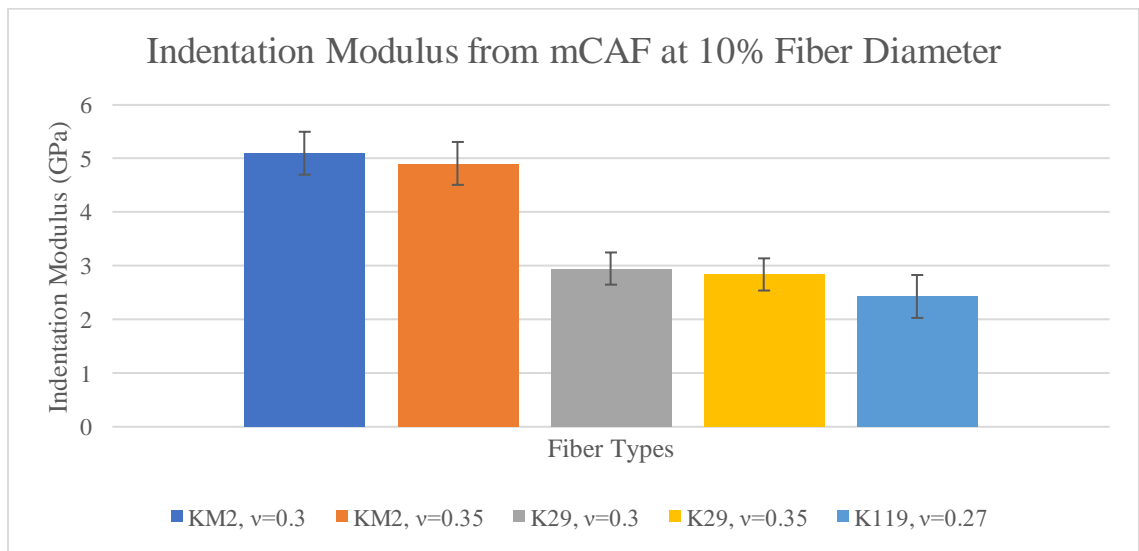


Figure 4.1: Indentation moduli from the mCAF measured at indentation depth equal to 10% of the fiber diameter.

4.1.1 Kevlar K29 Fiber

The average measured Kevlar K29 diameter across five samples was $14.6\mu\text{m}$ and is close to the proposed $15\mu\text{m}$ with $1\mu\text{m}$ skin [19] (Fig. 4.2). The Kevlar K29 was treated in denatured alcohol for obtaining consistent nanoindentation graphs. Its natural surface roughness is visible in Fig. 4.2 before treatment. Smaller ridges and bumps on the surface of the fiber from treatment allowed for more repeatable tests.

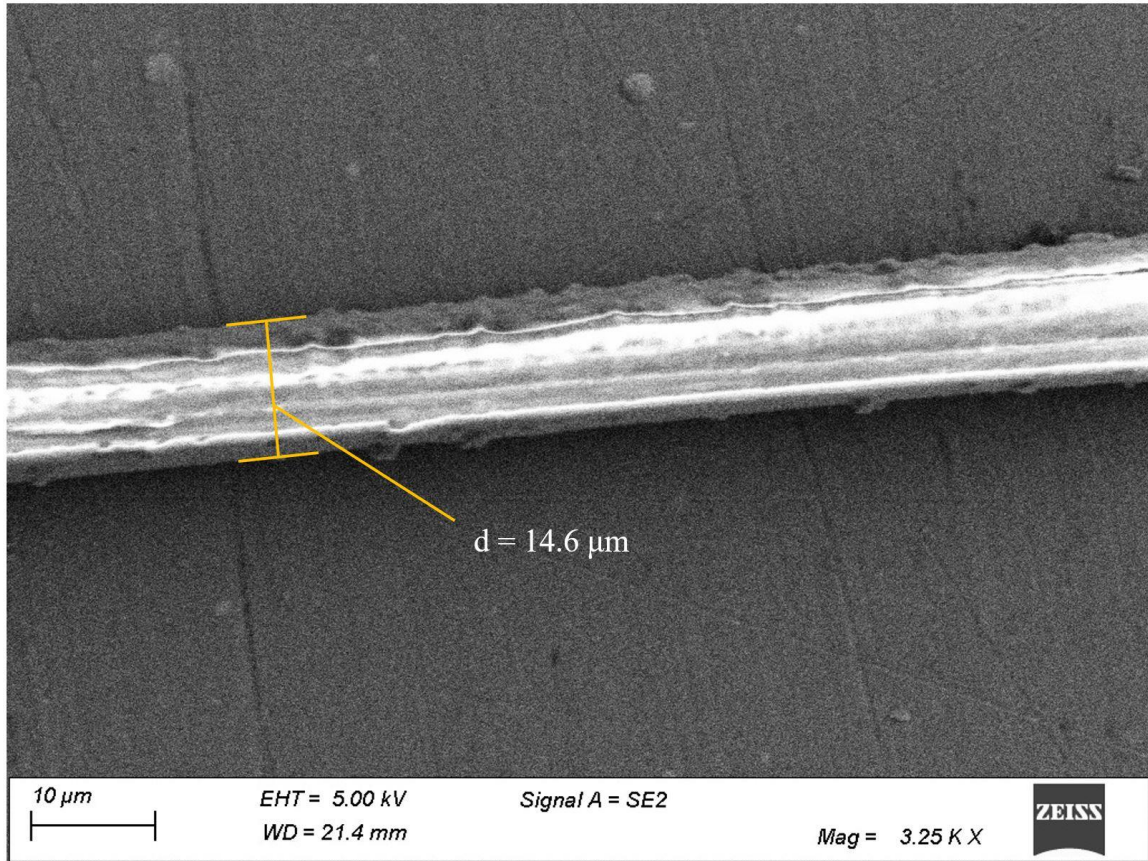


Figure 4.2: SEM picture of K29 fiber before treatment in denatured alcohol. The fiber has a rough surface, which is clearly visible.

At 3 and 5mN loads, 20 indents were performed under load-controlled conditions on single K29 fibers, out of which, the six most representative are presented in Fig. 4.3. The indentation depth for 3mN was slightly below 10% fiber diameter, while the depth at 5mN was just above 10% fiber diameter. Evidently, both sets of data are incorporated in the indentation modulus of K29 at 10% of the fiber diameter in Table 4.2.

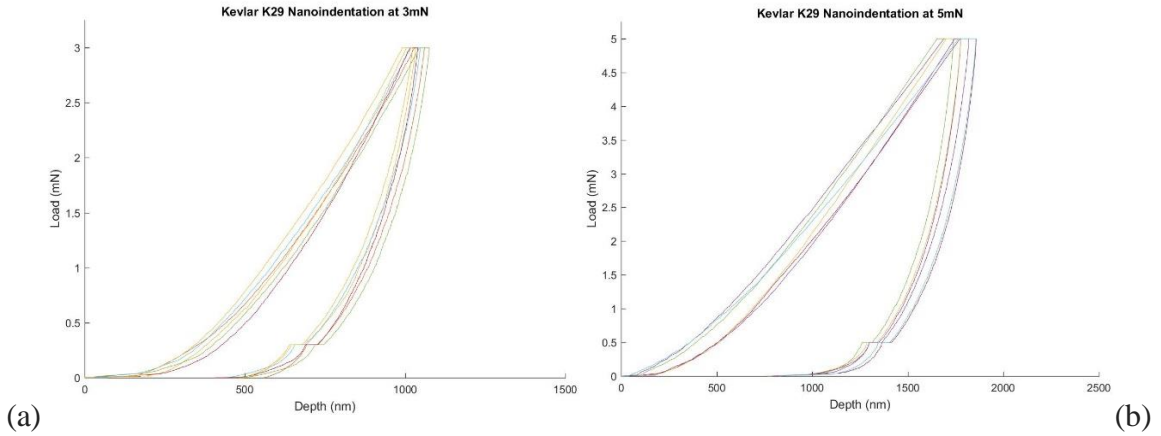


Figure 4.3: Kevlar K29 single cycle nanoindentation at (a) 3mN (6 curves) and (b) 5mN (6 curves) with respect to a depth of 10% fiber diameter.

The indentation moduli calculated using the mCAF for Poisson's ratios of 0.30 and 0.35 are, 2.95 ± 0.3 GPa and 2.84 ± 0.3 GPa, respectively. From compression tests, Kawabata, Singletary, Davis, and Song recorded elastic moduli values 2.59 GPa [18] and 2.45 ± 0.40 GPa [53], respectively. Their reported values match that of the data from the mCAF within 20% difference. Obvious differences in mechanical properties originate from distinct testing methods and specimen preparation. For example, Singletary's research group tested K29 fibers with a different diameter and a higher transverse Poisson's ratio of 0.43 [54]. When compared to Kawabata's computed elastic modulus, the indentation moduli calculated from the mCAF for Poisson's ratios of 0.3 and 0.35 result in a difference of 13.9% and 9.7%, respectively. In contrast, the difference between Kawabata's value and indentation moduli from the FAF for Poisson's ratios of 0.3 and 0.35 were 29.7% and 32%, respectively. Therefore, the disparity between reported (from compression testing) and computed values (from nanoindentation) was diminished when indentation moduli was calculated with area correction factors.

4.1.2 Kevlar KM2 Fiber

The measured average diameter of KM2 fibers across four samples was $12\mu\text{m}$ with a skin thickness of 200 nm [14, 42]. The KM2 fiber, shown in Fig. 4.4, was generally smoother than the K29 fiber. McAllister's research group concluded KM2's indentation modulus was $6.2 \pm 1.0\text{ GPa}$ using a Berkovich tip without any area correction factors [15]. Although their values largely diverged from FAF values reported in Table 4.2, the mCAF results displayed substantial compliance with their findings. The calculated indentation modulus of KM2 Plus from Cole's research group was $7.74 \pm 0.96\text{ GPa}$ [16]. Although KM2 Plus was not a specimen examined in the present study, it was clearly stiffer than the original KM2. Cole's study additionally implemented a Berkovich indenter, but their area correction analysis assumed the indenter to have a spheroconical geometry [16]. The differences between the contact area of spheroconical and Berkovich geometry are noticeably different arising from their distinct area functions [41]. Hence, the mCAF accurately incorporates the Berkovich indenter's pyramidal geometry for modulus calculation.

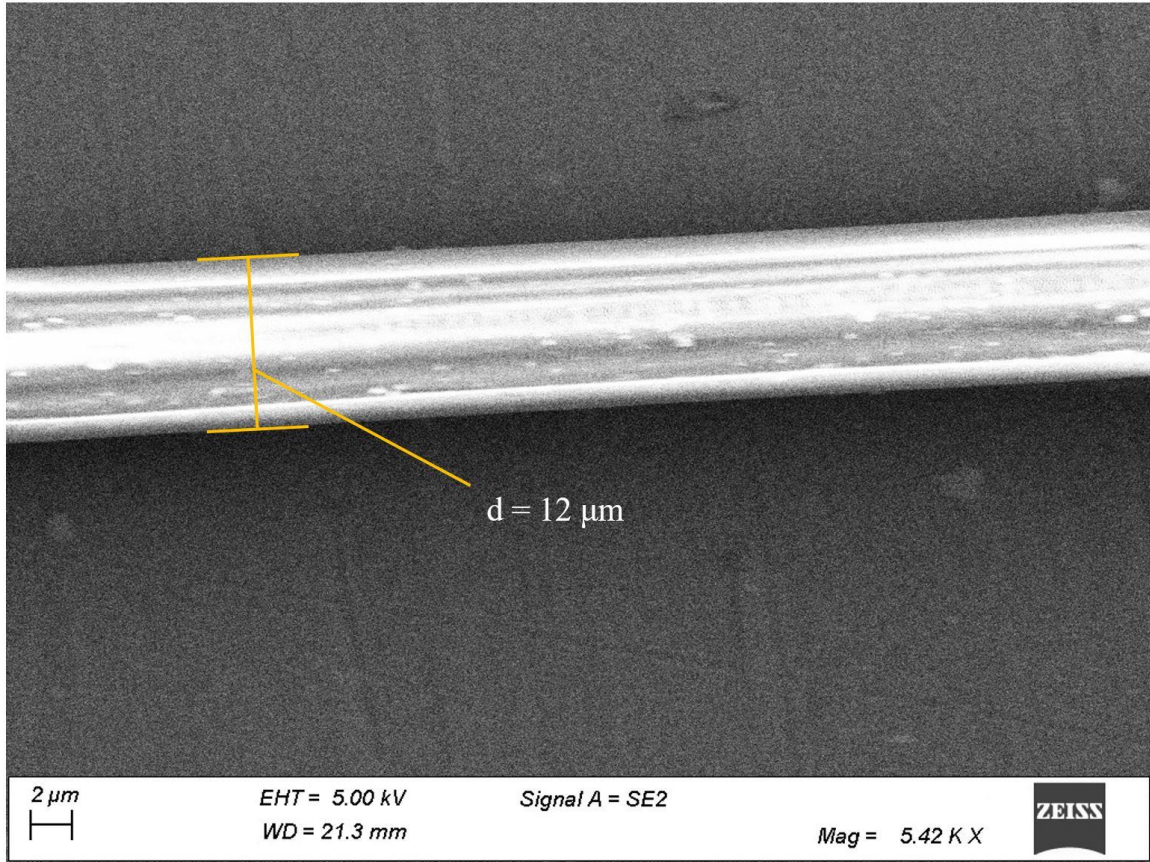


Figure 4.4: SEM picture of KM2 fiber with clear distinction of a smoother surface than the K29 fiber.

The indentation moduli for 10% KM2 fiber diameter in Table 4.2 originate from the 5mN hysteresis curves (Fig 4.5). The indentation moduli computed from the mCAF for Poisson's ratios of 0.3 and 0.35 are 5.10 ± 0.4 GPa and 4.91 ± 0.4 GPa, respectively. Comparing these values to 6.2 ± 1.0 GPa [15], the percent differences for the moduli with Poisson's ratios of 0.30 and 0.35 are 17.74% and 20.8%, respectively. Greater differences in reported and computed values emerge from an absence of area correction factors in McAllister's study [15].

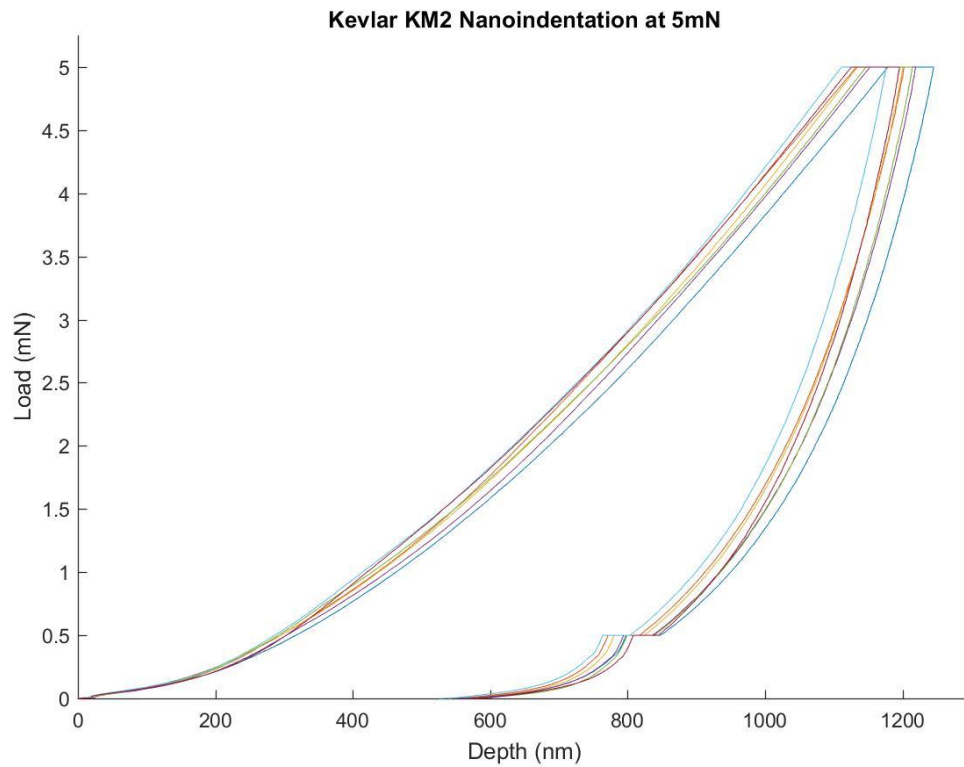


Figure 4.5: Kevlar KM2 single cycle nanoindentation at 5mN (7 curves) with respect to a depth of 10% fiber diameter.

4.1.3 Kevlar K119 Fiber

Across five specimens, the average measured diameter for K119 was $15.33\mu\text{m}$ with a skin of $3.5\mu\text{m}$ [55]. The surface for K119 (Fig. 4.6) was much smoother than K29's surface and further comparable to KM2's surface roughness. Kawabata's compression test study reported that K119 has an elastic modulus of 2.31 GPa [18]. Table 4.2 depicts that the corrected indentation modulus at 10% of K119 fiber diameter was 2.43 ± 0.4 GPa. Load-controlled hysteresis graphs for single cycle indents at 10% of K119 fiber diameter consisted of four representative load curves (Fig 4.7). Kawabata's compression tests differ from indentation experiments, resulting in minimal differences from different testing methods. The percent difference for indentation modulus

determined from the mCAF was 5.19% when compared to 2.31 GPa [18]. The modulus computed from the FAF, 1.61 ± 0.4 GPa, was very low compared to reported literature. Ultimately, error decreased drastically when considering the mCAF rather than FAF.

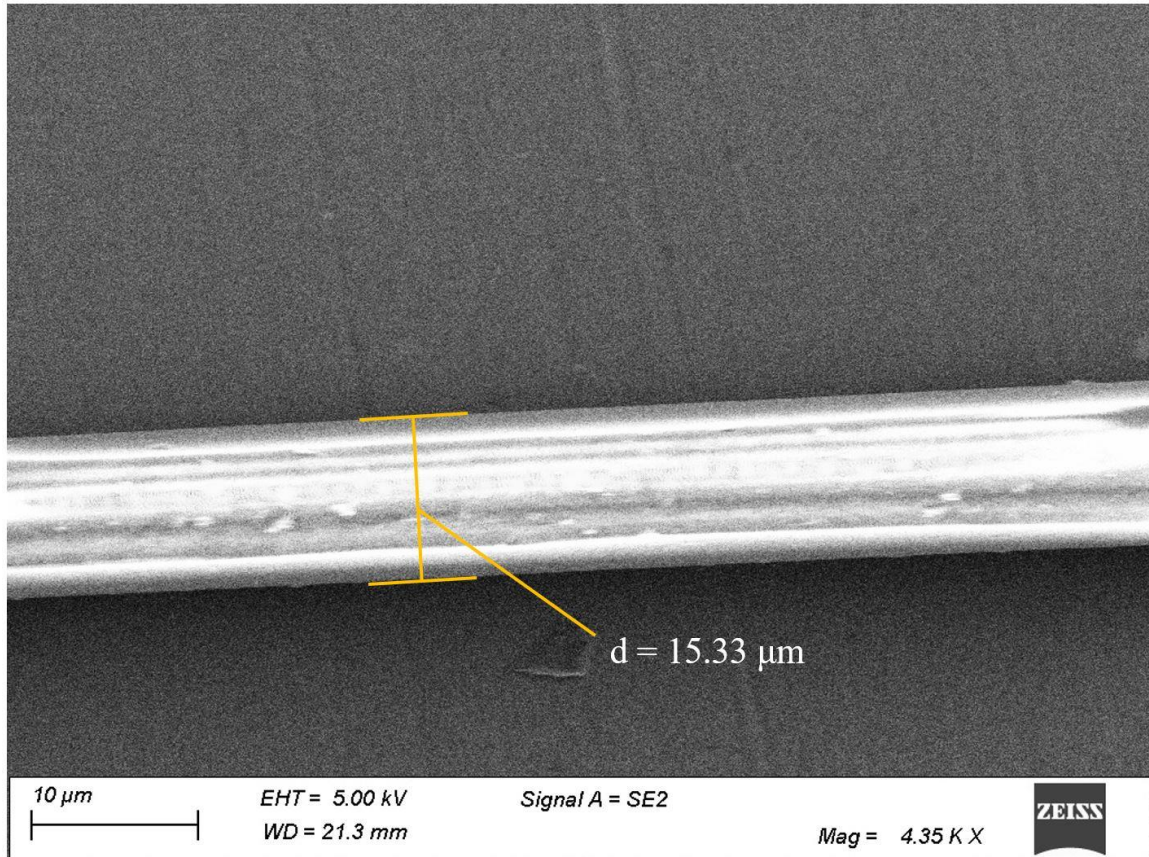


Figure 4.6: SEM picture of KM2 fiber with clear distinction of a smoother surface than the K29 fiber.

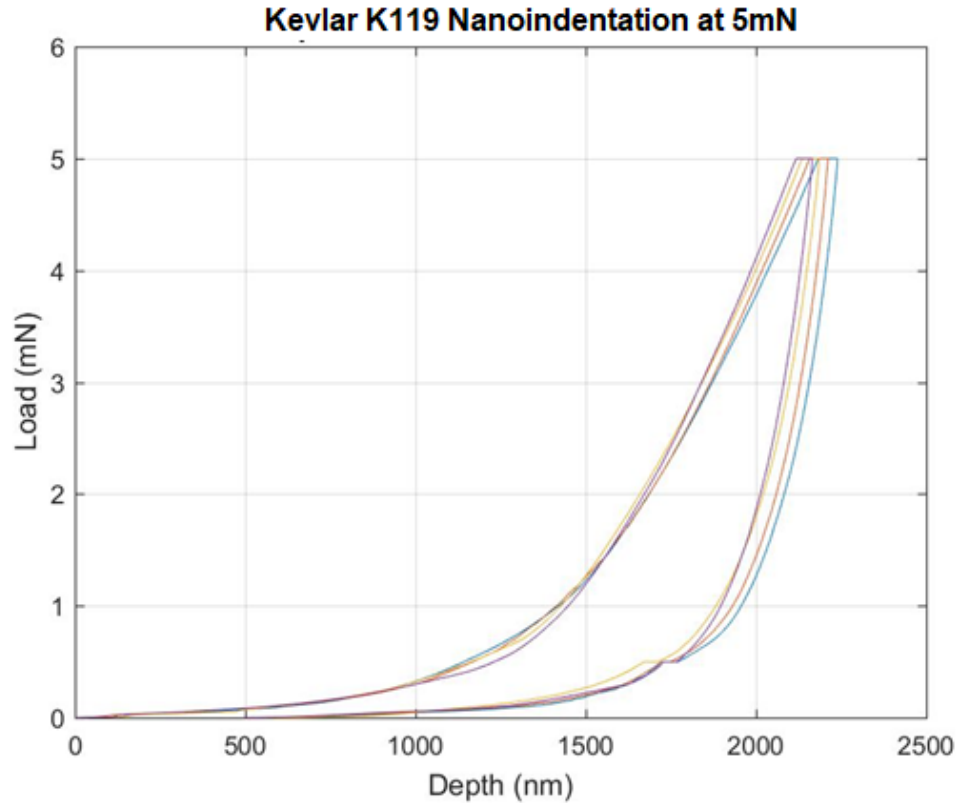


Figure 4.7: Kevlar K119 single cycle nanoindentation at 5mN (4 curves) with respect to a depth of 10% fiber diameter.

4.2 – Indentation Moduli at Various Percentages of Fiber Diameter

All load-controlled tests marked in Table 4.1 characterize the indentation moduli at various depths across fiber diameter. The hysteresis curves corresponding to the loads not marked with asterisks are plotted in Appendices A (K29), B (KM2), and C (K119). The maximum indentation depths corresponding to each load are split up in relation to the fiber diameter ranging from the skin, 2-13%, 7-13%, and 25-40%. The indentation moduli calculated from the mCAF and FAF are tabulated in Tables 4.3 and 4.4, respectively, illustrating the drastic effect area correction functions have. Evidently, the K29 and K119 skin was stiffer and less elastic than the fibers' core. The lowest load of 1mN completely pierced the KM2 fiber's skin, but the trends between skin and core were

assumed to be the same. K119 fibers exhibited the most elasticity, while KM2 fibers possessed stiffer bonds. Remarkably, the K29 fiber's skin was slightly stiffer than the core of the KM2 fiber, but KM2's core was stiffer than K29's core. The indentation moduli for all fibers complied within a reasonable range of reported literature. The Poisson's ratio difference between 0.30 and 0.35 did not provide a significant contribution to the indentation moduli; rather, the effect of the contact area geometry between the mCAF and FAF was more prominent. Hence, it is imperative that the contact area between the indenter tip and fiber be accurately calculated.

Table 4.3: Indentation modulus computed with mCAF at skin, 2-13%, 7-13%, and 25-40% of fiber diameter for Kevlar fibers.

Fiber	d (μm)	Skin Thickness (μm)	Skin/ Fiber (%)	ν	Indentation Modulus (GPa)				Literature Modulus (GPa)
					Skin	2- 13%	7- 13%	25- 40%	
KM2	12	~0.2 [14]	1.67	0.30 [50]	--	5.28	--	5.28	6.2 ± 1.0 [15]
				0.35 [48,49]	--	5.09	--	5.10	
K29	14.6	~1 [19]	6.85	0.30 [50]	6.89	--	2.95	2.98	2.59 [18]
				0.35 [48,49]	6.65	--	2.84	2.88	2.45 ± 0.4 [53]
K119	15.33	~3.5 [55]	22.83	0.27 [50]	2.43	--	--	2.21	2.31 [18]

Table 4.4: Indentation modulus computed with FAF at skin, 2-13%, 7-13%, and 25-40% of fiber diameter for Kevlar fibers.

Fiber	d (μm)	Skin Thickness (μm)	Skin/ Fiber (%)	ν	Indentation Modulus (GPa)				Literature Modulus (GPa)
					Skin	2- 13%	7- 13%	25- 40%	
KM2	12	~0.2 [14]	1.67	0.30 [50]	--	3.77	--	3.77	6.2 ± 1.0 [15]
				0.35 [48,49]	--	3.64	--	3.64	
K29	14.6	~1 [19]	6.85	0.30 [50]	7.11	--	1.82	1.59	2.59 [18]
				0.35 [48,49]	6.86	--	1.76	1.53	2.45 ± 0.4 [53]
K119	15.33	~3.5 [55]	22.83	0.27 [50]	1.61	--	--	1.22	2.31 [18]

4.2.1 Kevlar K29 Fiber

Using nanoindentation, Bencomo-Cisneros and their research group reported the average hardness for K29 as 1.3 ± 0.7 GPa at a maximum depth of 100 nm [17]. This value was suspected to be the hardness of the skin because the maximum depth of 100nm does not exceed the 1 μ m thick skin [19]. Therefore, their research study concluded no differences between the skin and core of the fiber [17]. According to Wollbrett-Blitz's research group, there was a clear difference in mechanical properties between the skin and core of the K29 fiber [19]. The data, in Tables 4.3 and 4.4, supported Wollbrett-Blitz's conclusion of moduli differences between the skin and core of the K29 fiber. From measurement results, the hardness of K29 skin was 0.68 GPa, which fell within the range reported by Bencomo-Cisneros and their research group [17].

The FAF data for the K29 fiber yielded a slightly higher skin modulus than the mCAF. Contrarily, the mCAF yielded a higher indentation modulus for the fiber core in comparison to the FAF. The moduli for K29 in Tables 4.3 and 4.4 are illustrated in Fig. 4.8 for visual comparison at different percentages along the fiber diameter. The corresponding load-controlled hysteresis curves are in Appendix A for reference. The skin indentation modulus was roughly more than twice its core modulus. Kawabata's results clearly aligned with the moduli at 7-13% and 25-40% of fiber diameter.

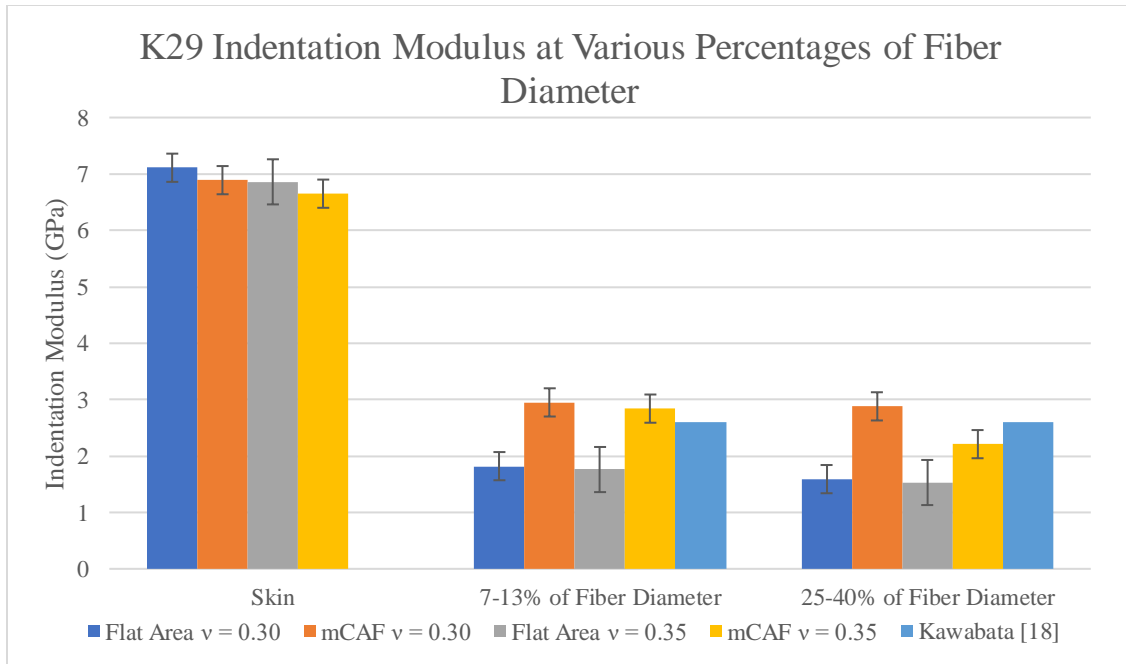


Figure 4.8: K29 indentation modulus at various percentages of fiber diameter.

The drastic difference in modulus between the skin and core of the fiber proved that the skin was stronger and less elastic than the core. The skin indentation moduli from both mCAF and FAF were neighboring values; however, an immense difference between the two contact area functions stemmed from deeper depths. At the higher depths, the mCAF indentation moduli for Poisson's ratio of 0.30 had the maximum value, whereas the FAF had the lowest. Generally, the indentation moduli calculated from the mCAF at higher contact depths agreed fairly with the elastic modulus of 2.59 GPa from compression tests [18]. Therefore, the mCAF was more significant at higher contact depths, but area correction factors are still a requirement at lower contact depths for improved accuracy.

4.2.2 Kevlar KM2 Fiber

The KM2 depth sections are divided into two depths: 2-13% and 25-40% of fiber diameter (Fig. 4.9). The indentation values for both sections are nearly identical and was a similar trend with the K29 fiber at higher depths. For reference, load-controlled hysteresis curves for these experiments are shown in Appendix B.

Generally, the indentation moduli determined from the mCAF function was higher and agreed reasonably with McAllister's [15] indentation modulus of 6.2 ± 1.0 GPa. McAllister's group [15] implemented a Berkovich indenter tip for indentation on KM2 fibers, but they lacked an area correction factor in their calculations. On the other hand, Cole's group [16] conducted indentations on KM2 Plus fibers with a Berkovich tip although their area correction factors involved a spheroconical tip. Cole's group calculated an indentation modulus of 7.74 ± 0.96 GPa for KM2 Plus and they additionally identified the importance of area correction factors in nanoindentation theory [16]. Overall, the KM2 Plus fibers proved to be stiffer than the core of KM2 fibers.

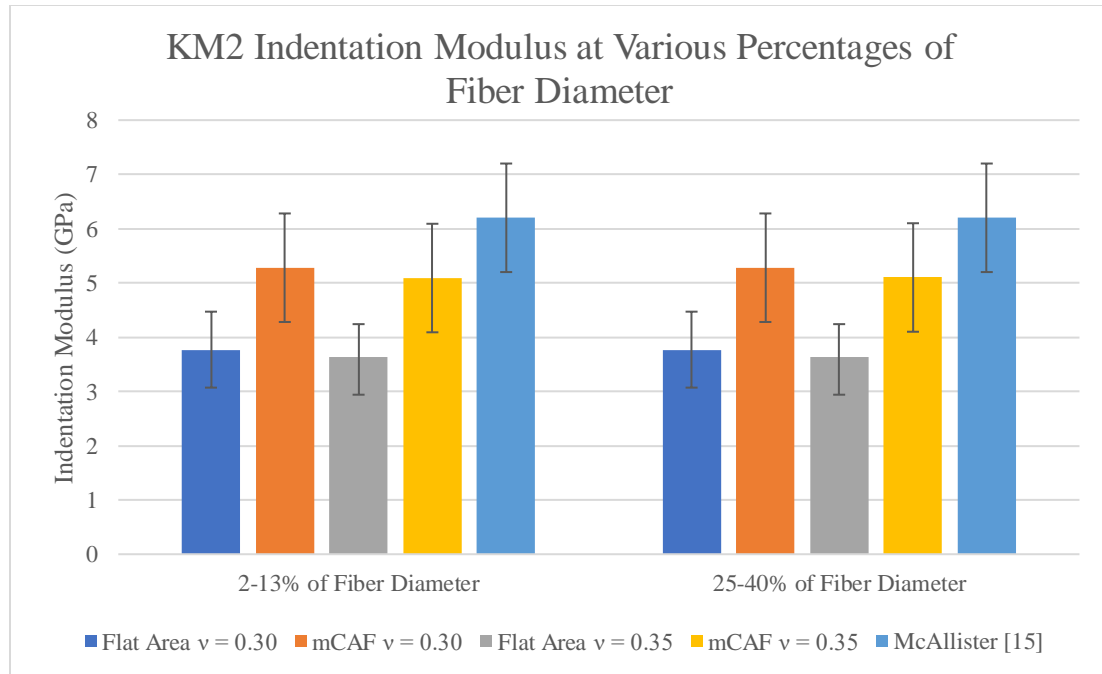


Figure 4.9: KM2 indentation modulus at various percentages of fiber diameter.

4.2.3 Kevlar K119 Fiber

The K119 fiber was distinct from the K29 and KM2 fibers because the skin indentation moduli were closer to those of the core. Data from the FAF had the lowest value for the skin in comparison to that from the mCAF and Kawabata's elastic modulus value of 2.31 GPa [18] (Fig. 4.10). The load-controlled hysteresis curves corresponding to indentation moduli for K119 presented in Tables 4.3 and 4.4 are plotted in Appendix C. In this specific fiber type, the indentation modulus had a closer value to Kawabata's [18] for both the skin and core of the fiber using the mCAF. Although Kawabata [18] conducted compression testing, the indentation moduli values extrapolated from the mCAF provided similar values to that of literature.

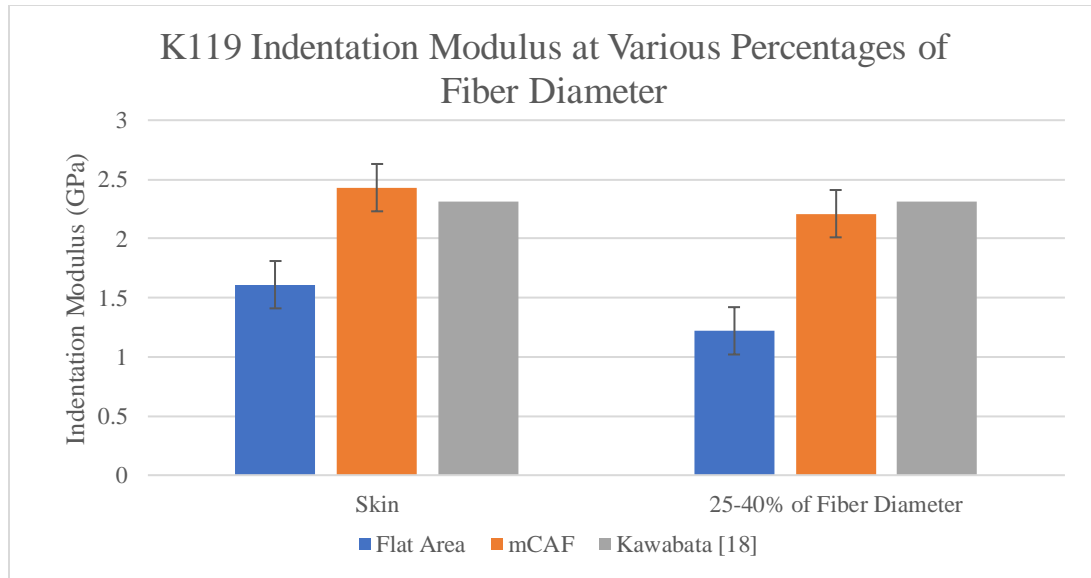


Figure 4.10: K119 indentation modulus at various percentages of fiber diameter.

4.3 PDMS Experimental Results

The PDMS specimen was tested with single and multiple cycle indentation loading. The single cycle tests were necessary to determine the quasi static indentation modulus for literature comparison. Multiple cycle loading was utilized to study frequency dependency in the polymer. The surface roughness of this hydrophilic elastomer was very little since it was molded with glass slides, but still varied at the nanoscale range. PDMS is a very soft polymer with a Poisson's ratio of 0.5 with incompressible characteristics at room temperature [21, 56], hence very low loads were tested (Table 4.5).

Table 4.5: Two nanoindentation methods listed with the load-controlled tests on PDMS.

Load (mN)	Single cycle loading	Multiple cycle loading
1	X	X
2	X	X
3	X	X
4	X	

4.3.1 PDMS – Single Cycle Loading

Low loads of 1mN resulted in a high displacement of 8,310nm further proving this material to be very soft with a low stiffness (Fig. 4.11(a)). This maximum depth was significantly larger than the depth for K29 fibers at 1mN. PDMS was characterized to have a very low indentation modulus compared to any of the Kevlar fibers. Specifically, the average indentation modulus for PDMS was 5.45 ± 0.05 MPa at 1mN.

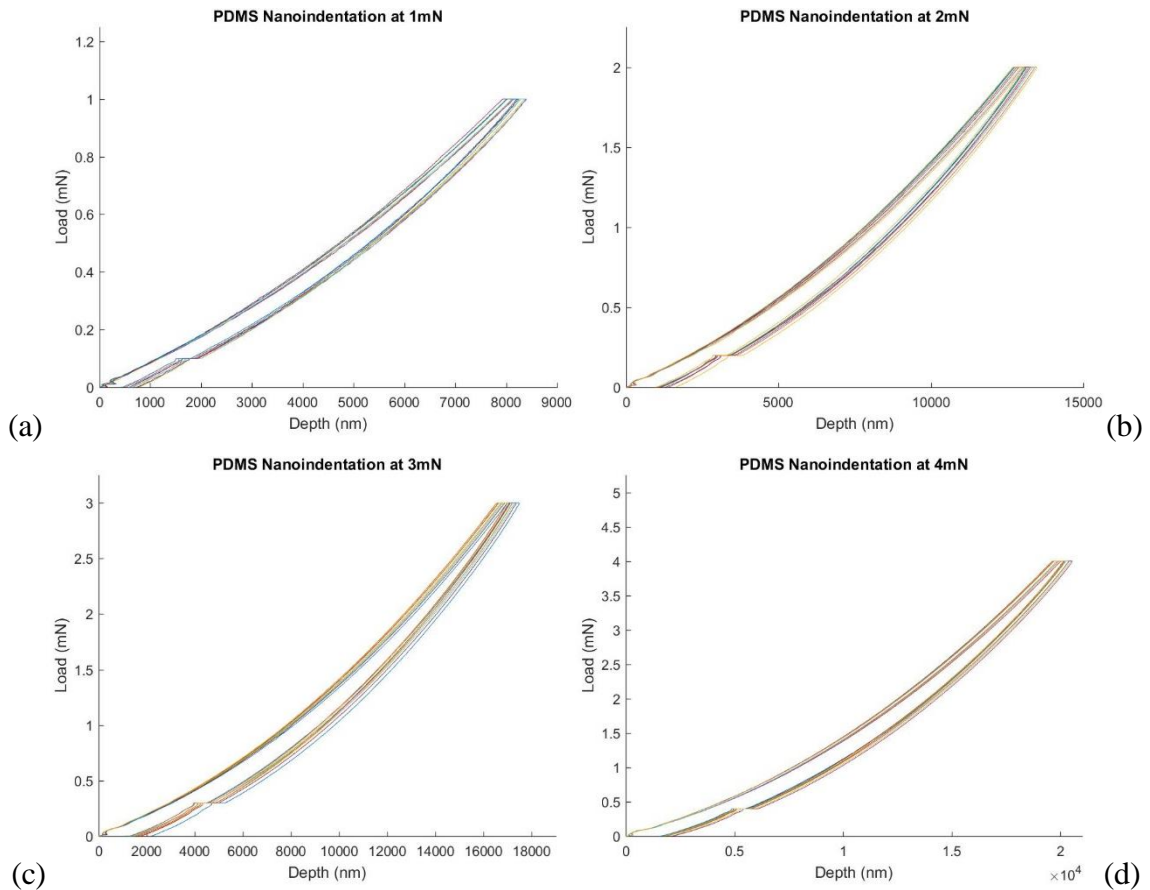


Figure 4.11: PDMS single cycle nanoindentation at (a) 1mN (8 curves), (b) 2mN (10 curves), (c) 3mN (10 curves), and (d) 4mN (10 curves).

The indenter tip reached a maximum average depth of 13,200nm at 2mN and the average indentation modulus at this depth was a slight decrease from the average

indentation modulus at 1 mN (Fig. 4.11(b)). The load-controlled indentations at 3 mN had an average maximum depth of 17,200 nm, only at 1.72% of the specimen's thickness. The hysteresis curves at 3 mN in Fig. 4.11(c) included 10 indents, which were used to determine the stiffness. Similarly, the 4 mN load-controlled indents reached an average maximum depth of 20,300 nm, which was 2.03% of the film thickness. The average indentation modulus at this depth decreased to 3.76 ± 0.04 MPa and their hysteresis curves are shown in Fig. 4.11(d).

Table 4.6: PDMS characterization of indentation modulus and hardness over a range of depths through 1 mm specimen thickness.

Load (mN)	Average Maximum Depth (nm)	Percentage of Thickness (%)	Indentation Modulus (MPa)	Hardness (MPa)
1	$8,310 \pm 100$	0.831	5.45 ± 0.05	2.1 ± 0.15
2	$13,200 \pm 109$	1.32	4.37 ± 0.1	1.4 ± 0.12
3	$17,200 \pm 225$	1.72	3.94 ± 0.06	1.2 ± 0.02
4	$20,300 \pm 250$	2.03	3.76 ± 0.04	1.1 ± 0.04

The average indentation moduli at given loads are listed in Table 4.6 along with corresponding depths and hardness. The maximum percentage of depth characterized for PDMS was 2.03% of the thickness. A visual representation of the average maximum depths plotted with their analogous indentation moduli from Table 4.6 are displayed in Fig. 4.12. The indentation modulus decreased as the average maximum depth increased up to 2.03% of the specimen thickness. Similar trends in reduced modulus of pristine PDMS were seen in Maji's research data [22]. Their study included reduced moduli data on different forms of PDMS. The indentation modulus of 5.84 ± 1.76 MPa at 500 nm was measured with a Berkovich tip [22] and was approximately 5.45 ± 0.05 MPa in the present study corresponding to a depth of 8,310 nm (Table 4.6). Although the depths

vastly differed, the higher depth indicated a lower modulus, as identified in the literature and present study. Likewise, the hardness exhibited a similar trend as the indentation modulus in Fig. 4.13. These graphical trends were identical to those also recognized in other PDMS nanoindentation studies which involved different base to crosslinker ratios, moduli, and hardness [31, 57, 58].

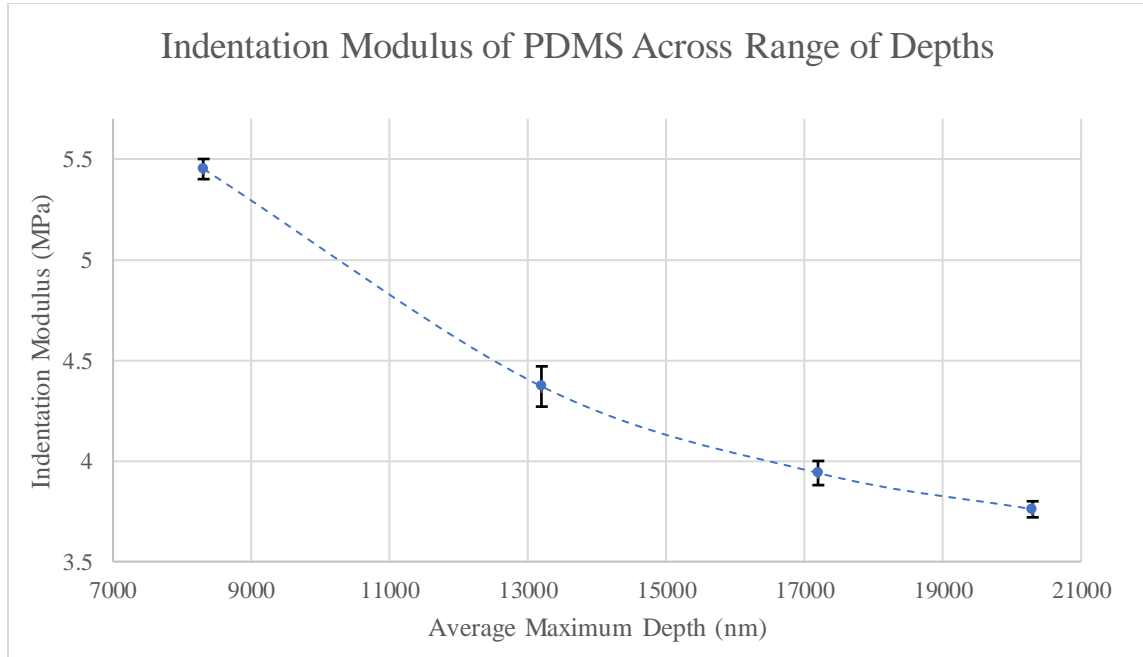


Figure 4.12: Behavior of PDMS indentation modulus across a range of average maximum depths.

Carillo's research group calculated their PDMS specimen with 10:1 crosslinker ratio to have an indentation modulus of 3.64 MPa at 1nm from a conospherical indenter tip [21]. Their tests differed slightly with indenter geometry and loads; however, their quasi static load tests were held at the same holding times as the single cycle loading in the present study [21]. In addition, their experimental procedure along with Maji's [22] included the Hysitron nanoindentation instrument which relies on a continuous stiffness measurement method [59] that utilizes the piezoelectric effect to apply a force.

Conversely, the Vantage does not rely on this method because it uses a magnet and coils to apply a force. These significant differences in experimental procedure explain small discrepancies in data measurements. Overall, the data calculated from the Vantage at 3 and 4mN agree reasonably with the indentation modulus presented by literature [21]. Since data from Carillo [21] and Maji's [22] group considerably agreed, indentation tests validate data acquired on other specimens.

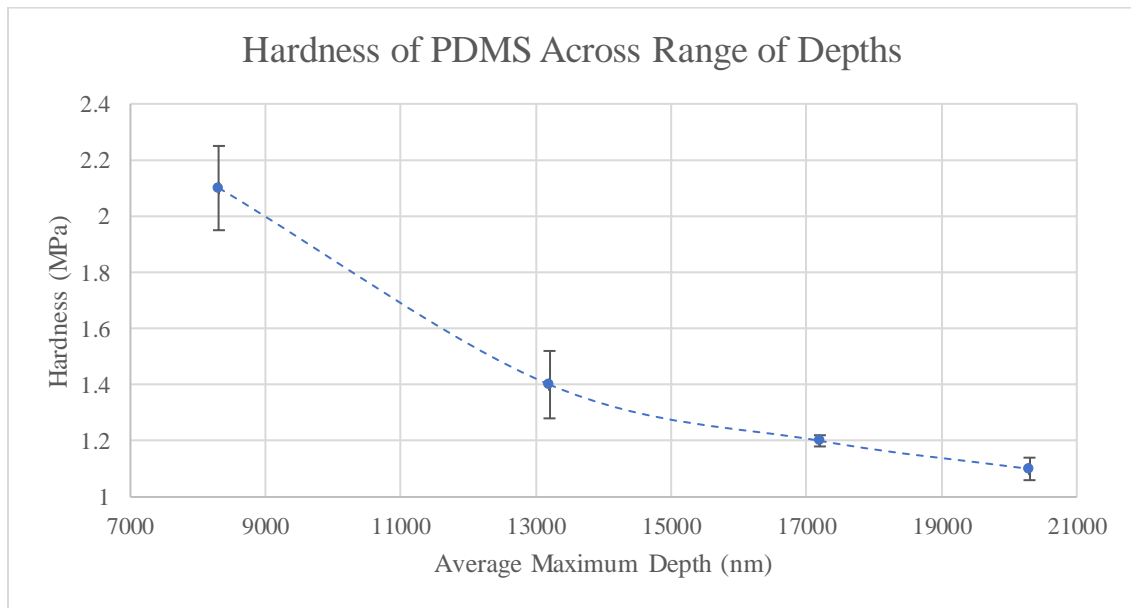


Figure 4.13: Behavior of PDMS hardness across a range of average maximum depths.

4.3.2 PDMS – Multiple Cycle Loading

During multiple cycle loading, the frequency was varied at three different load-controlled experiments. At each frequency, the numbers of cycles were tabulated in Table 4.7 along with their corresponding indentation moduli minimum and maximum values. Every frequency at a given load was tested with 5, 50, and 100 cycles each to study the impact of varied cycles on indentation moduli and hardness. Three different frequencies were tested to examine the influence of time dependency on the elastomer.

Table 4.7: Multiple cycle indentation load-controlled tests for PDMS at frequencies of 1, 0.5, and 0.033Hz. Each frequency test was performed with 5, 50, and 100 cycles. Each test had a corresponding maximum and minimum indentation modulus.

Load (mN)	Frequency (Hz)	Cycles	E _s (MPa)		Cycles	E _s (MPa)		Cycles	E _s (MPa)	
			Min	Max		Min	Max		Min	Max
1	1	5	6.34	6.64	50	5.64	6.20	100	5.28	6.14
	0.5	5	6.42	6.70	50	5.38	5.96	100	4.98	6.10
	0.033	5	5.26	5.68	50	2.60	5.40	100	1.58	5.28
2	1	5	5.02	5.26	50	4.64	5.10	100	4.34	4.94
	0.5	5	4.92	5.12	50	4.38	4.86	100	4.12	4.94
	0.033	5	4.08	4.48	50	2.24	4.4	100	1.50	4.50
3	1	5	4.48	4.72	50	4.20	4.56	100	4.02	4.52
	0.5	5	4.38	4.56	50	3.96	4.36	100	3.70	4.40
	0.033	5	3.72	4.02	50	2.14	4.06	100	1.38	3.88

Progressing from Fig. 4.14(a) to Fig 4.14(c), the loading and unloading curves became smoother at 1 mN load-controlled indents. This could be attributed by the viscoelastic recovery which does not have time to stabilize at higher frequencies. Although the bump (in Fig. 4.14(a) and (b)) from the loading curve between 0 and 1,000nm did not disappear in Fig 4.14(c), it still diminished and appeared stable. The remainder of hysteresis multiple cycle loading curves are plotted in Appendix D and exhibited similar trends in loading curves as those seen in Fig. 4.14.

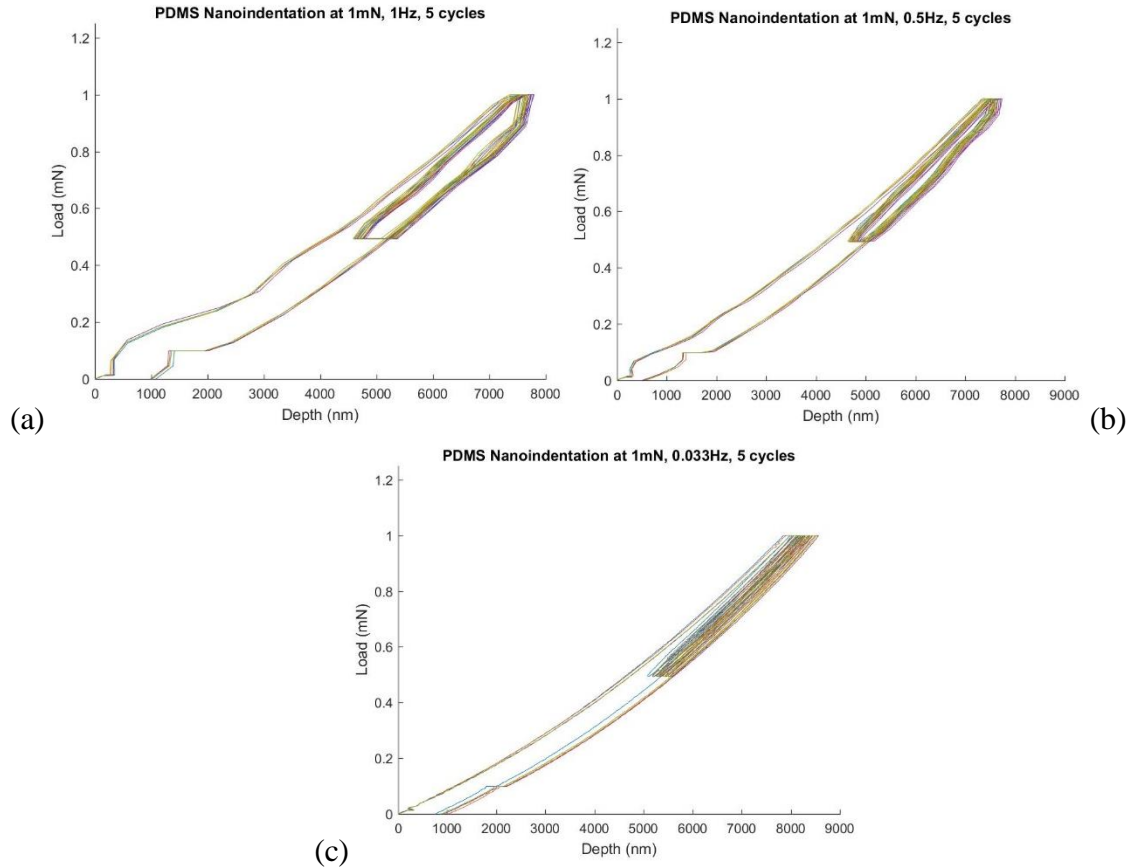


Figure 4.14: PDMS multiple cycle nanoindentation at 1mN and 5 cycles with varying frequencies of (a) 1Hz (5 curves), (b) 0.5Hz (5 curves), (c) 0.033Hz (5 curves).

The maximum and minimum indentation moduli listed in Table 4.7 at 1 mN for 5, 50, and 100 cycles were extracted from Fig. 4.15. The frequency decreased as the average maximum depth increased and the relationship between this behavior was attributed to creep. With a longer holding time, creep occurred and increased the maximum depth. In higher frequencies, such as 1 and 0.5Hz, there was no dwell period at maximum load. A lack of dwell period with a quick loading time prevented the polymer from viscoelastic recovery and resulted in the jagged loading and unloading curves (Fig. 4.14(a) and (b)). In Fig. 4.15, the 1 and 0.5Hz data were relatively at closer depths since large scale creep did not occur as opposed to 0.033Hz loading tests. As the average maximum depth

increased, the indentation moduli slowly decreased in a power law trend. Increasing the number of cycles increased the average maximum depth in the specimen. At 5 cycles, most of the trends were linear since the difference in depths were not drastic. Conversely, power law trends were clearly visible at 50 and 100 cycles.

The indentation moduli at 1mN were graphed for constant frequencies of 1, 0.5, and 0.033Hz in Fig. 4.16. The lower cycles typically initiated at a lower average maximum depth because it involved a combination of stress relaxation and surface roughness. Indentation moduli also decreased with an increase in average maximum depth in Fig. 4.16 because of energy loss. At smaller ranges in depth, indentation moduli exhibited a linear trend with a negative slope (Fig. 4.16(a) and (b)). However, the larger depths at 0.033Hz displayed a power law trend in respect to the indentation modulus, as shown in Fig. 4.16(c). These patterns were also evident in the hardness in Fig. 4.17 (for cycle trends) and 4.18 (for frequency trends). The load-controlled data yielded from 2 and 3mN indentations were graphed in the similar fashion as the 1mN load tests. The indentation data at 2mN for constant cycles and frequencies are displayed in Fig. 4.19 and 4.20, respectively. The hardness graphs at 2mN are shown in Fig. 4.21 and 4.22. Correspondingly, the 3mN load-controlled test data is depicted in Fig. 4.23 through 4.26.

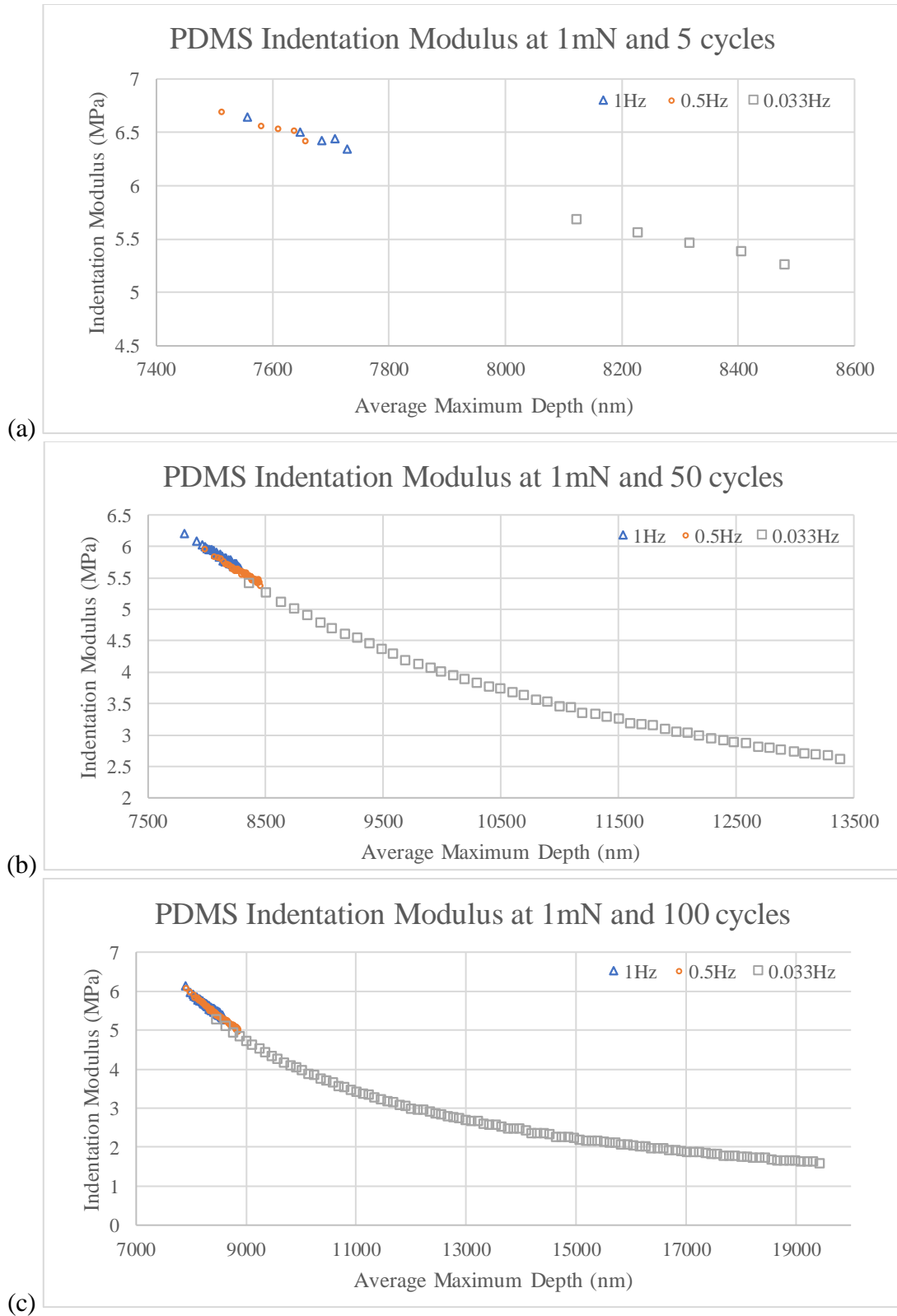


Figure 4.15: PDMS indentation modulus graphs at 1mN with various frequencies at (a) 5 cycles, (b) 50 cycles, and (c) 100 cycles.

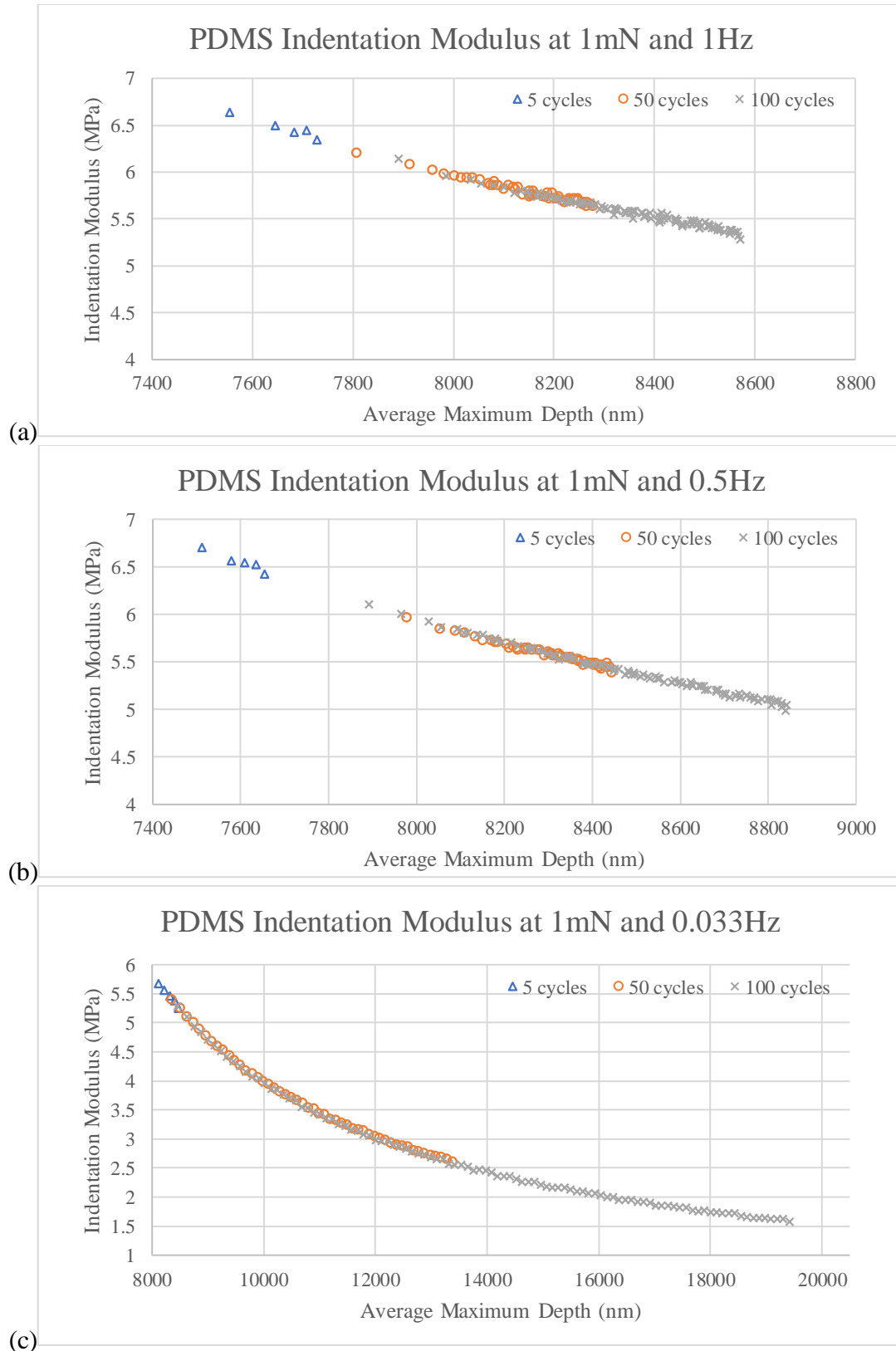


Figure 4.16: PDMS indentation modulus graphs at 1mN with various cycles at (a) 1Hz, (b) 0.5Hz, and (c) 0.033Hz.

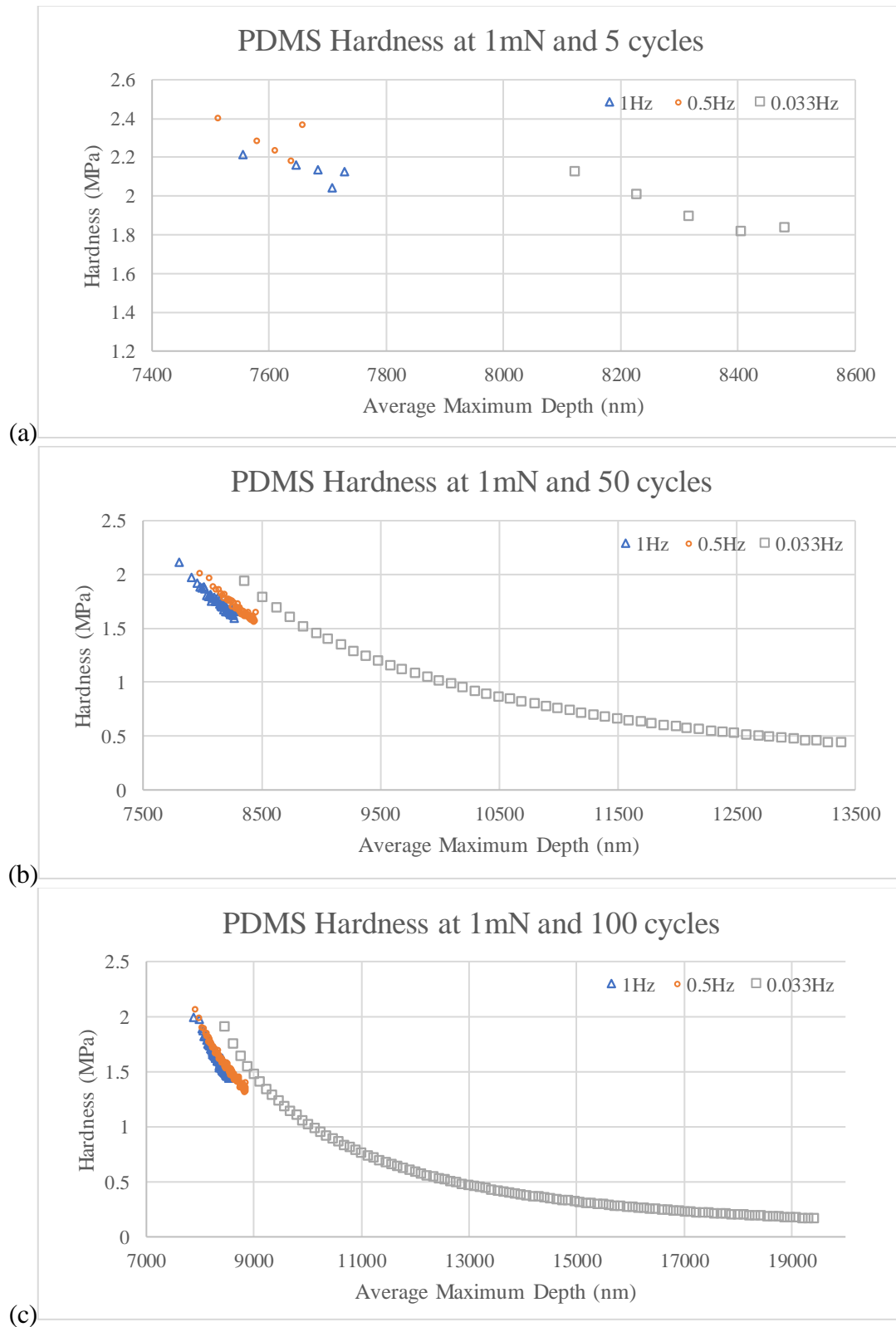


Figure 4.17: PDMS hardness graphs at 1mN with various frequencies at (a) 5 cycles, (b) 50 cycles, and (c) 100 cycles.

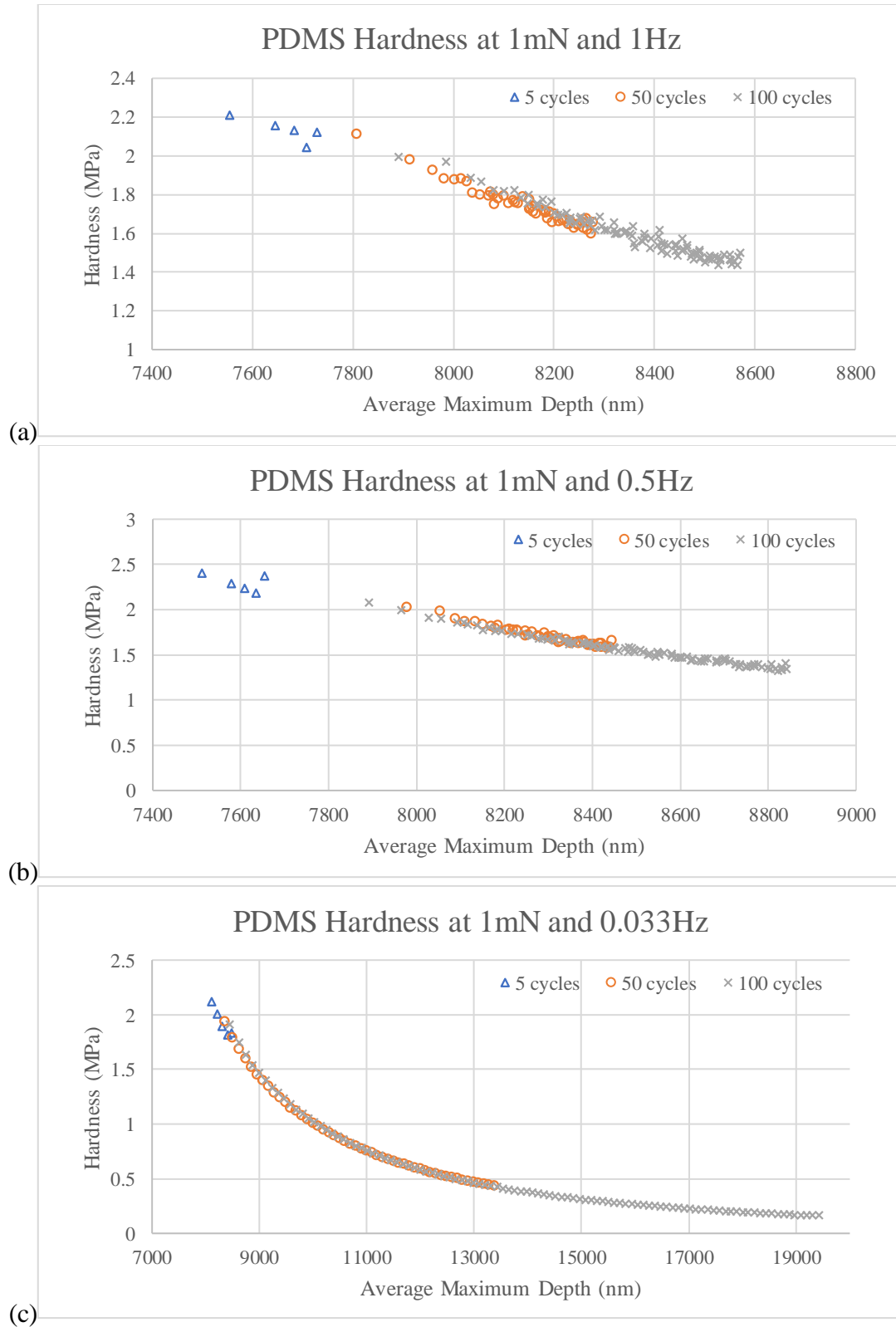


Figure 4.18: PDMS hardness graphs at 1mN with various cycles at (a) 1Hz, (b) 0.5Hz, and (c) 0.033Hz.

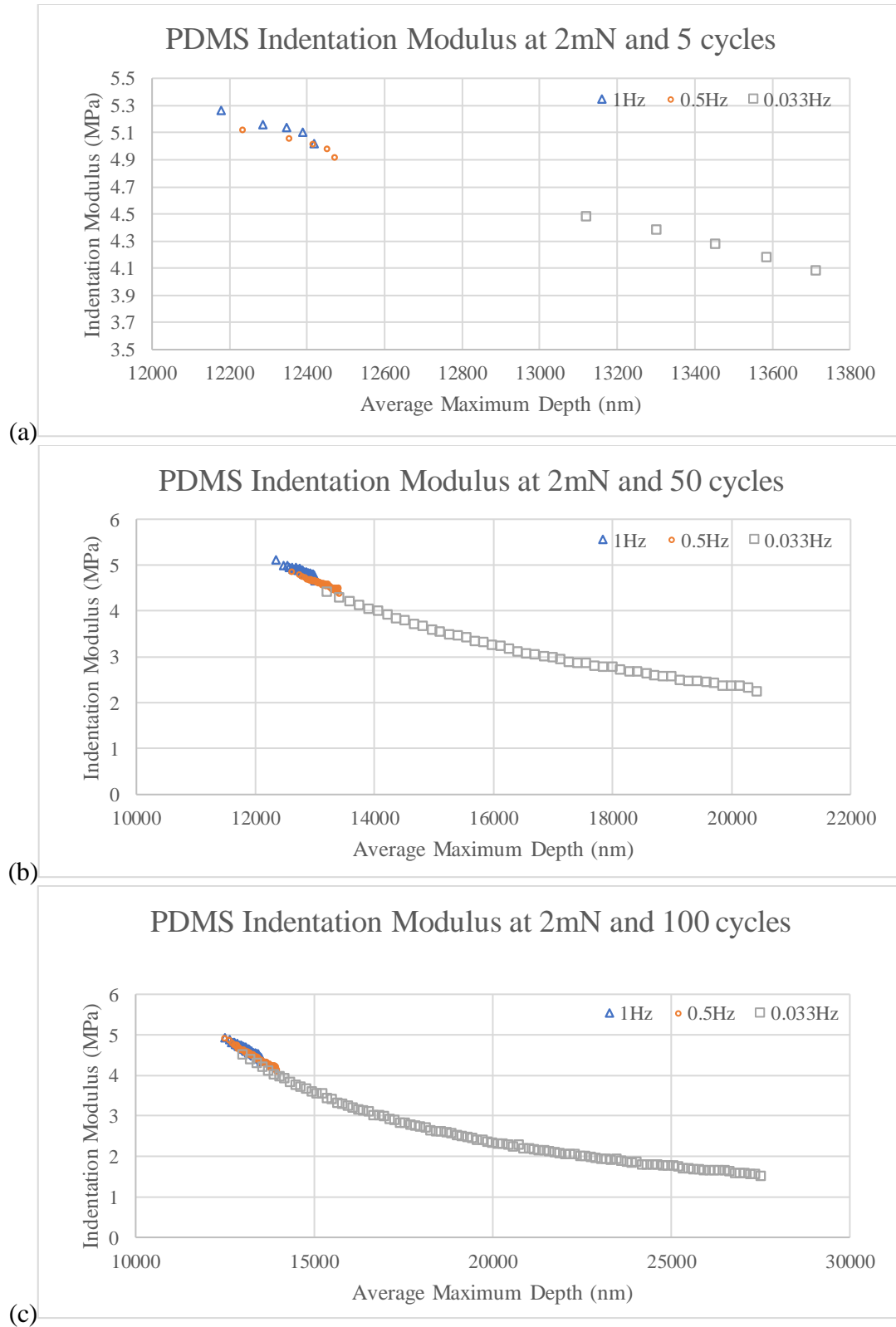


Figure 4.19: PDMS indentation modulus graphs at 2mN with various frequencies at (a) 5 cycles, (b) 50 cycles, and (c) 100 cycles.

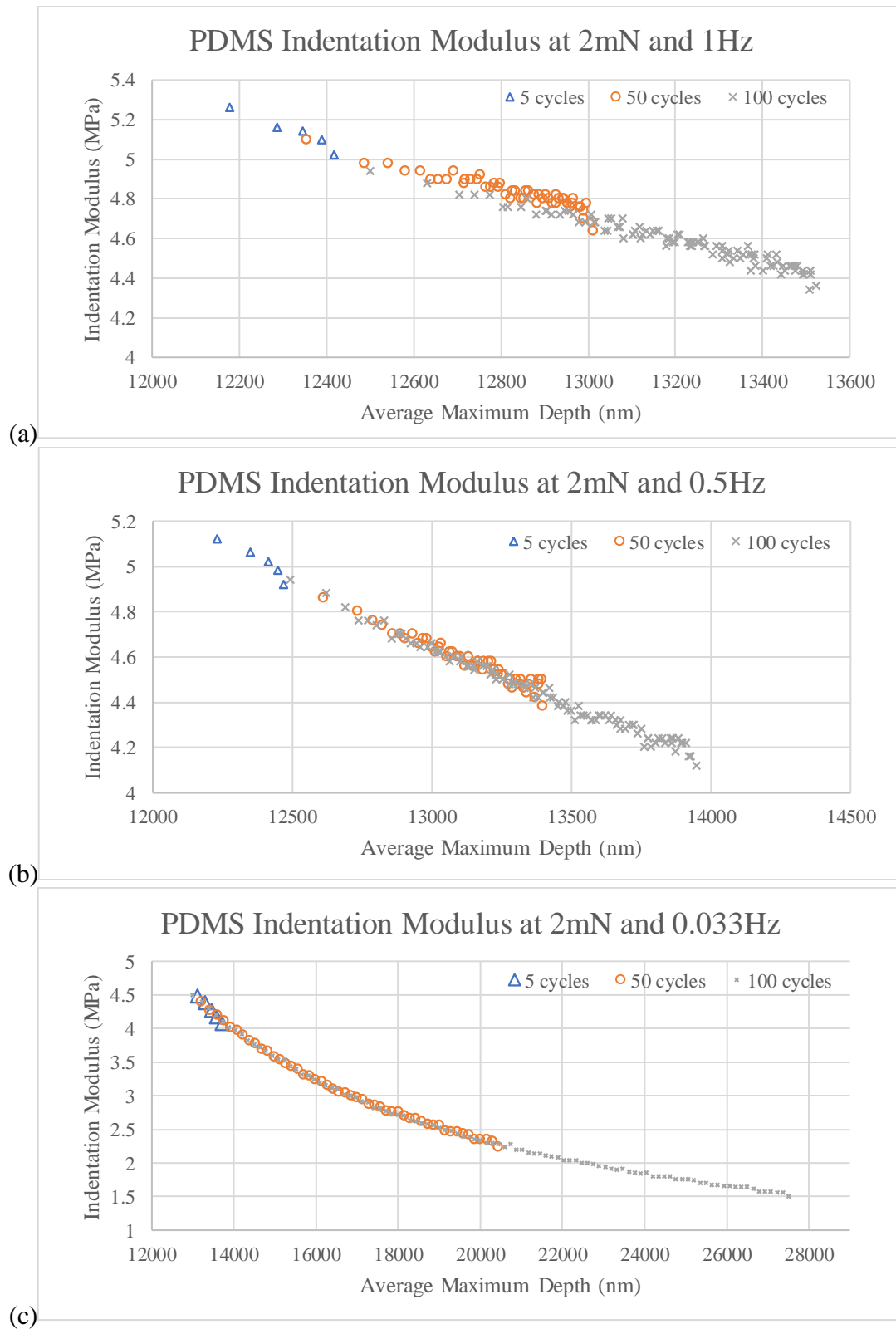


Figure 4.20: PDMS indentation modulus graphs at 2mN with various cycles at (a) 1Hz, (b) 0.5Hz, and (c) 0.033Hz.

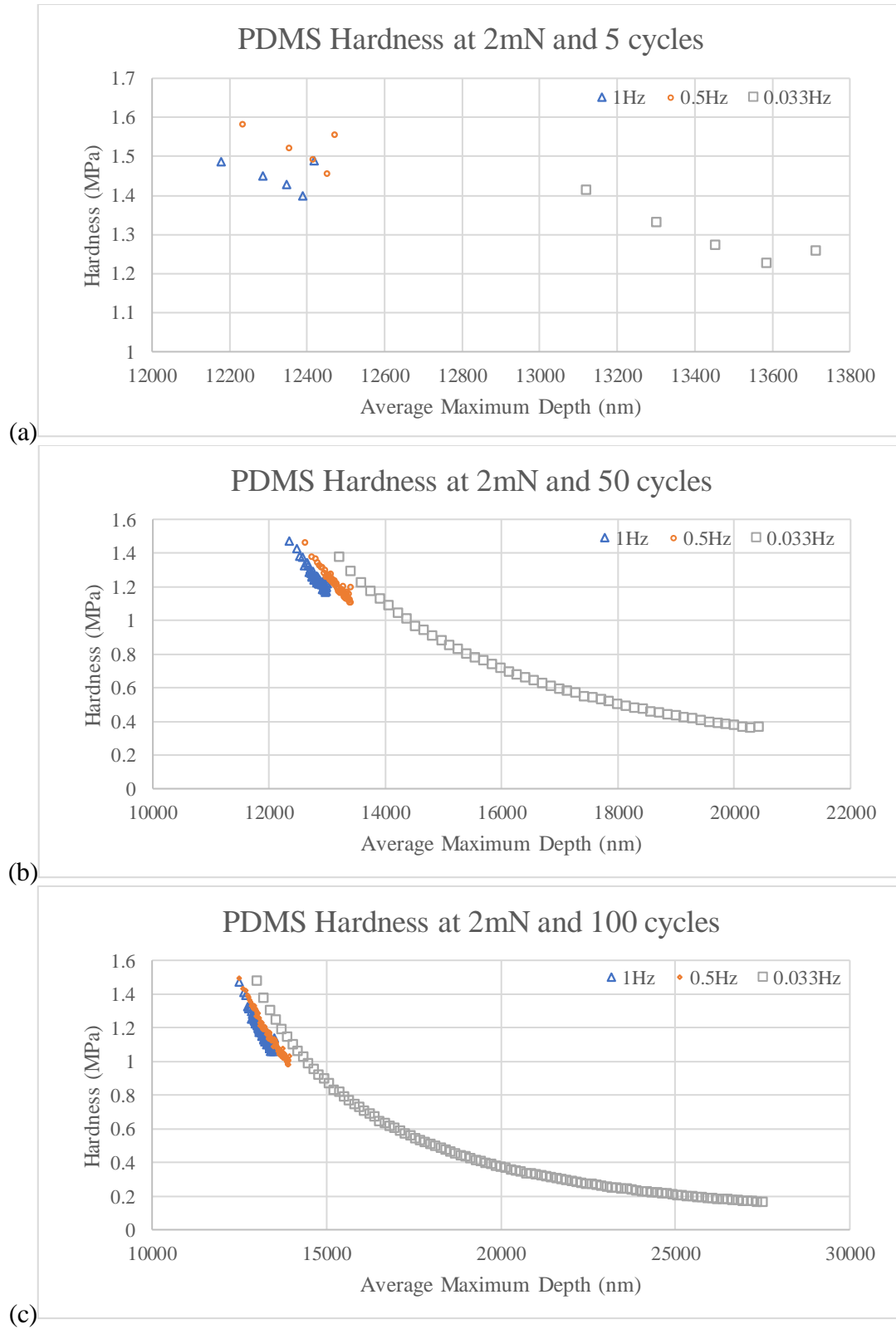


Figure 4.21: PDMS hardness graphs at 2mN with various frequencies at (a) 5 cycles, (b) 50 cycles, and (c) 100 cycles.

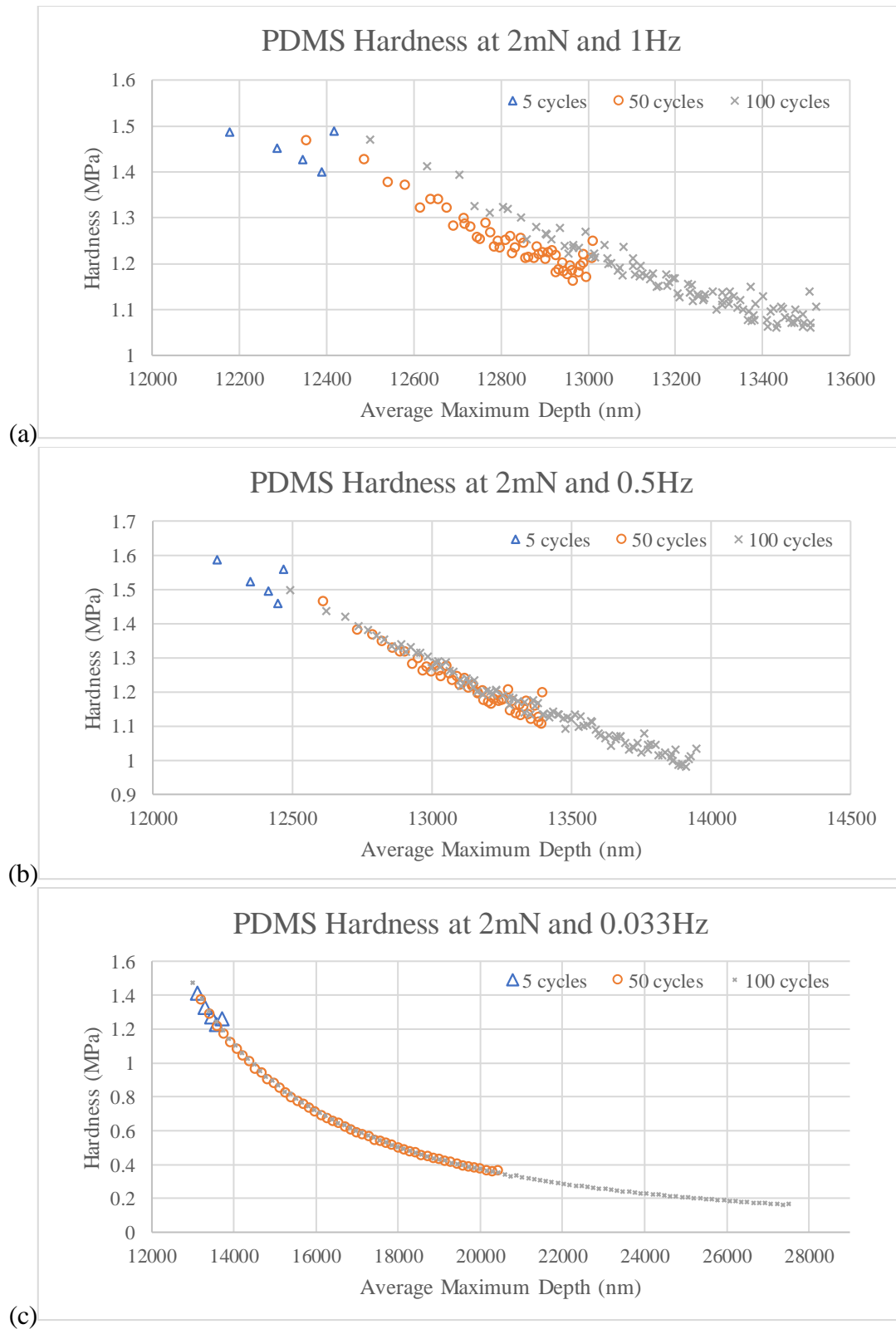


Figure 4.22: PDMS hardness graphs at 2mN with various cycles at (a) 1Hz, (b) 0.5Hz, and (c) 0.033Hz.

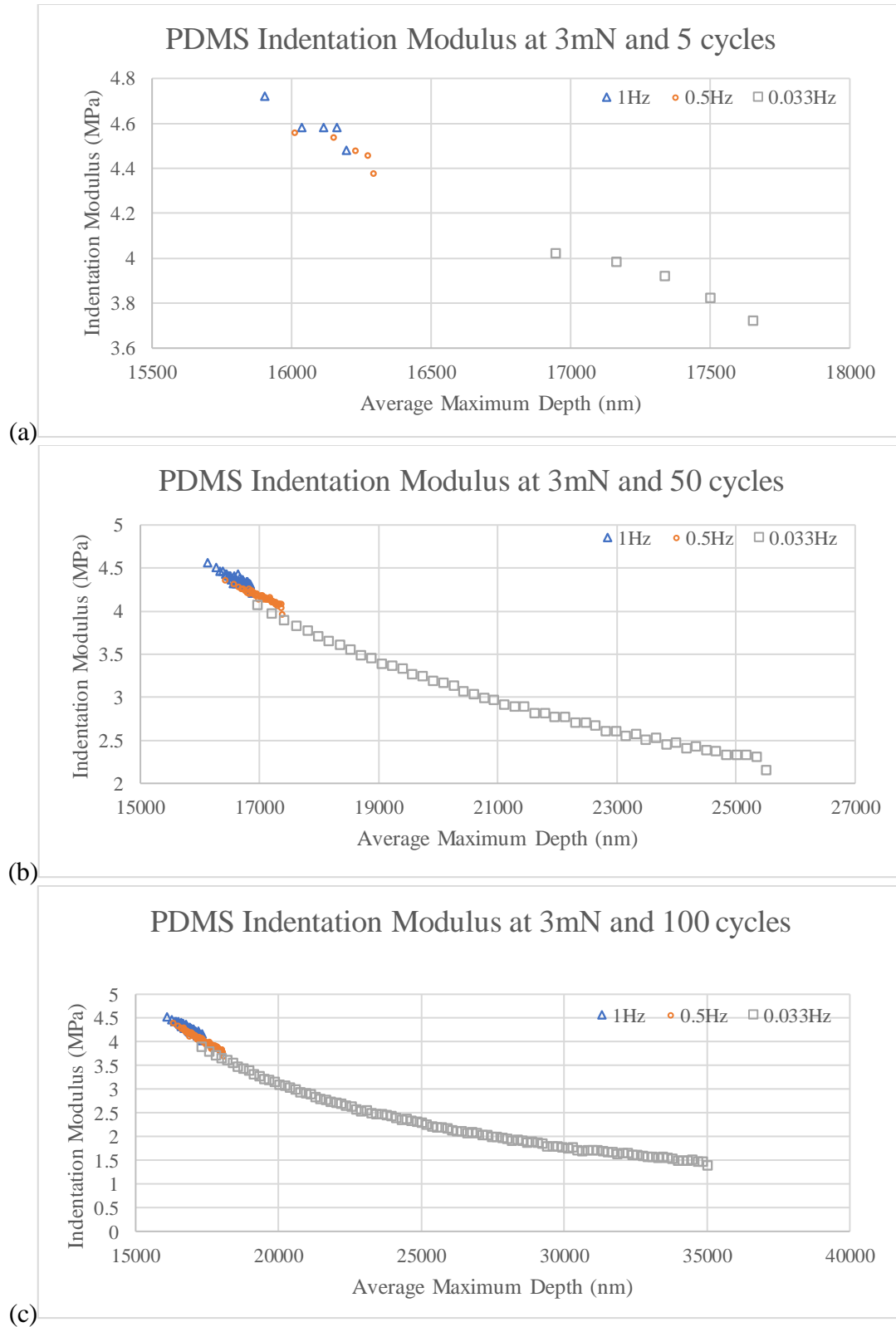


Figure 4.23: PDMS indentation modulus graphs at 3mN with various frequencies at (a) 5 cycles, (b) 50 cycles, and (c) 100 cycles.

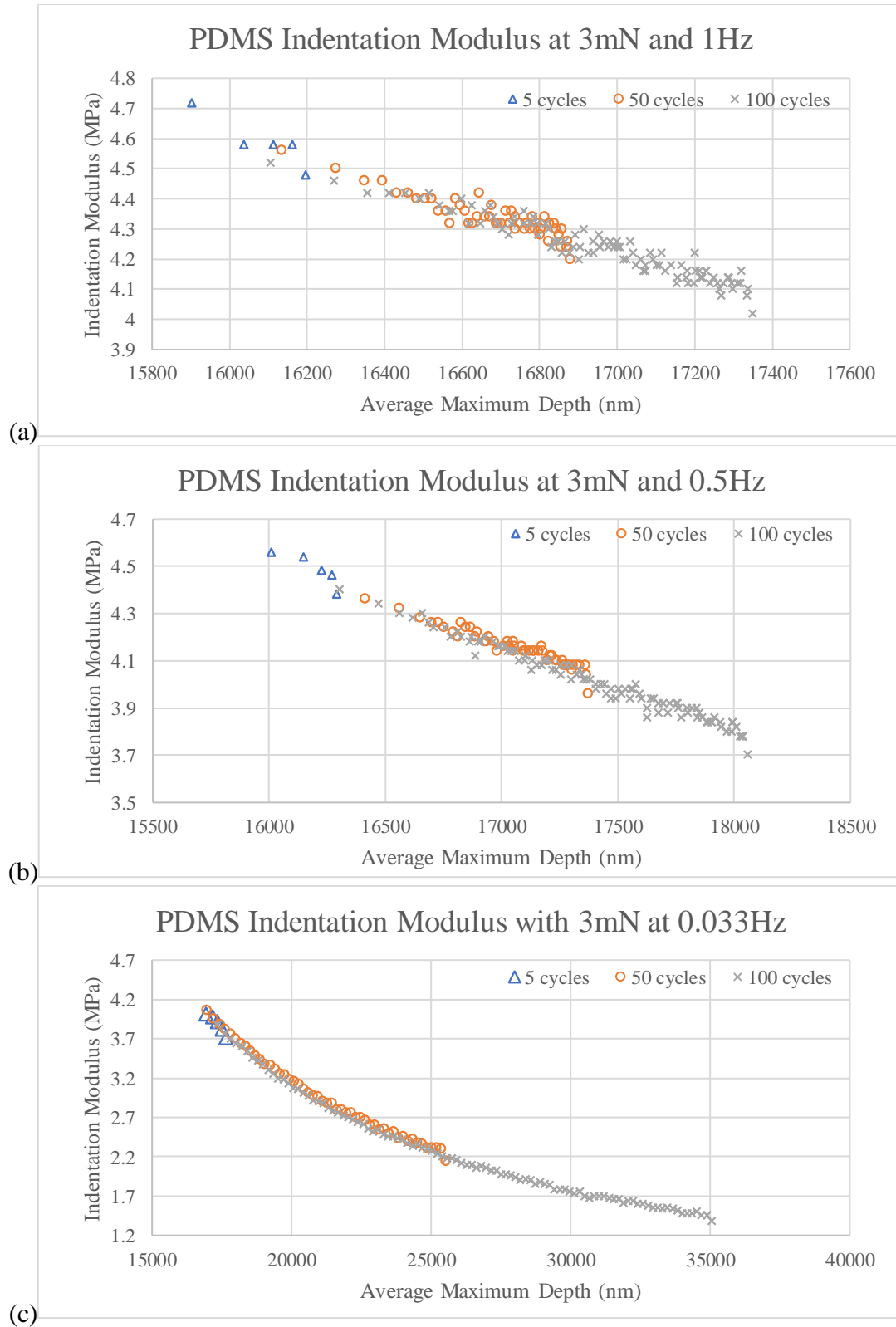


Figure 4.24: PDMS indentation modulus graphs at 3mN with various cycles at (a) 1Hz, (b) 0.5Hz, and (c) 0.033Hz.

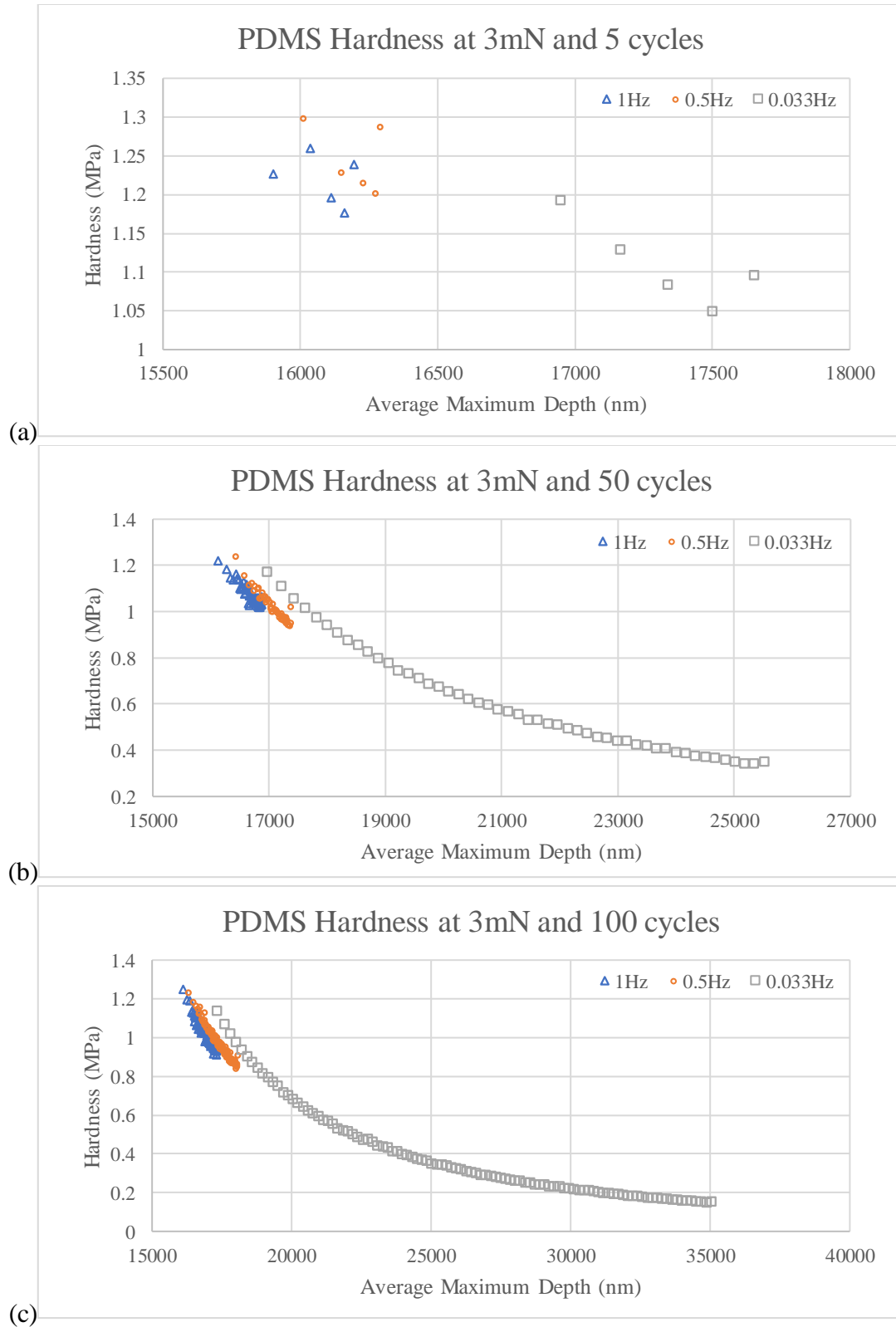


Figure 4.25: PDMS hardness graphs at 3mN with various frequencies at (a) 5 cycles, (b) 50 cycles, and (c) 100 cycles.

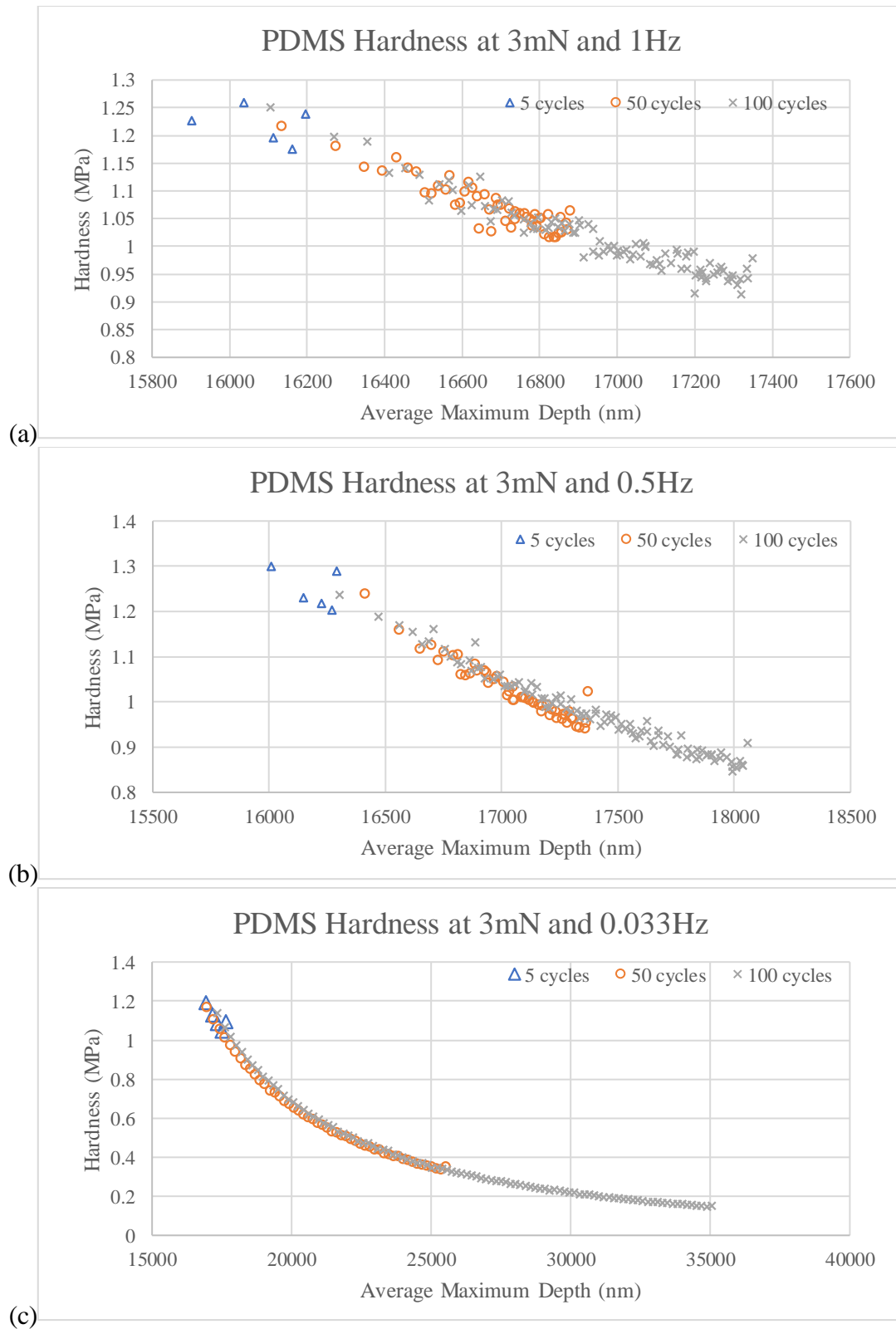


Figure 4.26: PDMS hardness graphs at 3mN with various cycles at (a) 1Hz, (b) 0.5Hz, and (c) 0.033Hz.

4.4 SMP Experimental Results

Two types of indentation methods were tested on the SMP specimens. The first method involved single cycle loading and was conducted at the following load-controlled tests listed in Table 4.8. Three different loads: 3, 10, and 50mN were specifically selected for studying frequency dependency in multiple cycle loading. The variety in loads provided an assortment of data ranging from low to high loads. From laboratory dynamic mechanical analysis (DMA) testing, the Poisson's ratio was specifically estimated as 0.44 for this hydrophilic specimen.

Table 4.8: Two nanoindentation methods listed with the load-controlled tests on SMP.

Load (mN)	Single cycle loading	Multiple cycle loading
2	X	
3	X	X
4	X	
5	X	
10	X	X
20	X	
30	X	
50	X	X
100	X	
200	X	
250	X	
300	X	

4.4.1 SMP – Single Cycle Loading

Although its softness did not compare to the PDMS, the SMP was able to resist higher loads to collect more load-controlled data. Indentations from 2 to 300mN were completed on the SMP (Table 4.8) and single cycle loading curves at 2, 3, 4, and 5mN are shown in Fig. 4.27.

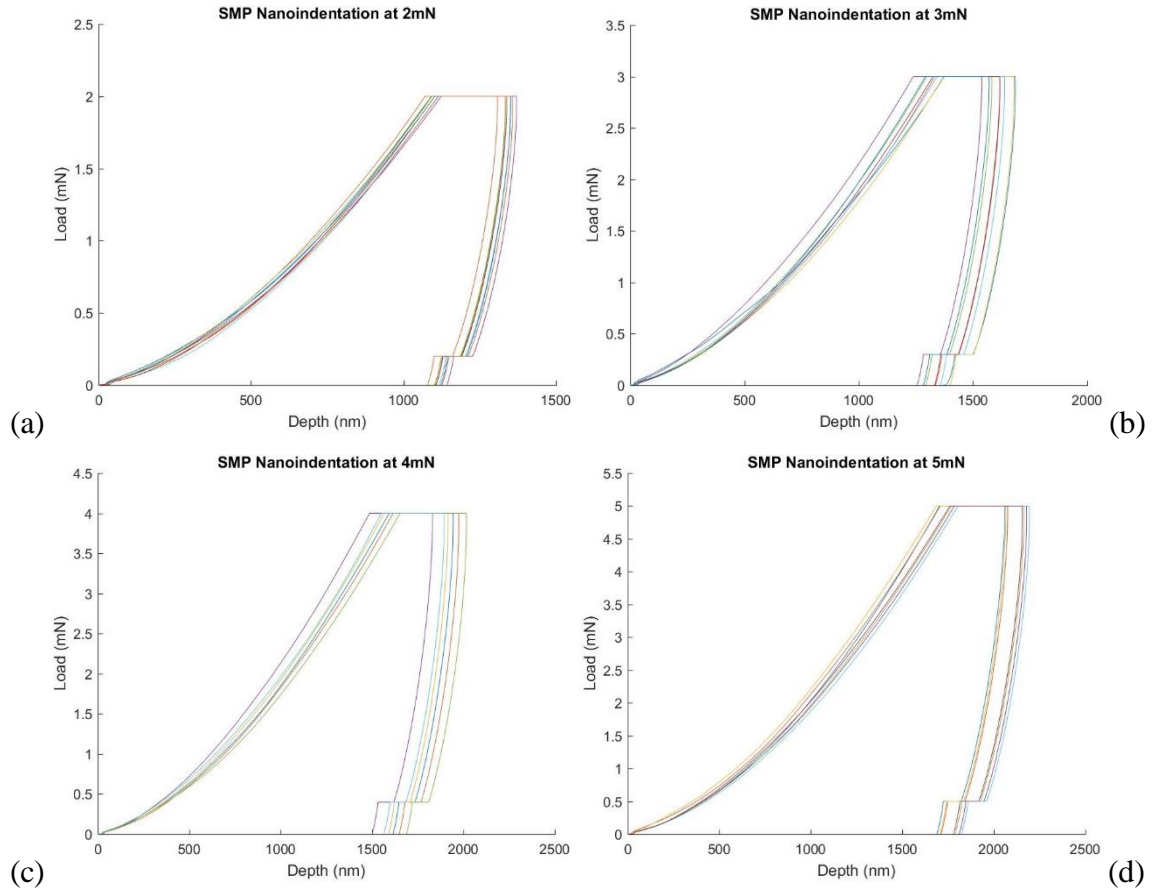


Figure 4.27: SMP single cycle nanoindentation at (a) 2mN (9 curves), (b) 3mN (8 curves), (c) 4mN (6 curves), and (d) 5mN (7 curves).

The higher loads of 10, 20, 30, and 50mN are graphed in Fig. 4.28 and exhibited identical loading curves as portrayed in Fig. 4.27. At even higher loads, the displacement was relatively miniscule compared to the displacement for PDMS single cycle tests at low loads (Fig. 4.29). From this behavior, the PDMS specimen was confirmed to be softer than the SMP.

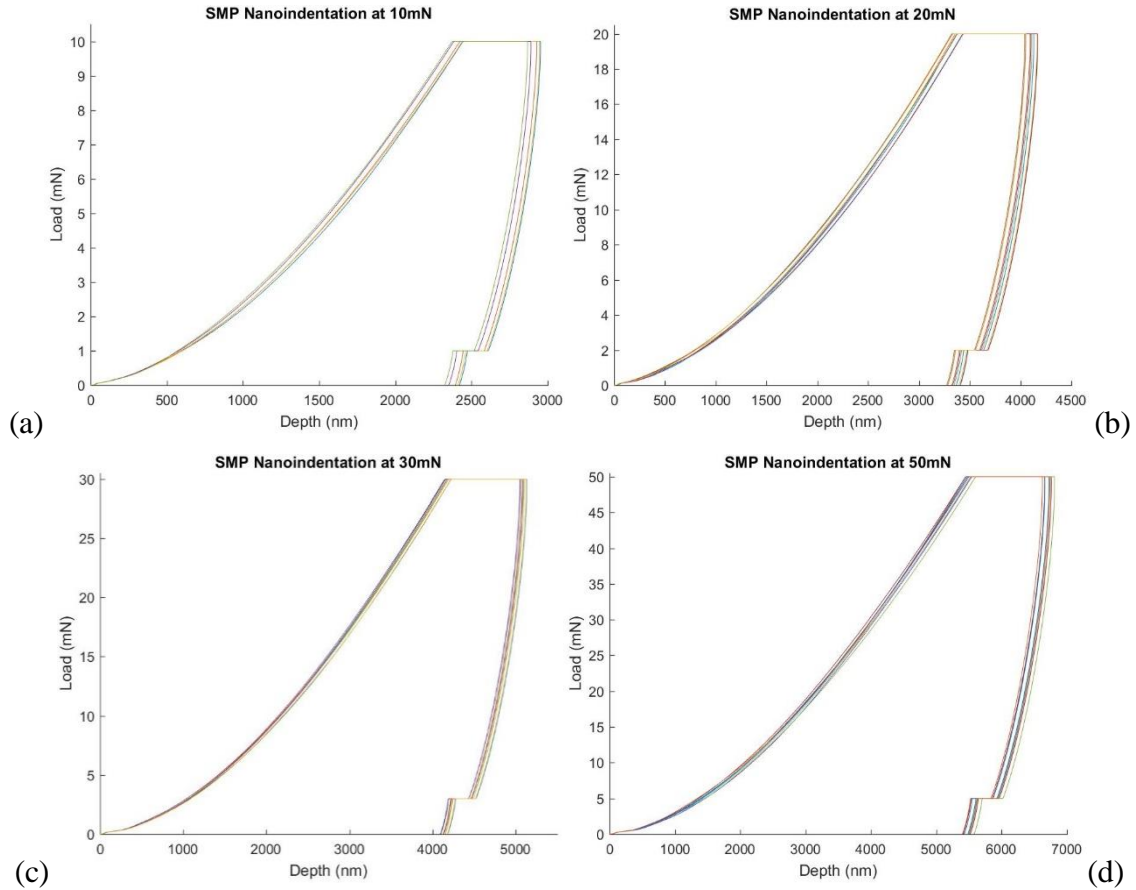


Figure 4.28: SMP single cycle nanoindentation at (a) 10mN (5 curves), (b) 20mN (10 curves), (c) 30mN (10 curves), and (d) 50mN (9 curves).

The corresponding indentation moduli, hardness, and depths for each set of loads was organized in Table 4.9. The depth was compared to the thickness of the specimen and was provided as a percentage in that table. The maximum load of 300mN only pierced about 1.937% of the specimen's thickness, whereas only a 4mN load test reached roughly the same percentage in the PDMS. This drastic comparison portrays the SMP as a stronger and vigorous specimen which can resist higher loads. PDMS ultimately exhibited more elasticity than the SMP because of its low indentation modulus.

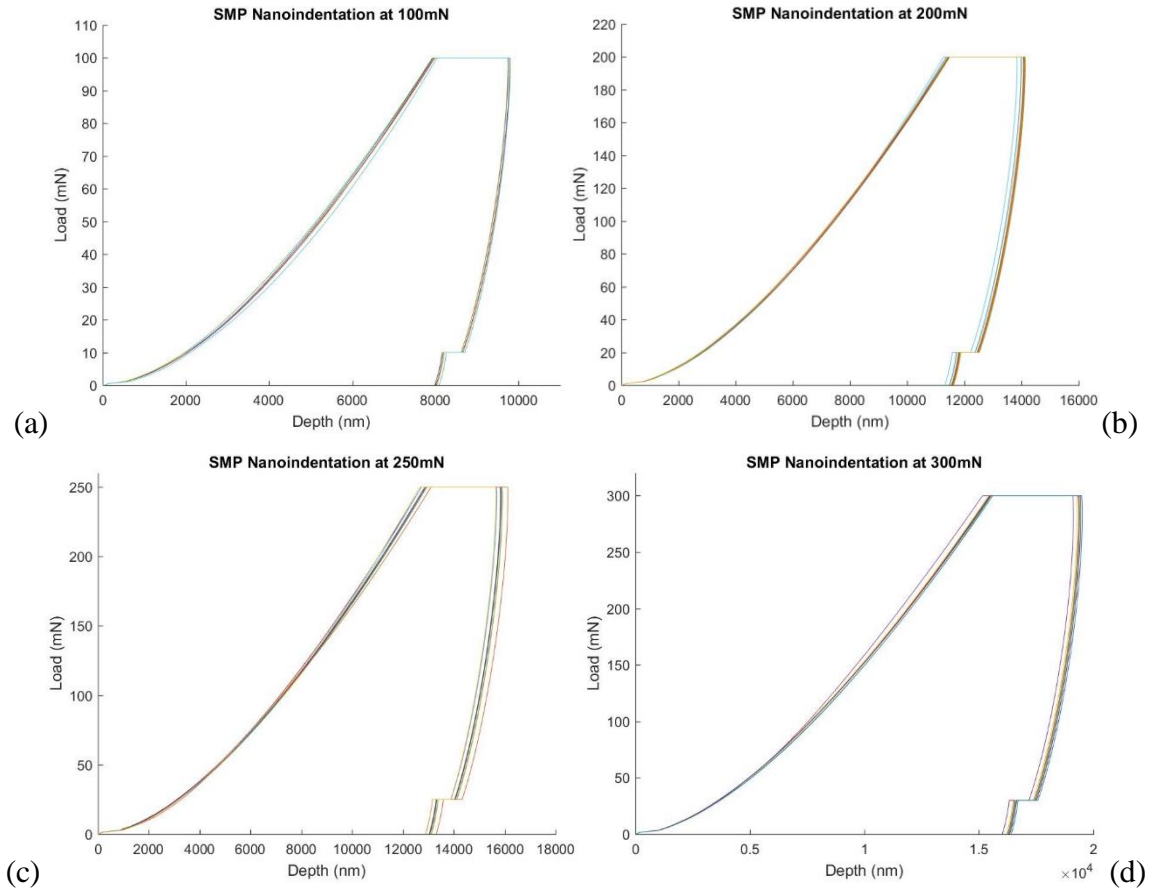


Figure 4.29: SMP single cycle nanoindentation at (a) 100mN (6 curves), (b) 200mN (10 curves), (c) 250mN (10 curves), and (d) 300mN (8 curves).

At a range from 1,342nm to 4,108nm, the indentation modulus was relatively constant around 2 GPa, but decreased as the depth increased. Although the decrease was not as consistent as the behavior in PDMS, the SMP had its lowest measured indentation modulus of 1.62 GPa at 19,374nm. The hardness did not display a similar decreasing trend, instead it remained around 0.044 GPa. Small fluctuations in surface area and stress relaxation were likely culprits of this discrepancy. The polymer was generally able to creep and conform to the indentation load, displaying smooth loading and unloading curves in Fig. 4.27 through 4.29.

Table 4.9: SMP characterization of indentation modulus and hardness over a range of depths through 1mm specimen thickness.

Load (mN)	Average Maximum Depth (nm)	Percentage of Thickness (%)	Indentation Modulus (GPa)	Hardness (GPa)
2	1342.8 ± 8	0.134	2.06 ± 0.04	0.045 ± 0.002
3	1620 ± 78	0.162	2.07 ± 0.08	0.048 ± 0.004
4	1930 ± 87	0.193	2.03 ± 0.05	0.045 ± 0.004
5	2130 ± 66.5	0.213	2.04 ± 0.07	0.046 ± 0.002
10	2920 ± 51.5	0.292	2.03 ± 0.02	0.050 ± 0.001
20	4108 ± 66.7	0.411	2.03 ± 0.004	0.051 ± 0.002
30	5093 ± 39	0.510	1.96 ± 0.006	0.050 ± 0.001
50	6692 ± 100	0.669	1.9 ± 0.06	0.049 ± 0.002
100	9965 ± 283	0.997	1.85 ± 0.05	0.043 ± 0.003
200	14051 ± 81	1.405	1.78 ± 0.008	0.044 ± 0.001
250	15839 ± 292	1.584	1.77 ± 0.008	0.044 ± 0.001
300	19374 ± 142	1.937	1.62 ± 0.013	0.034 ± 0.001

The indentation moduli from Table 4.9 were graphed in Fig. 4.30 for a visual representation of the decreasing trend. Some instability in moduli were depicted between depths of 1,342nm to 2,130nm. The indentation moduli constantly decreased after 4,108nm of indentation depth. The trend between hardness and average maximum depth was additionally plotted in Fig. 4.31. The first four points of hardness exhibited some small instability and subsequently inflated to a maximum of 0.051 GPa at a load of 20mN. The minimum hardness was located at the maximum depth of 19,374nm, which also corresponded to the location of the minimum indentation modulus.

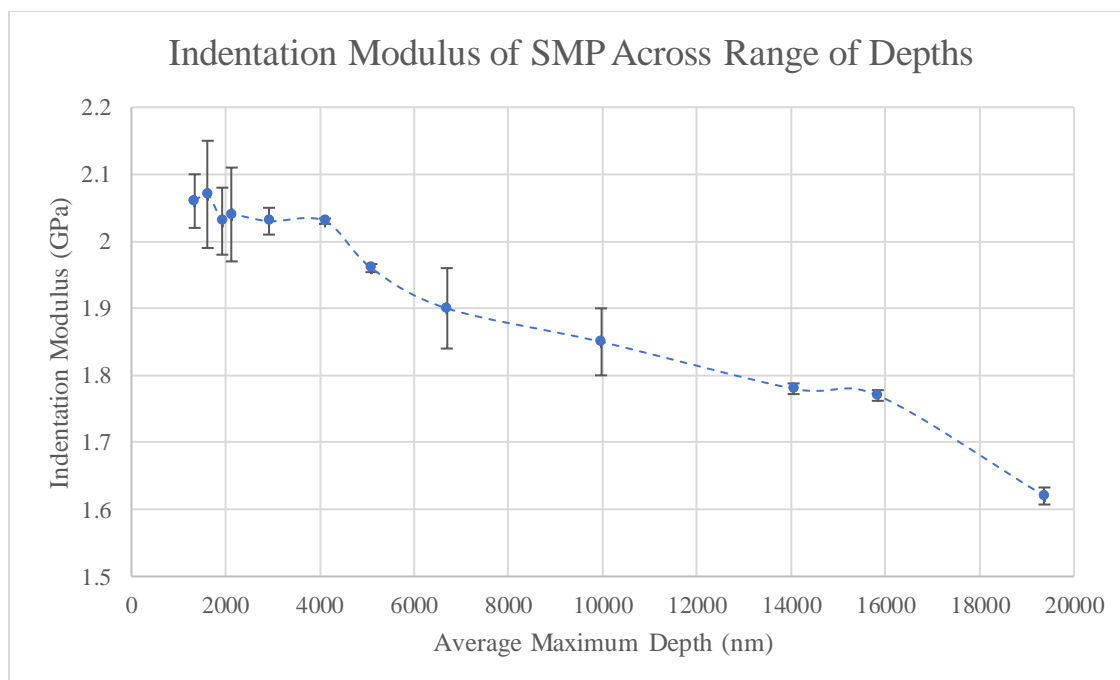


Figure 4.30: Behavior of SMP indentation modulus across a range of average maximum depths.

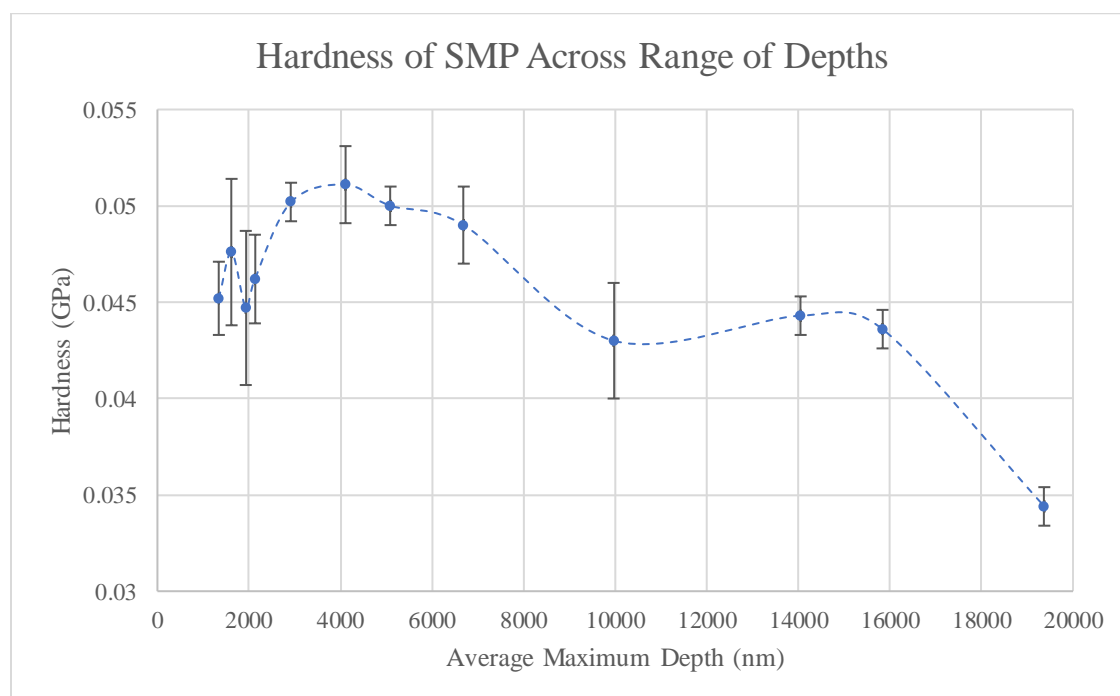


Figure 4.31: Behavior of SMP hardness across a range of average maximum depths.

4.4.2 SMP – Multiple Cycle Loading

The multiple cycle loading tests of 3, 10, and 50mN were performed at 1, 0.5, and 0.033Hz. The parameters for each loading test were listed in Table 4.10 with their corresponding minimum and maximum indentation moduli at specified cycles. The global minimum of 0.64 GPa was measured at 50mN, 0.033Hz, and 100 cycles. Conversely, a global maximum of 3.35 GPa was determined at 3mN, 1Hz, and 5 cycles. These minima and maxima pursued trends previously stated with single cycle loading, whereas the lower loads and faster frequencies resulted in higher indentation moduli.

Table 4.10: Multiple cycle indentation load-controlled tests for SMP at frequencies of 1, 0.5, and 0.033Hz. Each frequency test was performed with 5, 50, and 100 cycles. Each test had a corresponding maximum and minimum indentation modulus.

Load (mN)	Frequency (Hz)	Cycles	E _s (GPa)		Cycles	E _s (GPa)		Cycles	E _s (GPa)	
			Min	Max		Min	Max		Min	Max
3	1	5	2.48	3.35	50	1.89	3.25	100	1.94	3.19
	0.5	5	2.19	3.14	50	1.82	3.40	100	1.68	3.18
	0.033	5	1.47	2.25	50	0.74	2.09	100	0.70	2.11
10	1	5	2.29	3.11	50	1.90	3.25	100	1.85	3.09
	0.5	5	2.15	3.06	50	1.63	3.13	100	1.60	3.09
	0.033	5	1.47	2.20	50	0.74	2.11	100	0.65	2.26
50	1	5	2.14	2.89	50	1.70	2.93	100	1.77	3.00
	0.5	5	2.00	2.78	50	1.56	2.91	100	1.50	2.97
	0.033	5	1.33	2.07	50	0.93	2.82	100	0.64	2.21

Hysteresis curves for multiple cycle loading at 3mN and 5 cycles were plotted in Fig. 4.32; other similar curves based on Table 4.10 data are shown in Appendix E. As the frequency decreased, the loading curve progressed to a smoother curve. This specific pattern was similarly mentioned in the PDMS multiple cycle hysteresis graphs and was characterized by the viscoelastic deformation in the polymer.

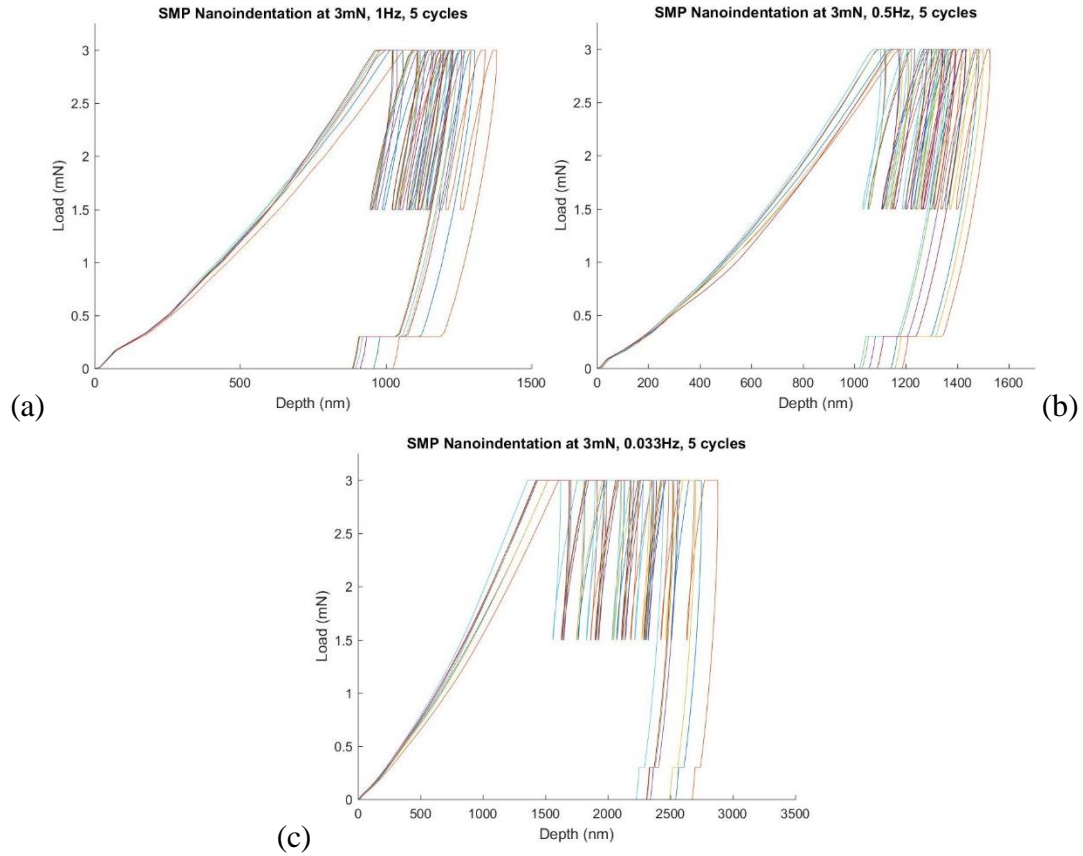


Figure 4.32: SMP multiple cycle nanoindentation at 3mN and 5 cycles with varying frequencies of (a) 1Hz (7 curves), (b) 0.5Hz (7 curves), (c) 0.033Hz (7 curves).

The indentation moduli corresponding to 3mN load tests in Table 4.10 at each cycle and frequency were plotted in Fig. 4.33 and 4.34, respectively. The surface roughness of the SMP was more significant compared to PDMS due to the SMP's hydrophilic characteristics. Again, indentation moduli continued to decrease as maximum depth increased because of energy loss associated with friction and loss modulus. This was also analogous to the hardness trends at 3mN loads in Fig. 4.35 and 4.36. The indentation moduli maxima and minima from Table 4.10 for 3, 10, and 50mN were extracted from Fig. 4.33 through 4.44. The patterns for each of these graphs were comparable to those from PDMS, except mechanical properties for the SMP were

measured at greater magnitudes and lower depths. Tests of 5 cycles typically had a linear trend for PDMS, whereas it was not visible in the SMP tests (Fig. 4.33(a), 4.35(a), 4.37(a), 4.39(a), 4.41(a), and 4.43(a)). The 50 and 100 cycle tests exhibited power law curves, similarly to the PDMS tests. All frequency consistent graphs (Fig. 4.34, 4.36, 4.38, 3.40, 3.42, and 3.44) portrayed power law or even exponential decay trends, as opposed to the PDMS where the only graphs with power law trends were 0.033Hz tests. For PDMS curves, the 1 and 0.5Hz graphs generally exhibited linearity in data points. These differences in trends outline differences in both polymers, even though there were similarities in viscoelastic behavior.

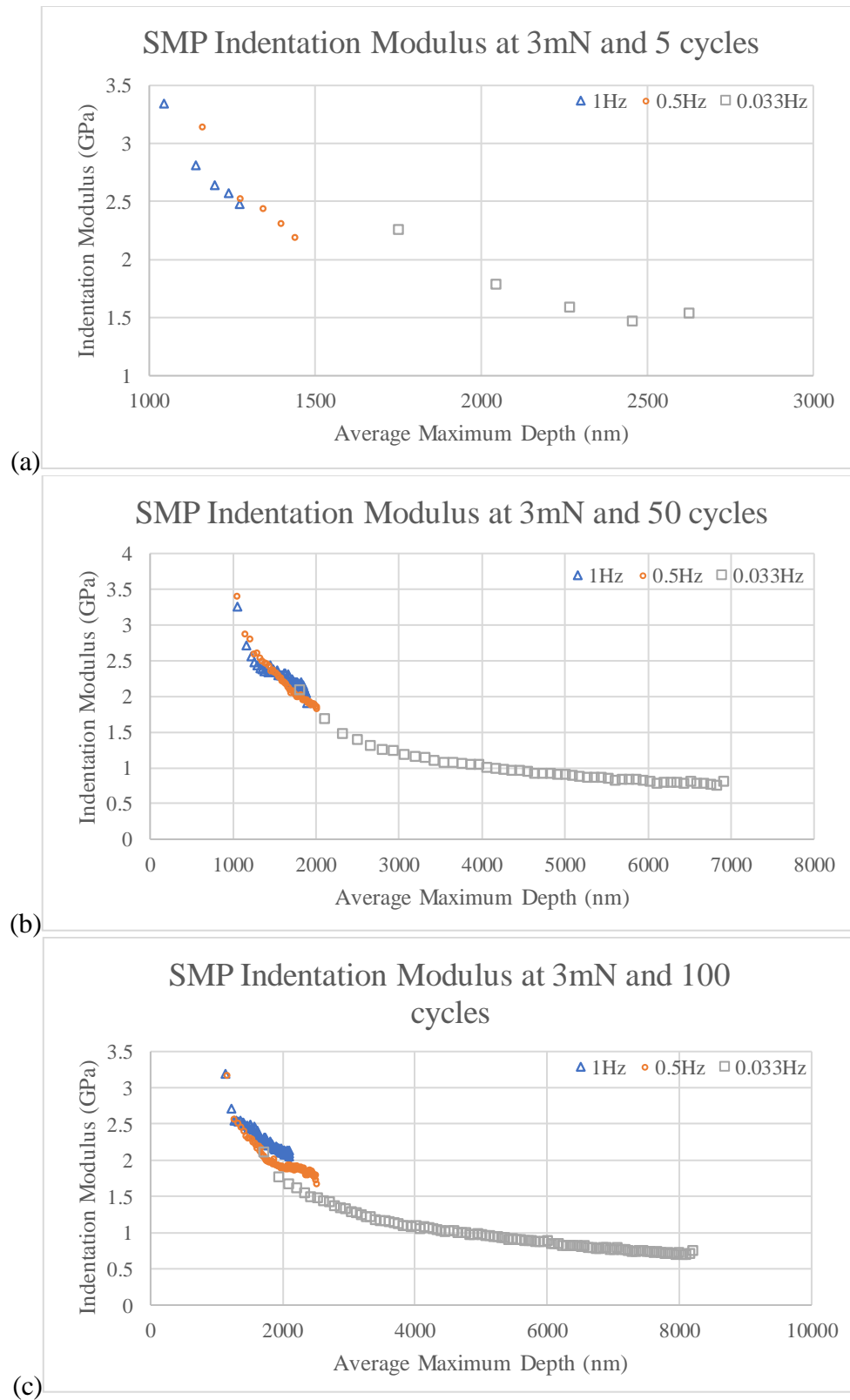


Figure 4.33: SMP indentation modulus graphs at 3mN with various frequencies at (a) 5 cycles, (b) 50 cycles, and (c) 100 cycles.

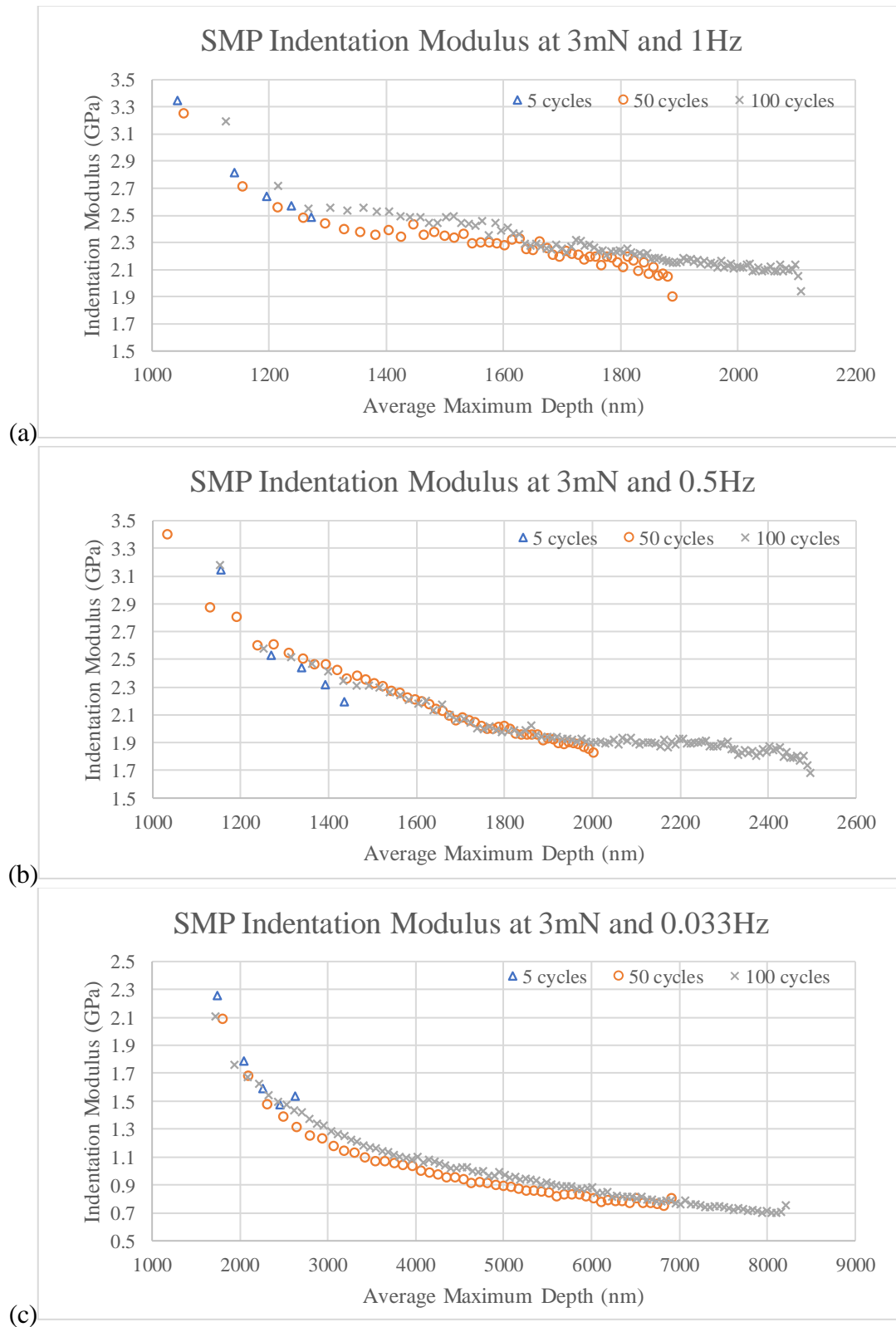


Figure 4.34: SMP indentation modulus graphs at 3mN with various cycles at (a) 1Hz, (b) 0.5Hz, and (c) 0.033Hz.

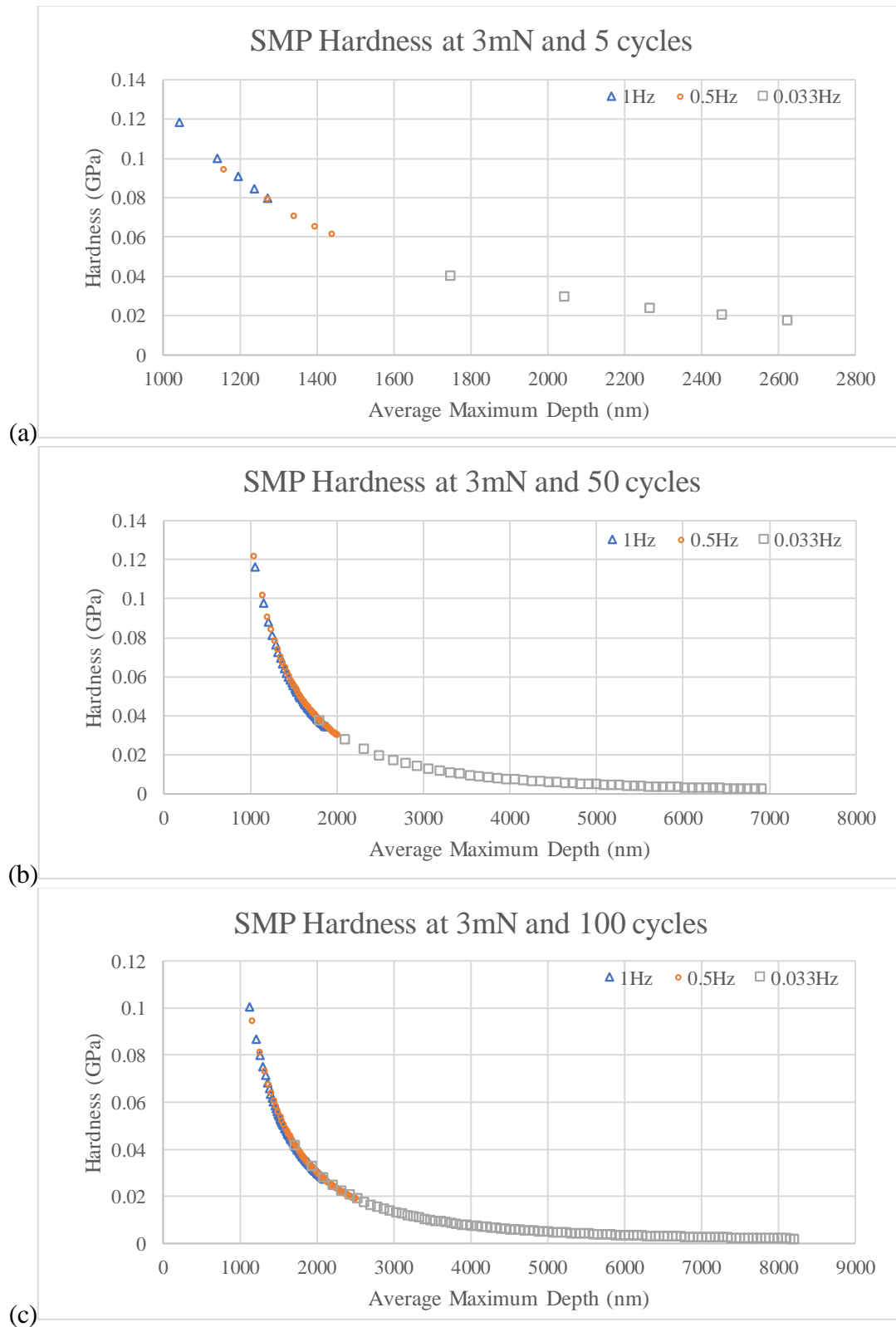


Figure 4.35: SMP hardness graphs at 3mN with various frequencies at (a) 5 cycles, (b) 50 cycles, and (c) 100 cycles.

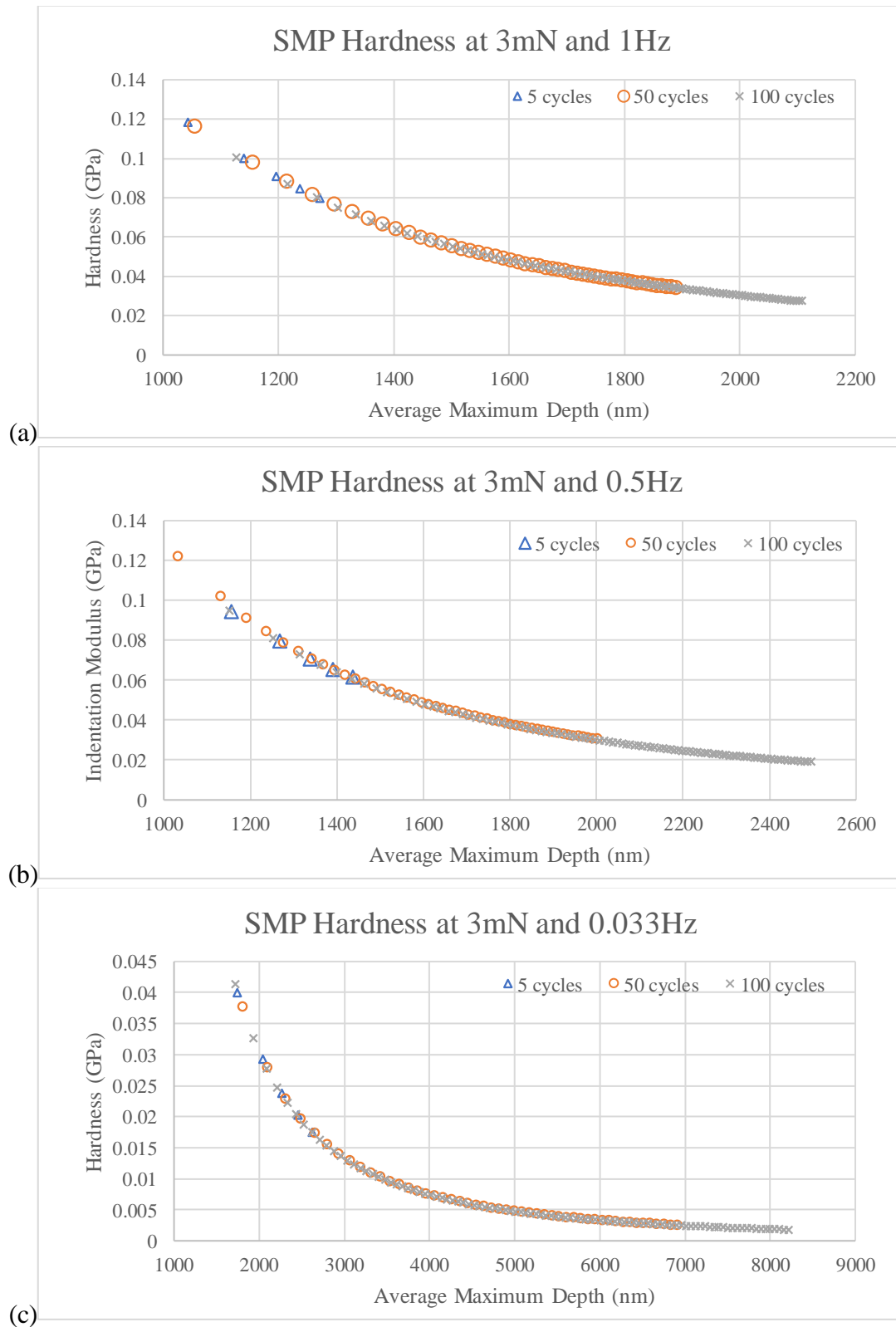


Figure 4.36: SMP hardness graphs at 3mN with various cycles at (a) 1Hz, (b) 0.5Hz, and (c) 0.033Hz.

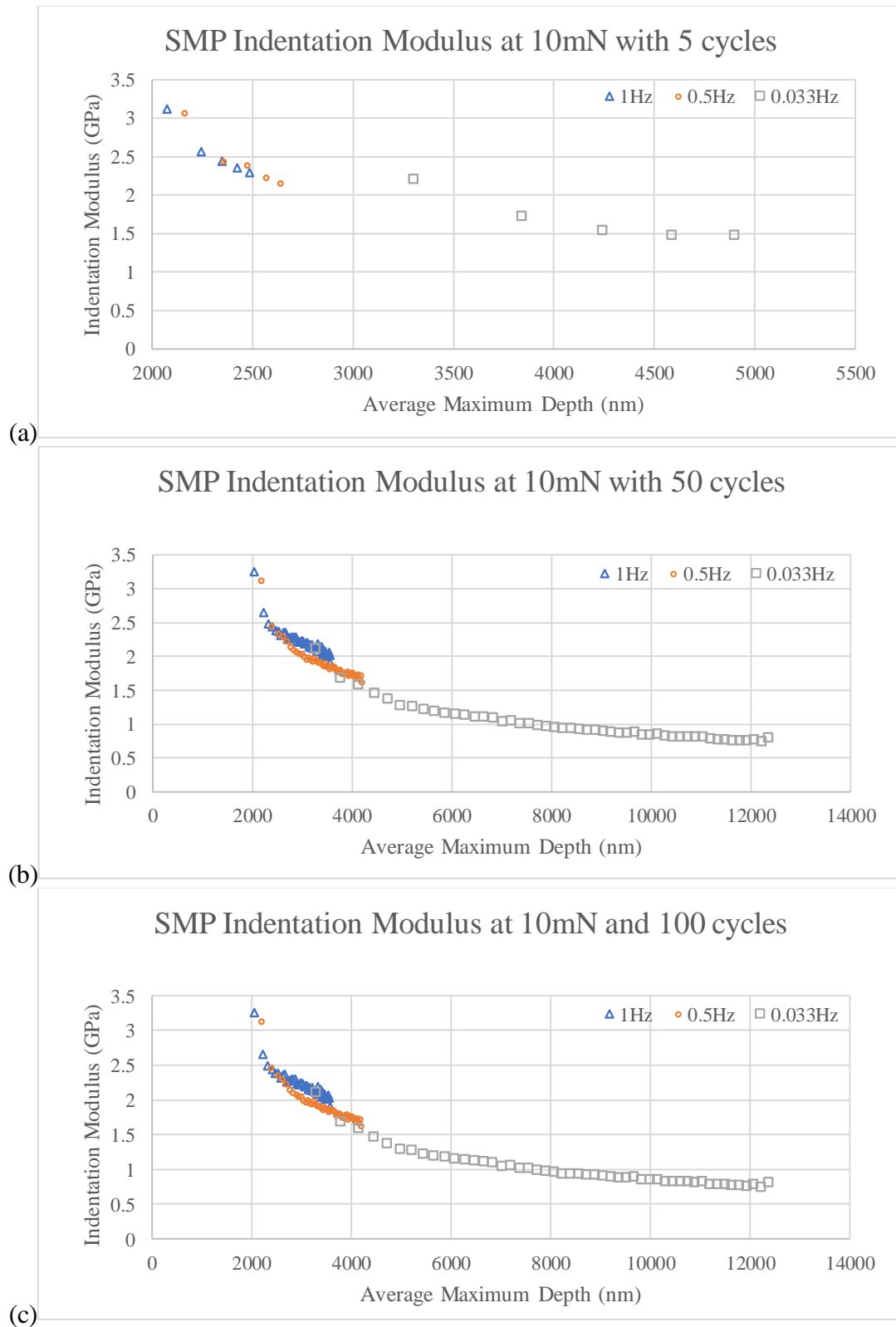


Figure 4.37: SMP indentation modulus graphs at 10mN with various frequencies at (a) 5 cycles, (b) 50 cycles, and (c) 100 cycles.

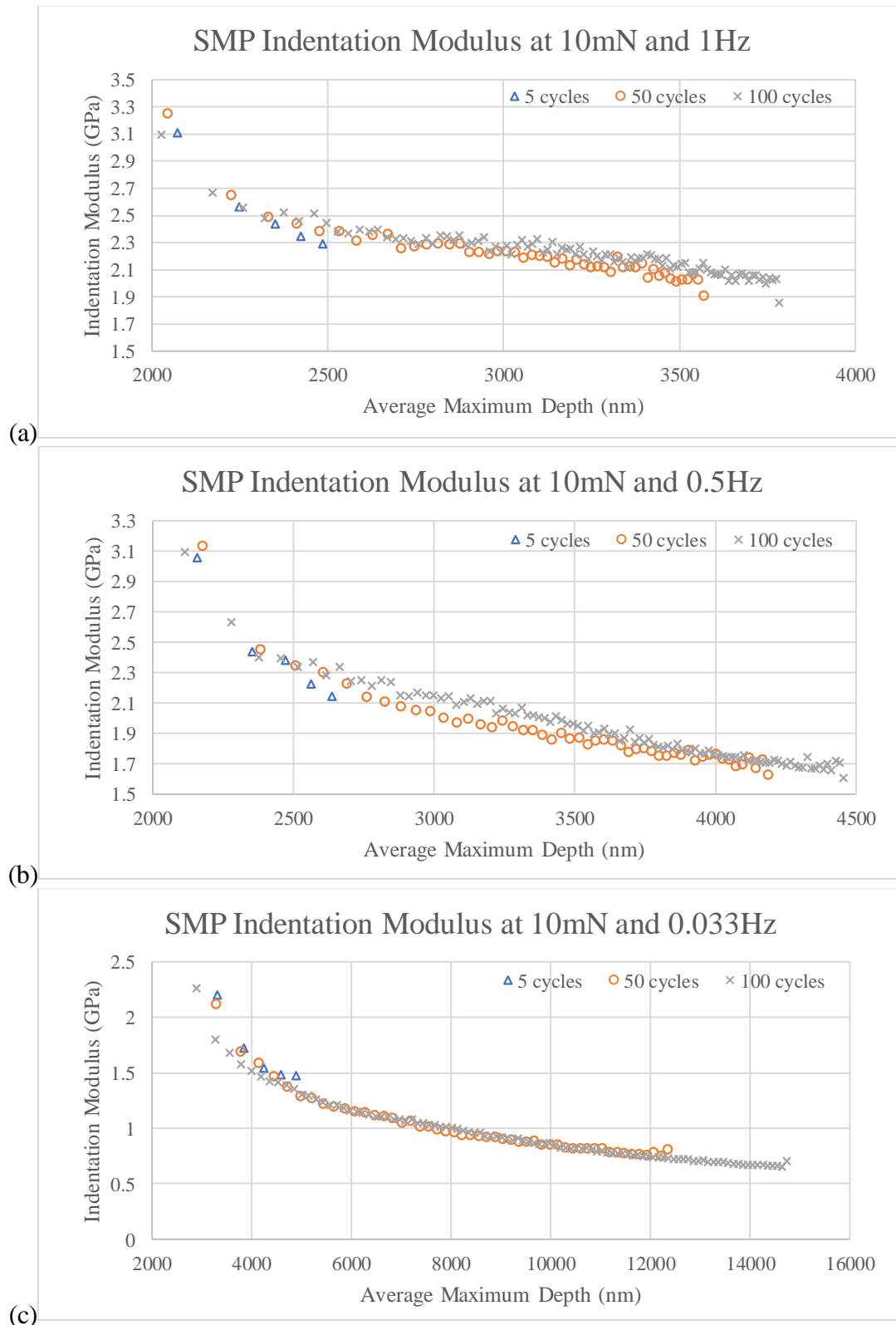


Figure 4.38: SMP indentation modulus graphs at 10mN with various cycles at (a) 1Hz, (b) 0.5Hz, and (c) 0.033Hz.

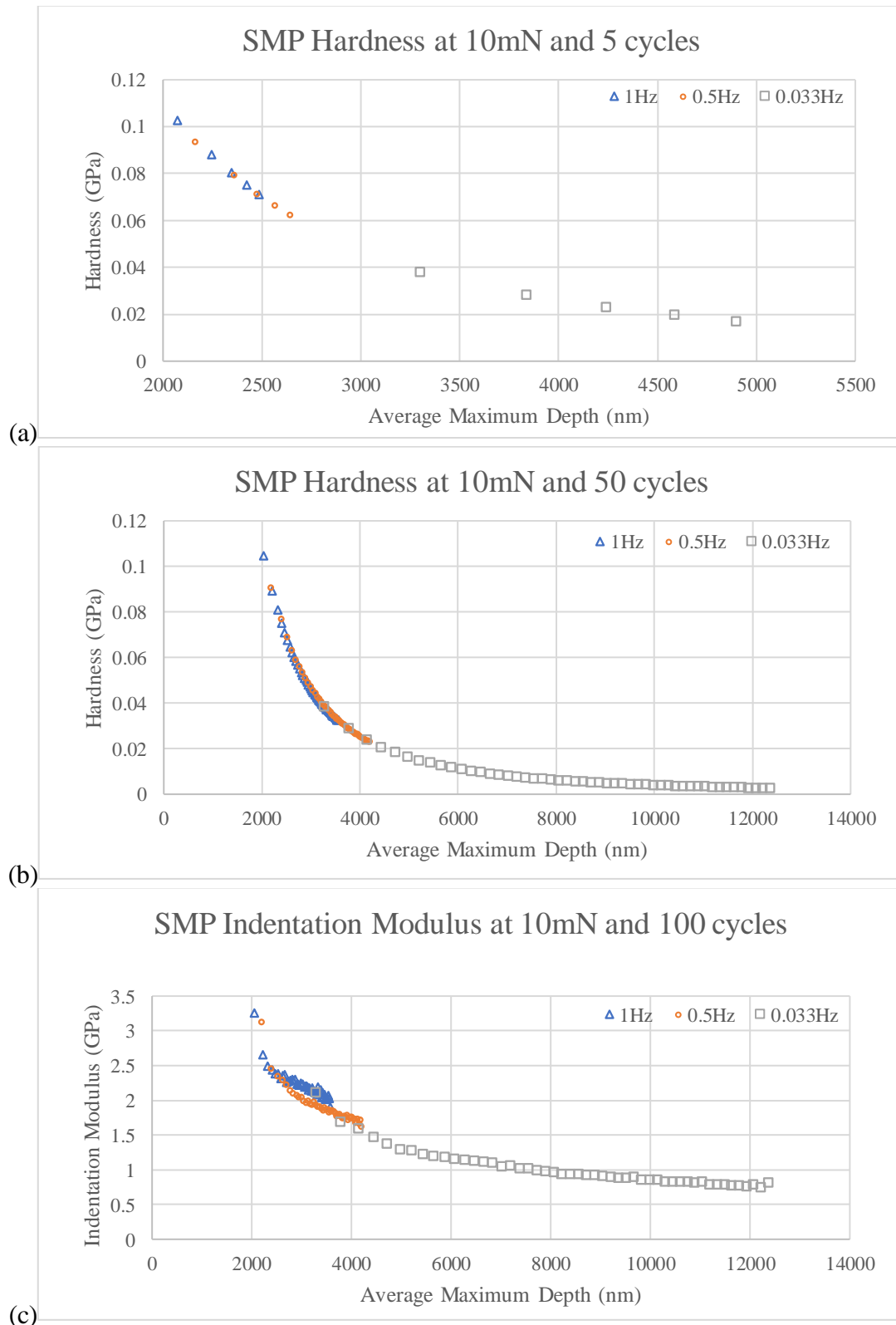


Figure 4.39: SMP hardness graphs at 10mN with various frequencies at (a) 5 cycles, (b) 50 cycles, and (c) 100 cycles.

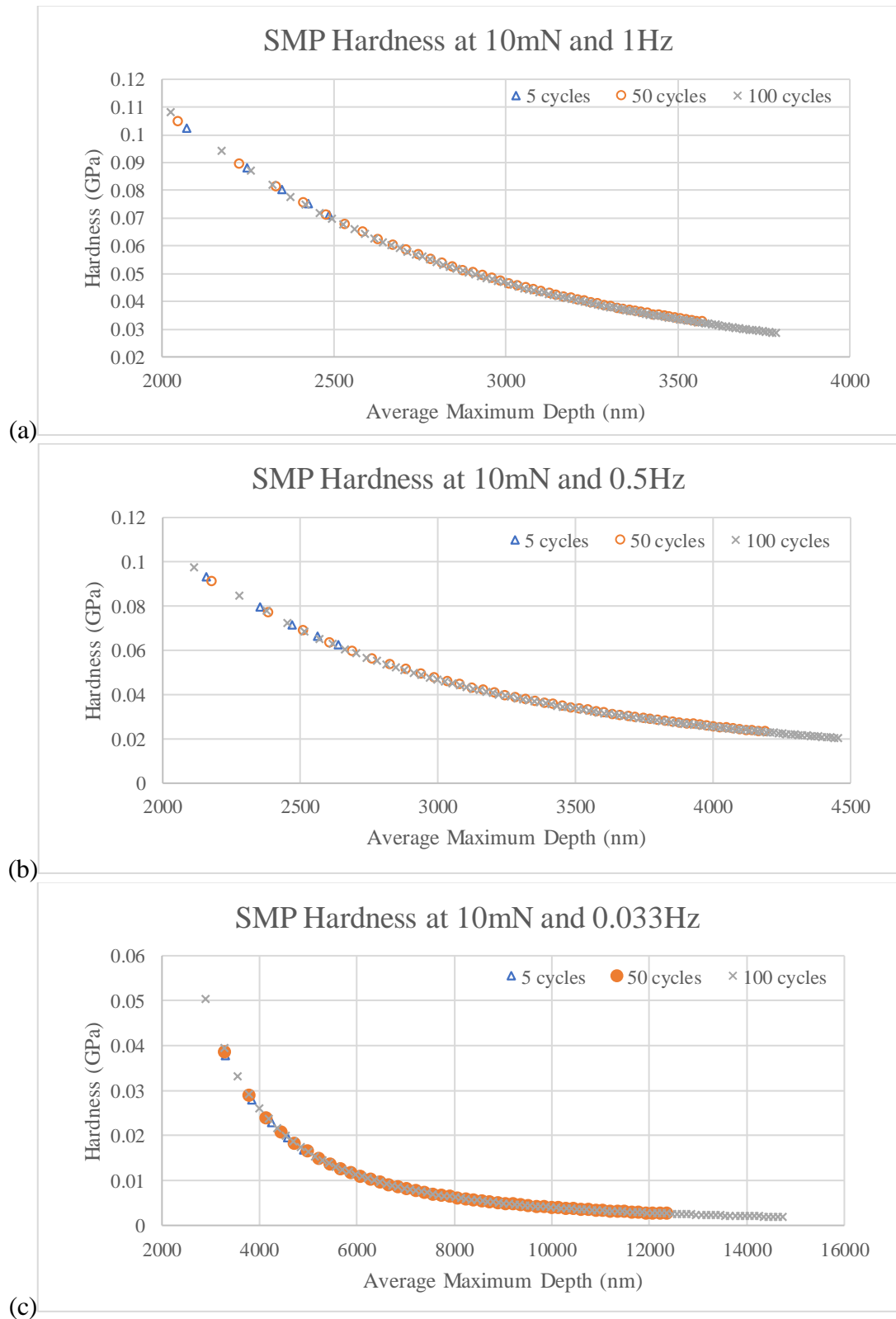


Figure 4.40: SMP hardness graphs at 10mN with various cycles at (a) 1Hz, (b) 0.5Hz, and (c) 0.033Hz.

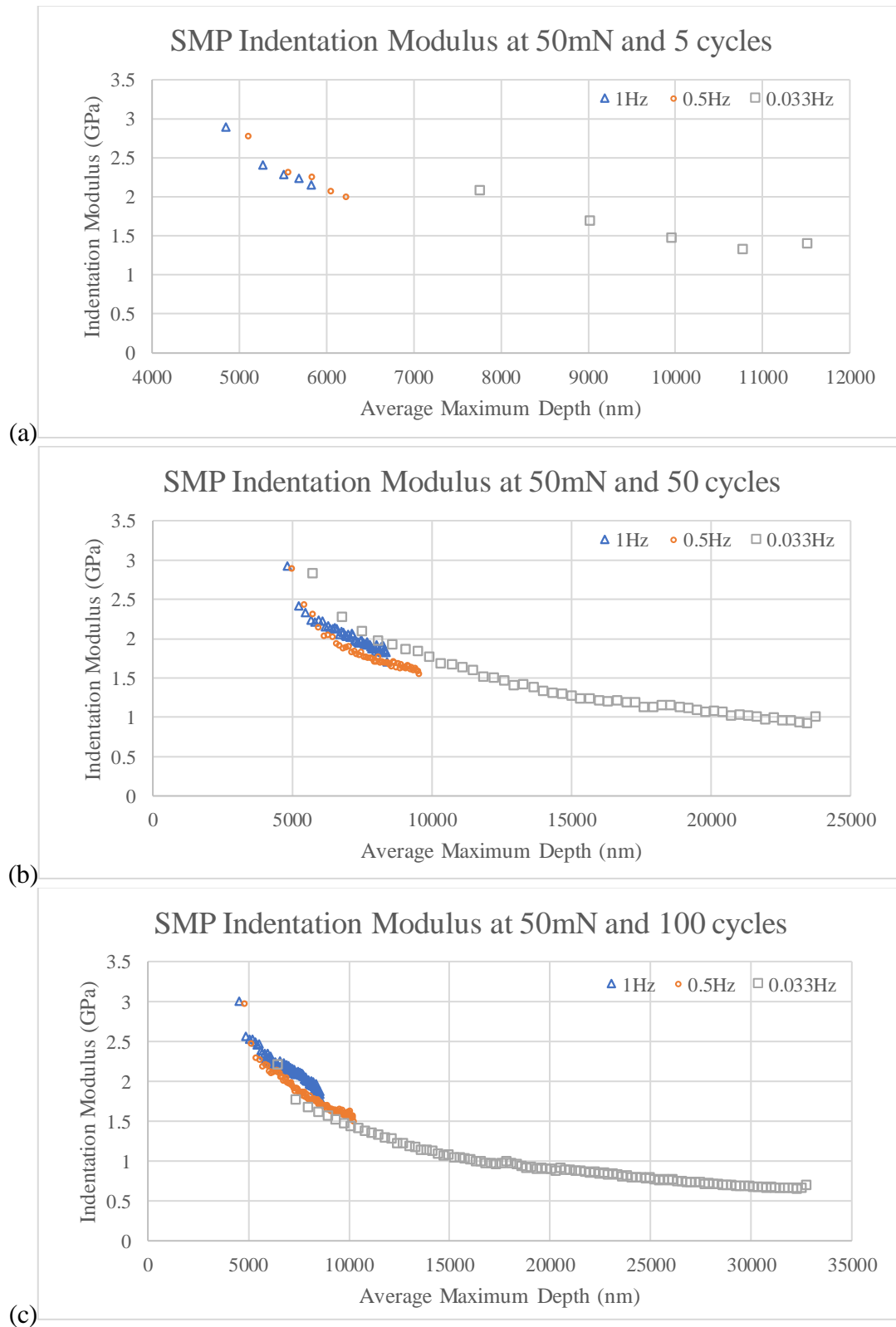


Figure 4.41: SMP indentation modulus graphs at 50mN with various frequencies at (a) 5 cycles, (b) 50 cycles, and (c) 100 cycles.

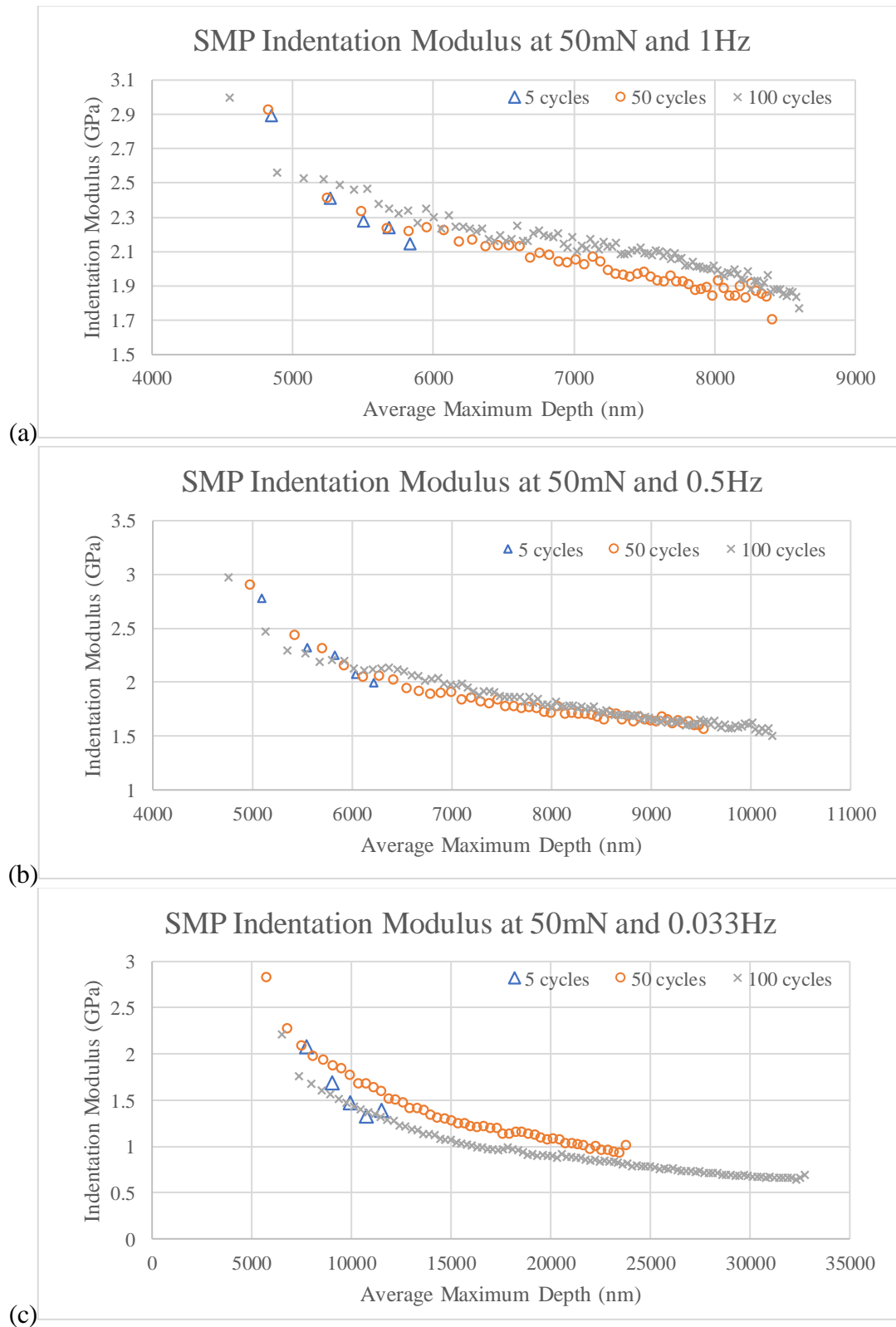


Figure 4.42: SMP indentation modulus graphs at 50mN with various cycles at (a) 1Hz, (b) 0.5Hz, and (c) 0.033Hz.

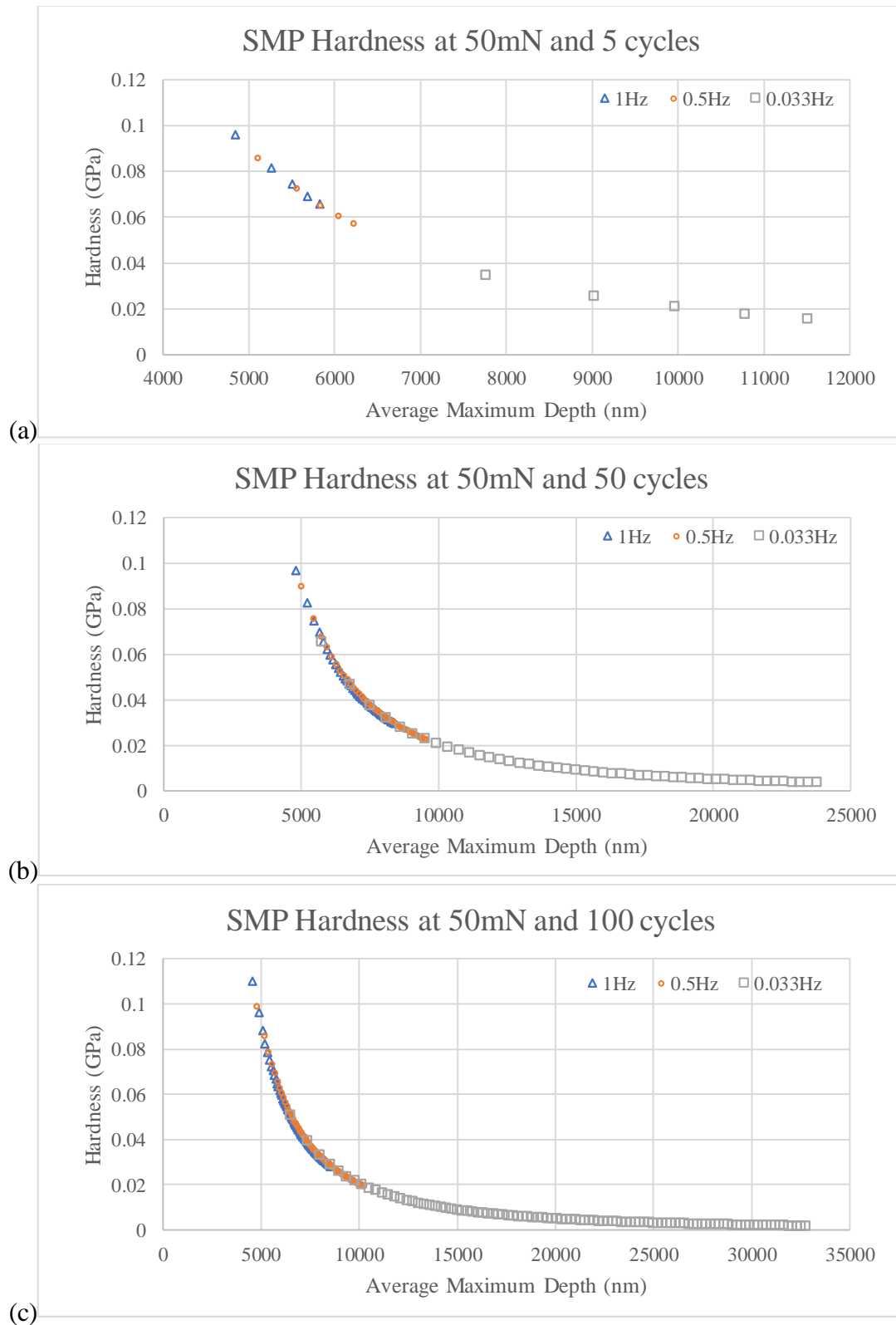


Figure 4.43: SMP hardness graphs at 50mN with various frequencies at (a) 5 cycles, (b) 50 cycles, and (c) 100 cycles.



Figure 4.44: SMP hardness graphs at 50mN with various frequencies at (a) 1Hz, (b) 0.5Hz, and (c) 0.033Hz.

Chapter 5 – CONCLUSION

Nanoindentation is a widely accepted method of measuring mechanical properties of materials. The indentation moduli calculated from the modified curved area function (mCAF) for all three types of Kevlar are larger than ones derived from the flat area function (FAF). The data corroborates that the contact area between the fiber and the indenter is smaller for the mCAF, illustrating the requirement of an area correction function. The significance in contact area for a round surface arises from comparable magnitudes between the Berkovich indenter tip and fiber diameter.

The mechanical properties of these Kevlar fibers derived from the corrected area function accurately describe their physical material properties. At 10% of fiber diameter, KM2 exhibits the largest indentation modulus of 5.10 GPa ($\nu=0.30$), while K119 possesses the lowest indentation modulus of 2.43 GPa ($\nu=0.27$). The indentation moduli for each fiber varies along the fiber diameter and does not consist of a universal indentation modulus. Indentations on the skins of the K29 and K119 fibers indicate stronger chemical composition as opposed to their cores. The mCAF results are the most comparable to reported values, even with variations in testing methods. Area correction functions are recommended in future studies for characterization of cylindrical fibers based on their curvature size.

The planar specimens: shape memory polymer (SMP) and polydimethylsiloxane (PDMS), do not require area function corrections. Rather, their unique behavior is studied with implementation of multiple cycle loading for frequency and cyclic dependency. The indentation moduli and hardness for both SMP and PDMS decrease as the depth increases during both single and multiple cycle indentations. The trends in PDMS are

linear for 5 and 50 cycles, whereas 100 cycle tests for mechanical properties favor power law curve fits. Linearity is displayed in PDMS at 1 and 0.5Hz controlled tests, while 0.033Hz tests follow power law curve fits. All three cycles and frequencies exhibit power law trends in SMP specimens. The mechanical properties of PDMS measured in the present study comply with reported literature, further affirming the precisions of indentation results. When the loads are increased for indentation experiments on both materials, the indentation moduli decrease as the maximum depth increases. A similar pattern is also evident for the hardness of both materials. Typically, the depth increases drastically at lower frequencies, indicating creep behavior. The tests from single cycle indentation validate with ones from multiple cycle loading, confirming the accuracy of data yielded from the two processes.

APPENDICES

Appendix A – Kevlar 29 Supplementary Graphs

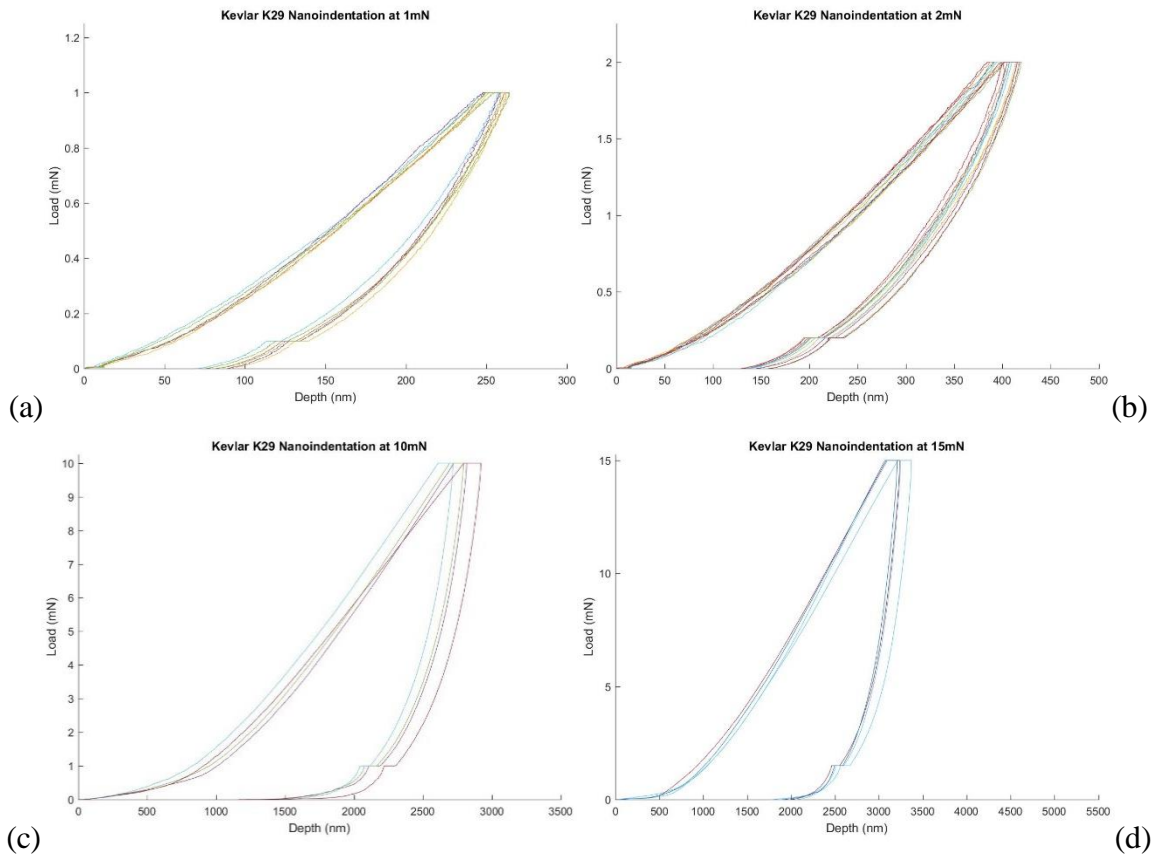
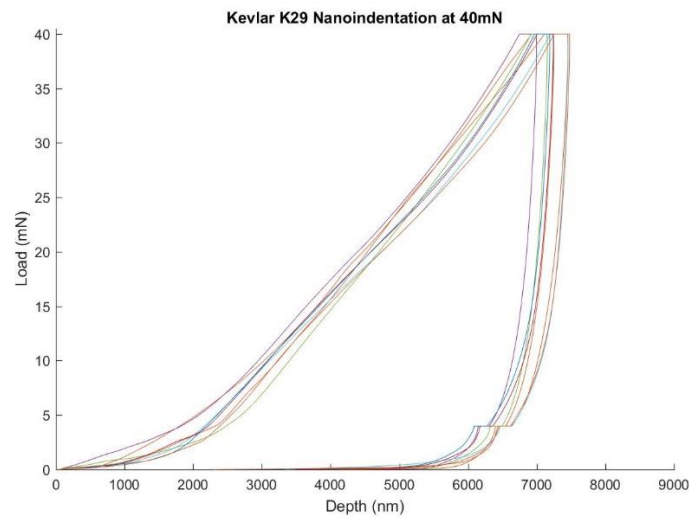
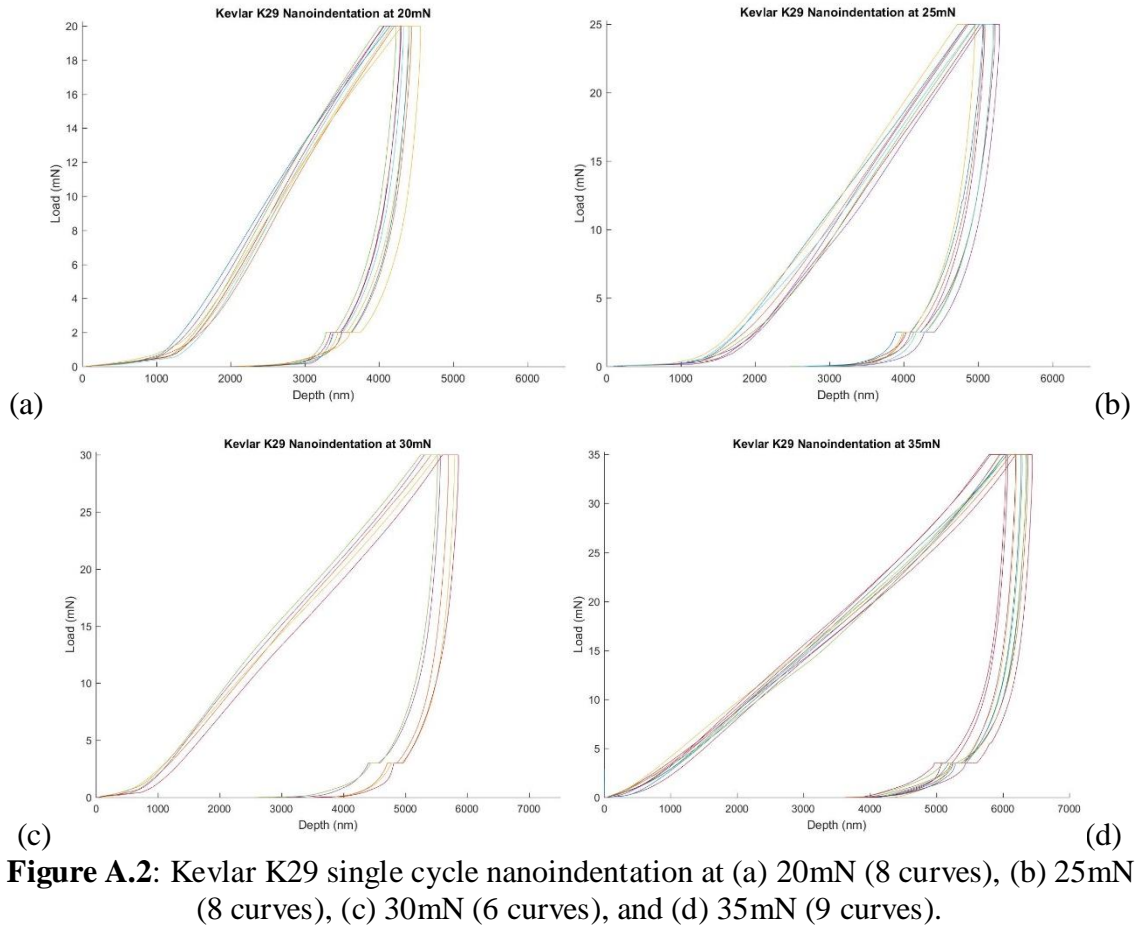


Figure A.1: Kevlar K29 single cycle nanoindentation at (a) 1mN (6 curves), (b) 2mN (11 curves), (c) 10mN (4 curves), and (d) 15mN (4 curves).



Appendix B – Kevlar KM2 Supplementary Graphs

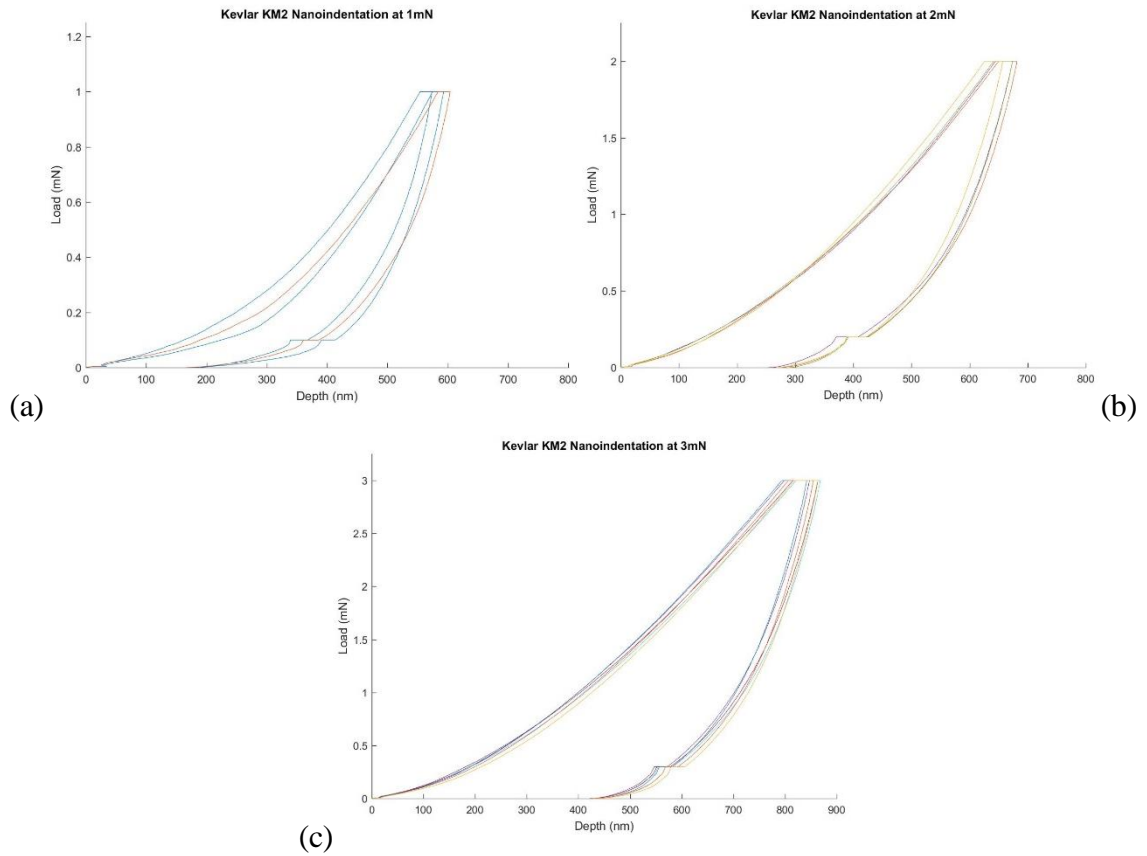


Figure B.1: Kevlar KM2 single cycle nanoindentation at (a) 1mN (3 curves), (b) 2mN (4 curves), and (c) 3mN (6 curves).

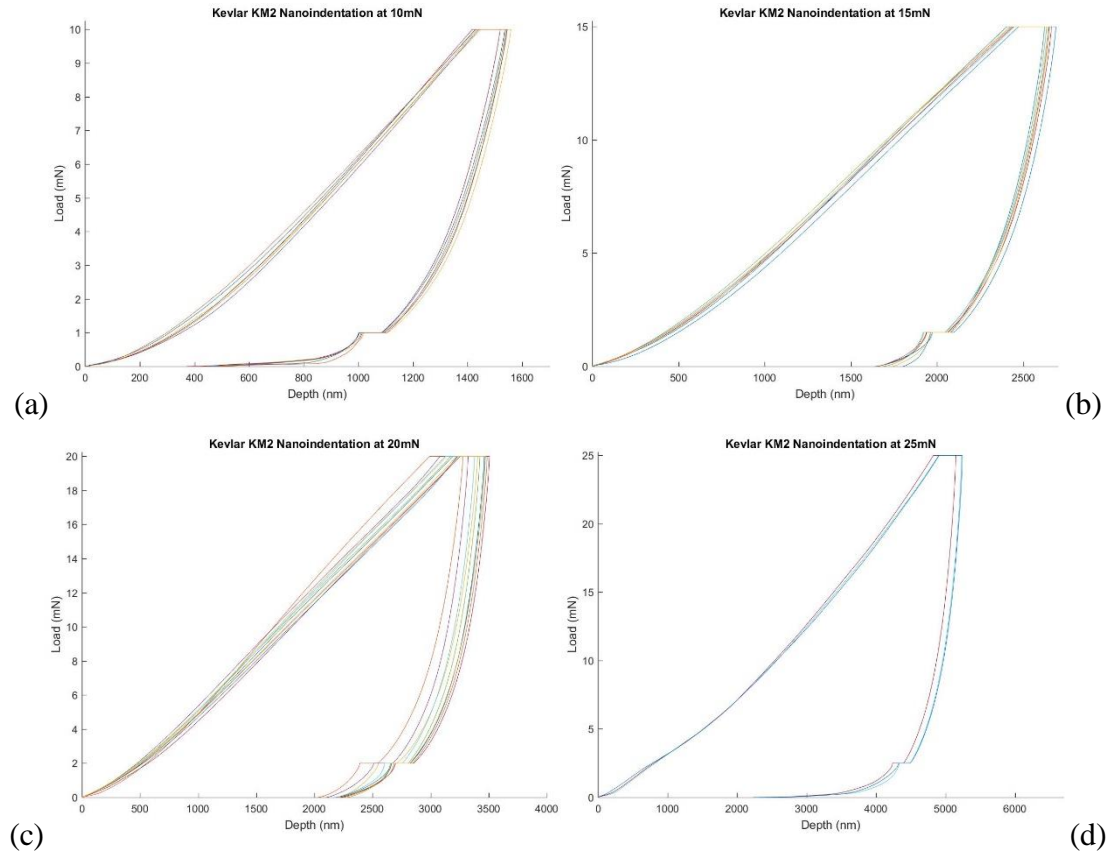


Figure B.2: Kevlar KM2 single cycle nanoindentation at (a) 10mN (6 curves), (b) 15mN (7 curves), (c) 20mN (10 curves), (d) 25mN (3 curves).

Appendix C – Kevlar K119 Supplementary Graphs

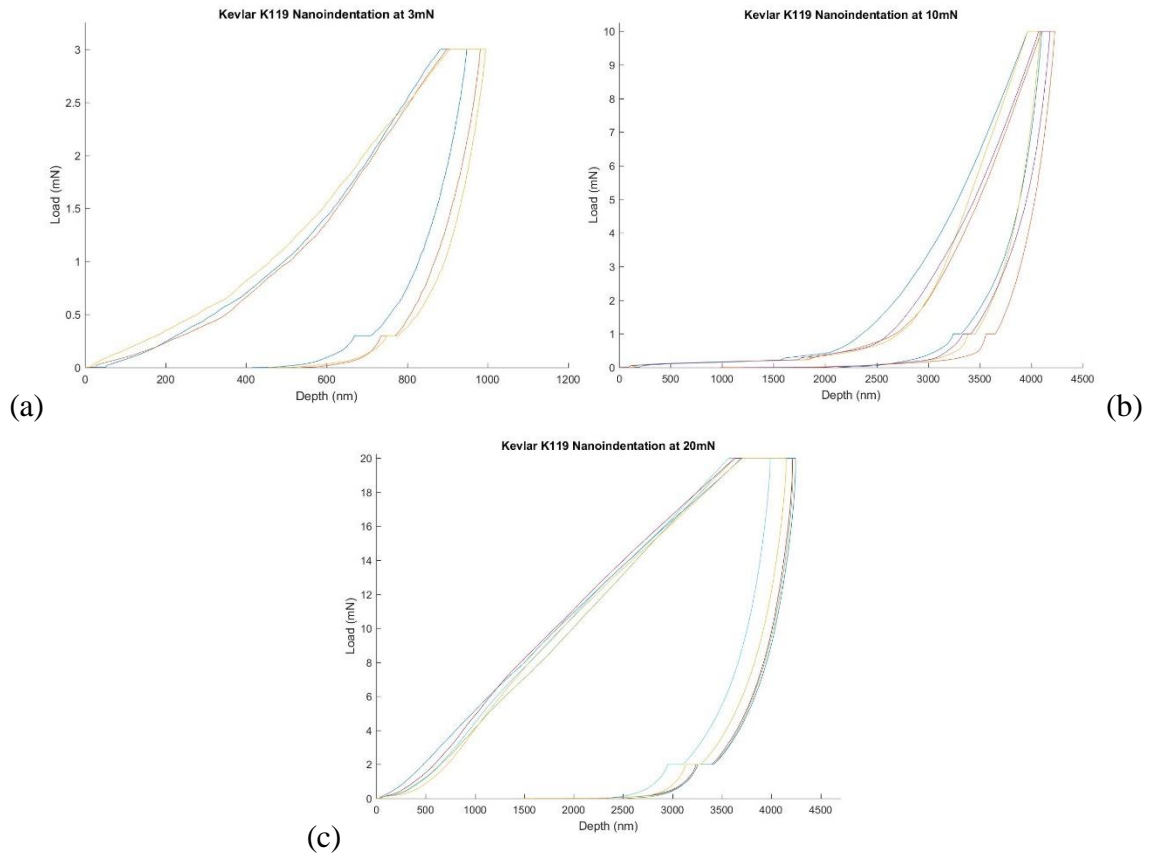


Figure C.1: Kevlar K119 single cycle nanoindentation at (a) 3mN (3 curves), (b) 10mN (4 curves), and (c) 20mN (5 curves).

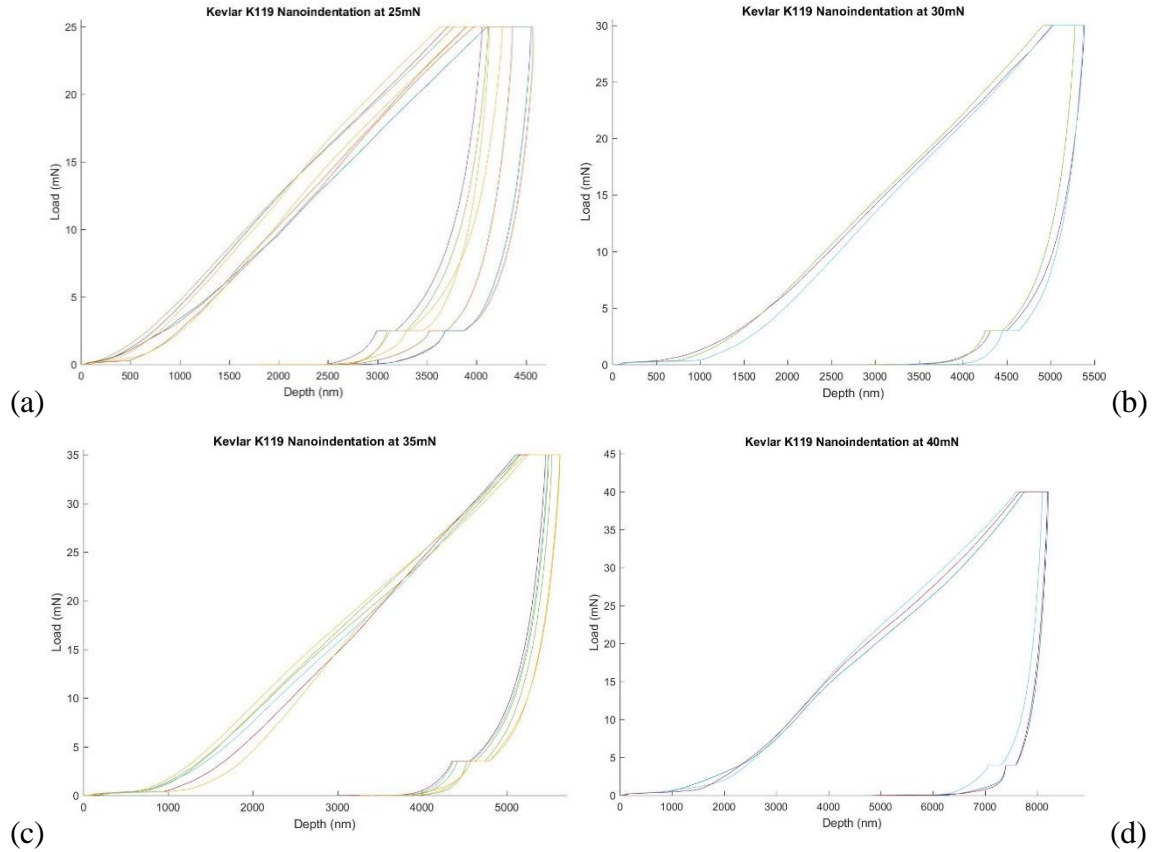


Figure C.2: Kevlar K119 single cycle nanoindentation at (a) 25mN (7 curves), (b) 30mN (3 curves), (c) 35mN (6 curves), and (d) 40mN (3 curves).

Appendix D – PDMS Supplementary Graphs

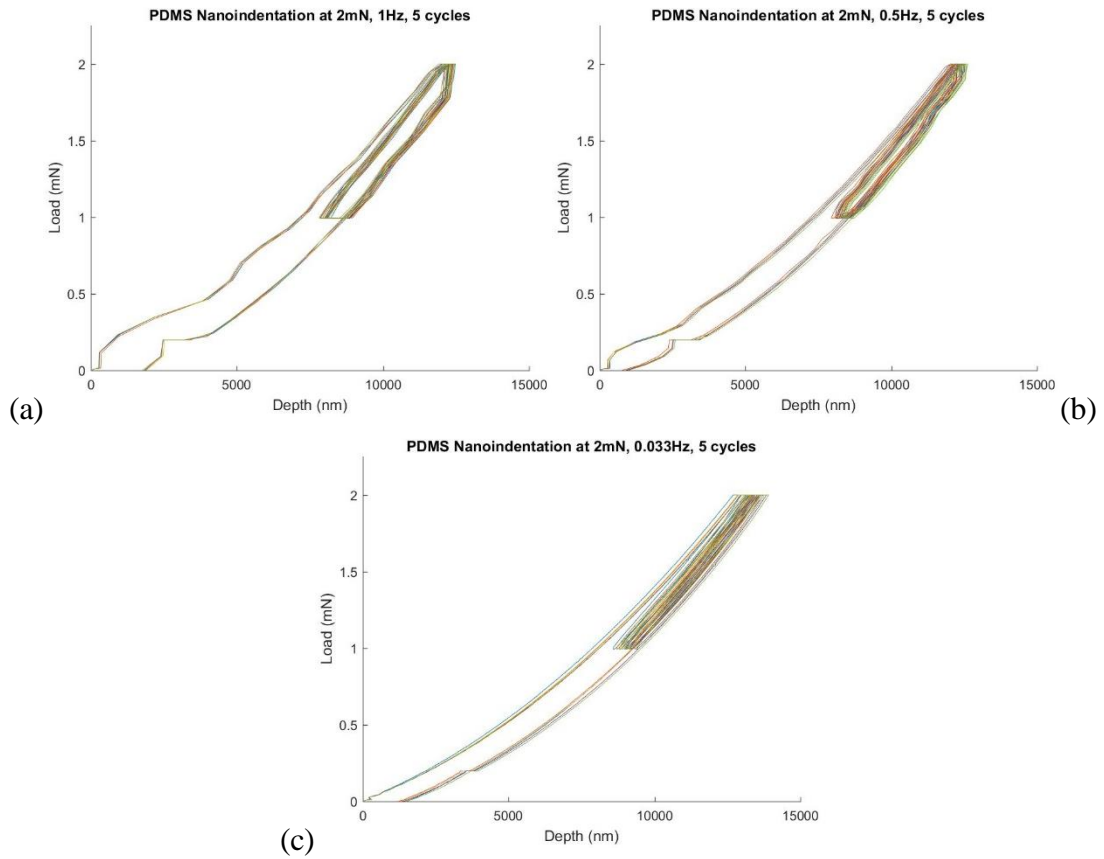


Figure D.1: PDMS multiple cycle nanoindentation at 2mN and 5 cycles with varying frequencies of (a) 1Hz (5 curves), (b) 0.5Hz (5 curves), (c) 0.033Hz (5 curves).

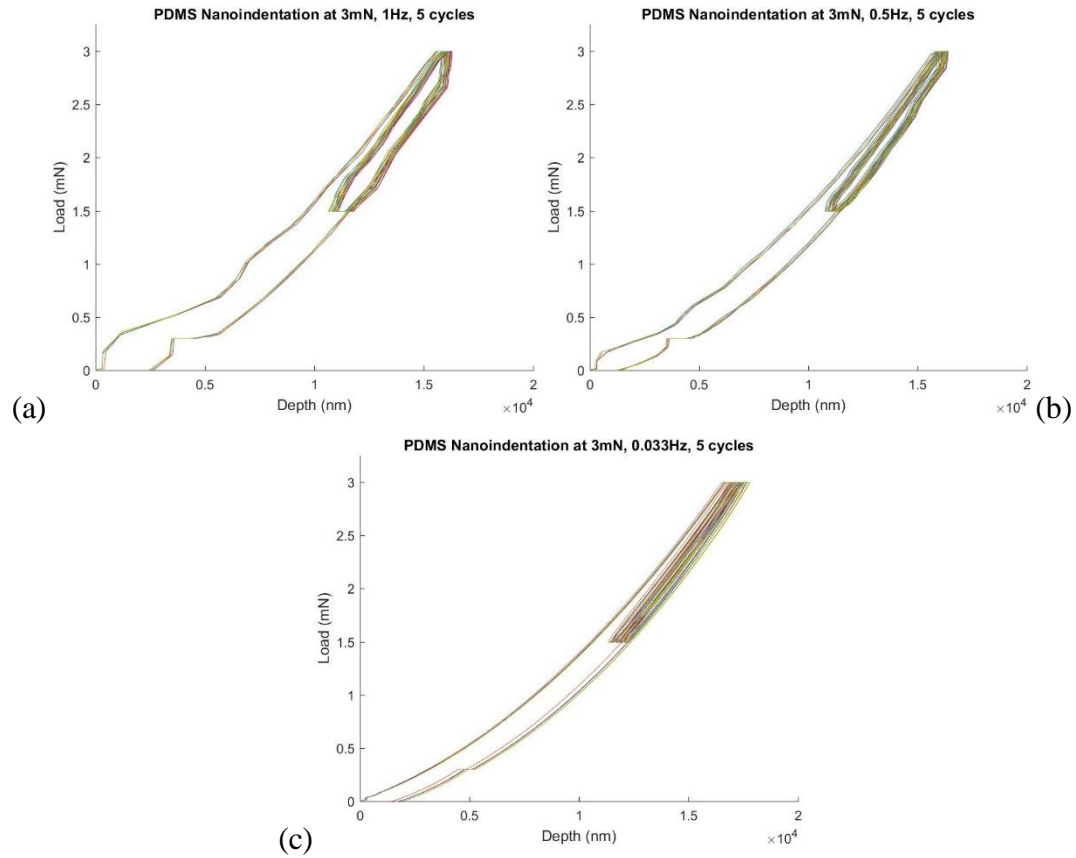


Figure D.2: PDMS multiple cycle nanoindentation at 3mN and 5 cycles with varying frequencies of (a) 1Hz (5 curves), (b) 0.5Hz (5 curves), (c) 0.033Hz (5 curves).

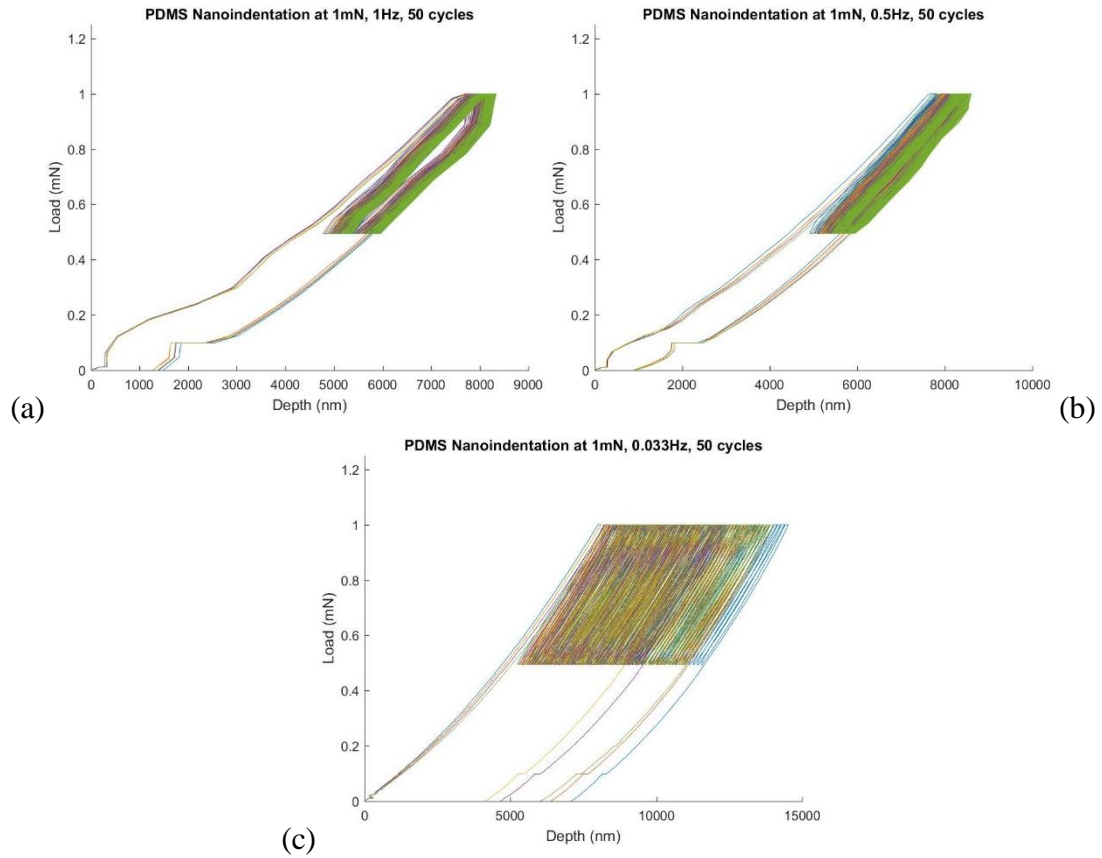


Figure D.3: PDMS multiple cycle nanoindentation at 1 mN and 50 cycles with varying frequencies of (a) 1Hz (5 curves), (b) 0.5Hz (5 curves), (c) 0.033Hz (5 curves).

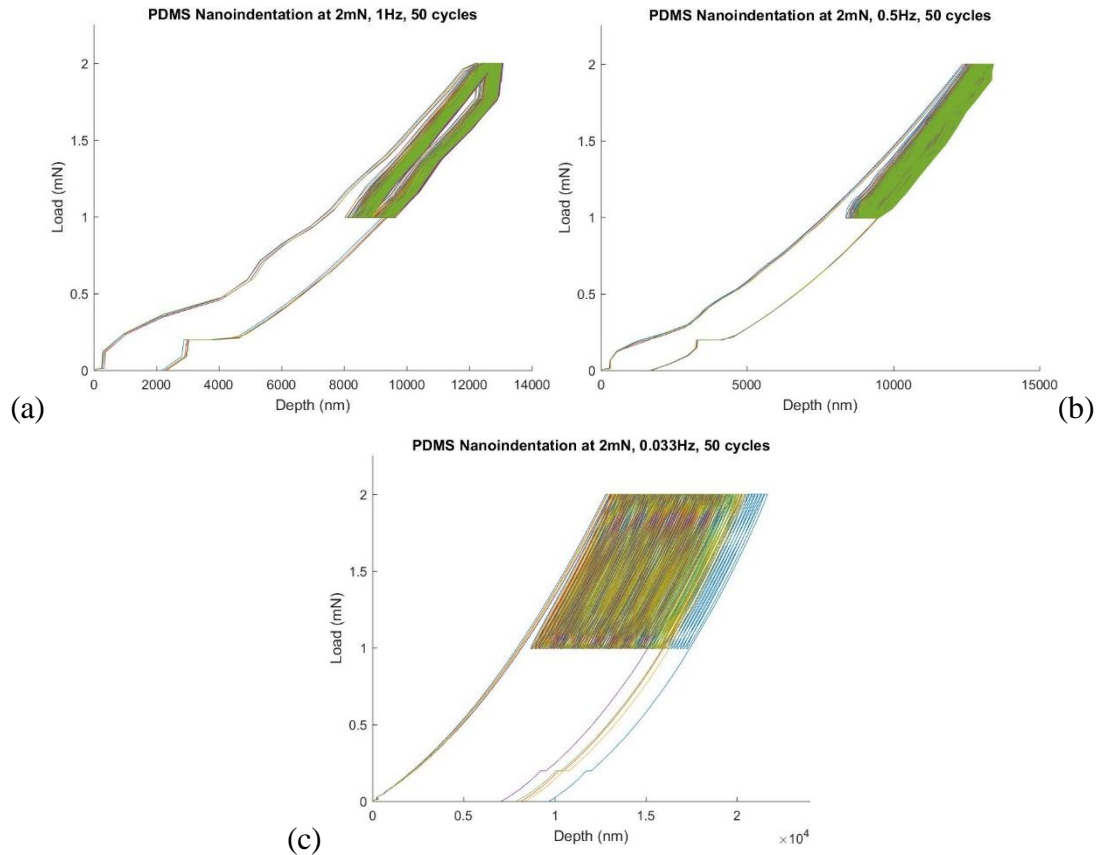


Figure D.4: PDMS multiple cycle nanoindentation at 2mN and 50 cycles with varying frequencies of (a) 1Hz (5 curves), (b) 0.5Hz (5 curves), (c) 0.033Hz (5 curves).

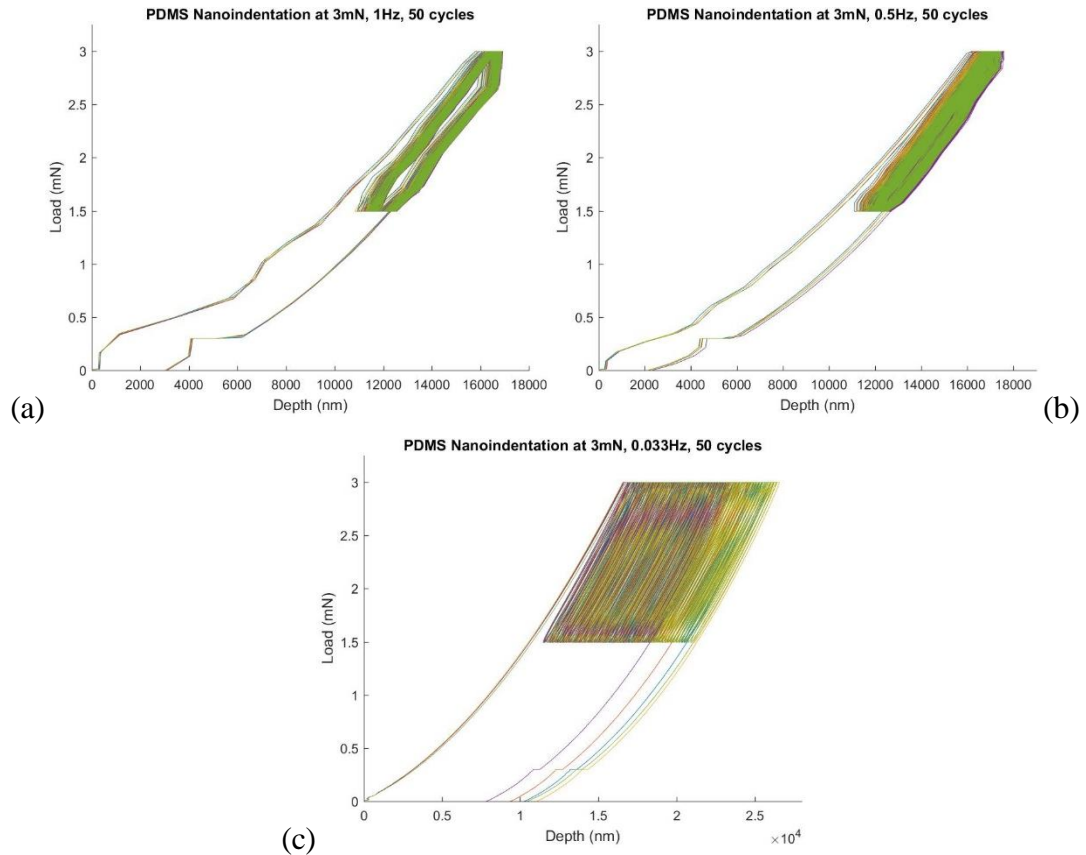


Figure D.5: PDMS multiple cycle nanoindentation at 3mN and 50 cycles with varying frequencies of (a) 1Hz (5 curves), (b) 0.5Hz (5 curves), (c) 0.033Hz (5 curves).

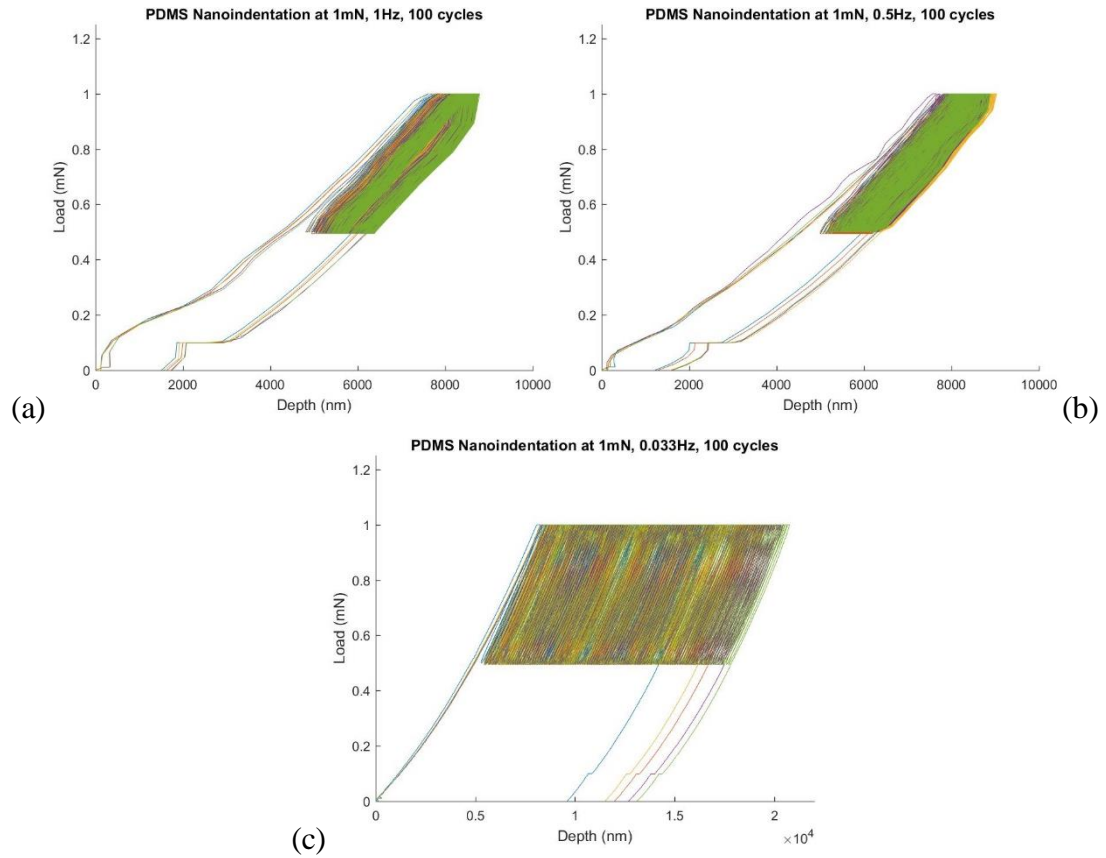


Figure D.6: PDMS multiple cycle nanoindentation at 1mN and 100 cycles with varying frequencies of (a) 1Hz (5 curves), (b) 0.5Hz (5 curves), (c) 0.033Hz (5 curves).

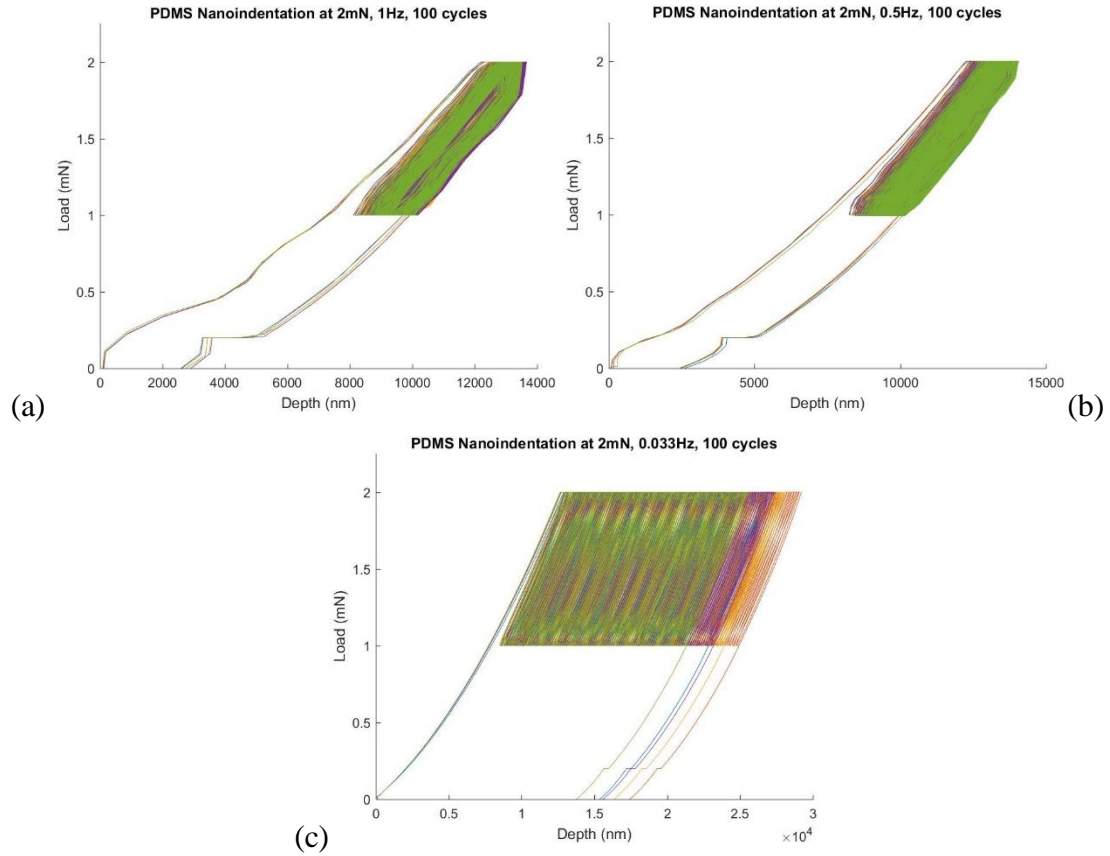


Figure D.7: PDMS multiple cycle nanoindentation at 2mN and 100 cycles with varying frequencies of (a) 1Hz (5 curves), (b) 0.5Hz (5 curves), (c) 0.033Hz (5 curves).

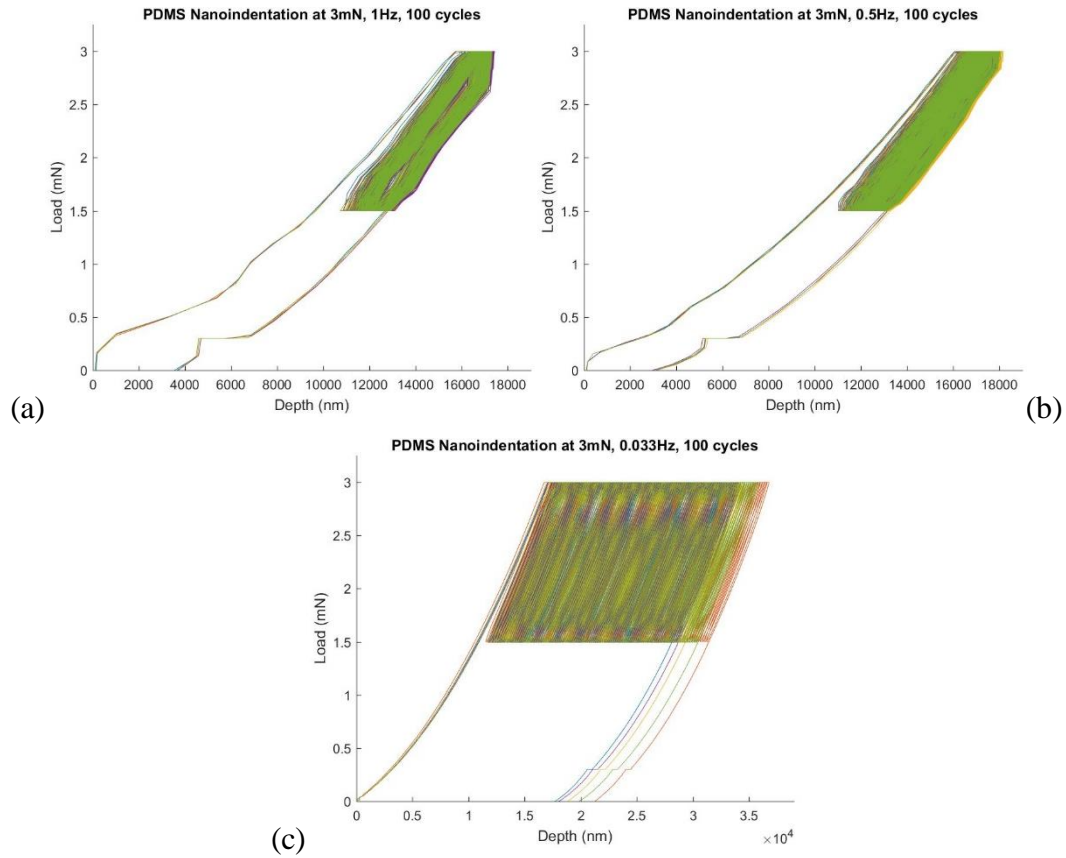


Figure D.8: PDMS multiple cycle nanoindentation at 3mN and 100 cycles with varying frequencies of (a) 1Hz (5 curves), (b) 0.5Hz (5 curves), (c) 0.033Hz (5 curves).

Appendix E – SMP Supplementary Graphs

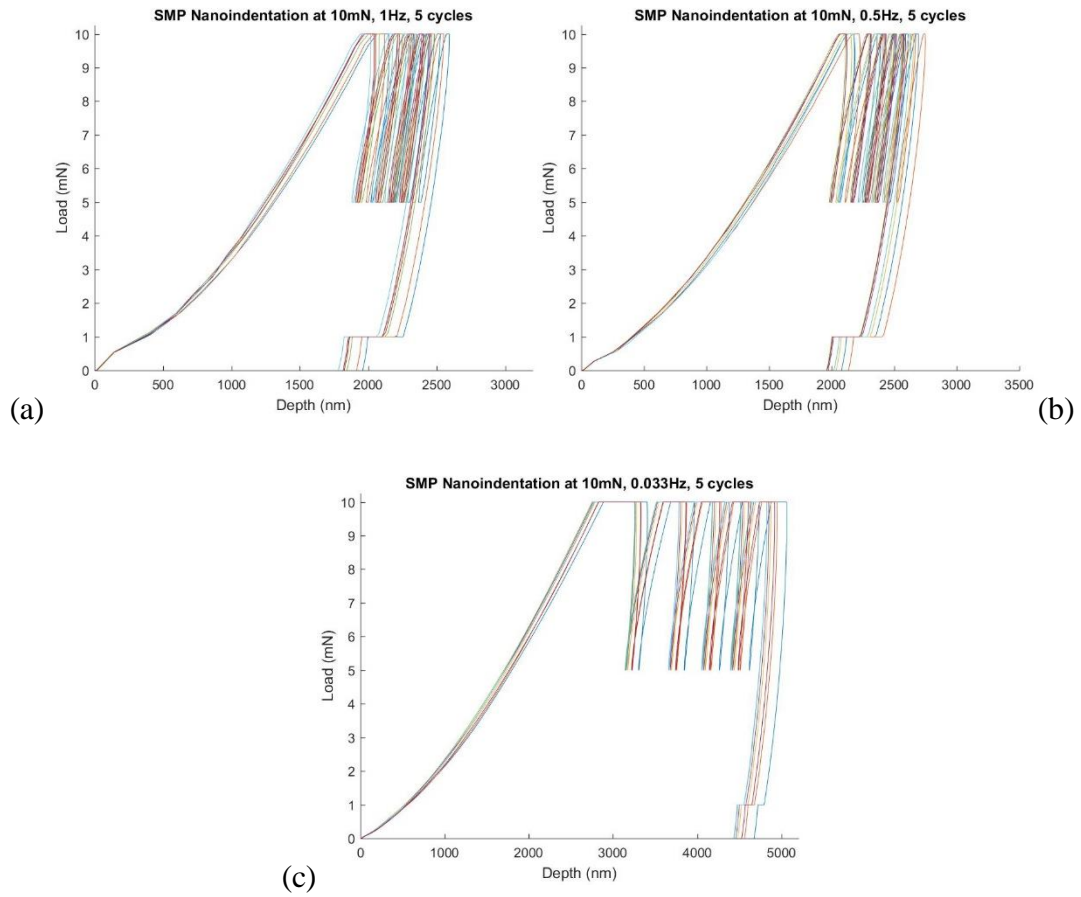


Figure E.1: SMP multiple cycle nanoindentation at 10mN and 5 cycles with varying frequencies of (a) 1Hz (7 curves), (b) 0.5Hz (7 curves), (c) 0.033Hz (7 curves).

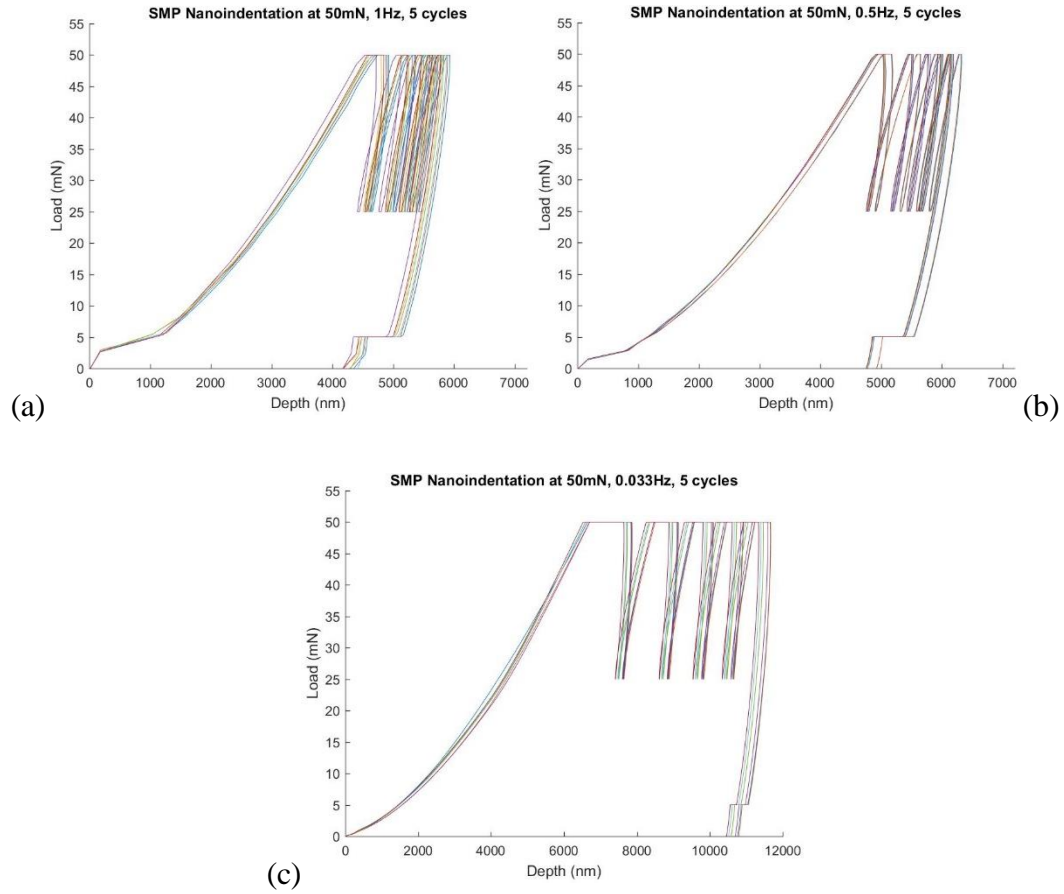


Figure E.2: SMP multiple cycle nanoindentation at 50mN and 5 cycles with varying frequencies of (a) 1Hz (7 curves), (b) 0.5Hz (7 curves), (c) 0.033Hz (7 curves).

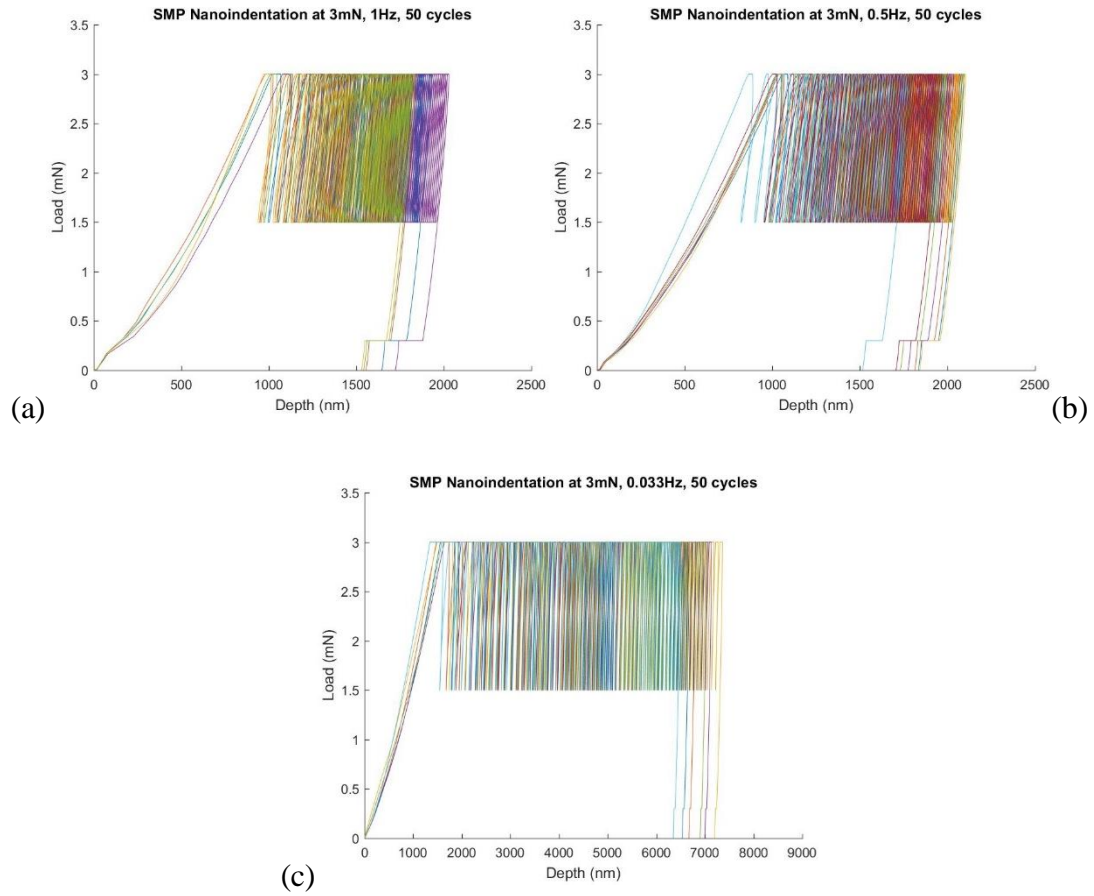


Figure E.3: SMP multiple cycle nanoindentation at 3mN and 50 cycles with varying frequencies of (a) 1Hz (5 curves), (b) 0.5Hz (7 curves), (c) 0.033Hz (6 curves).

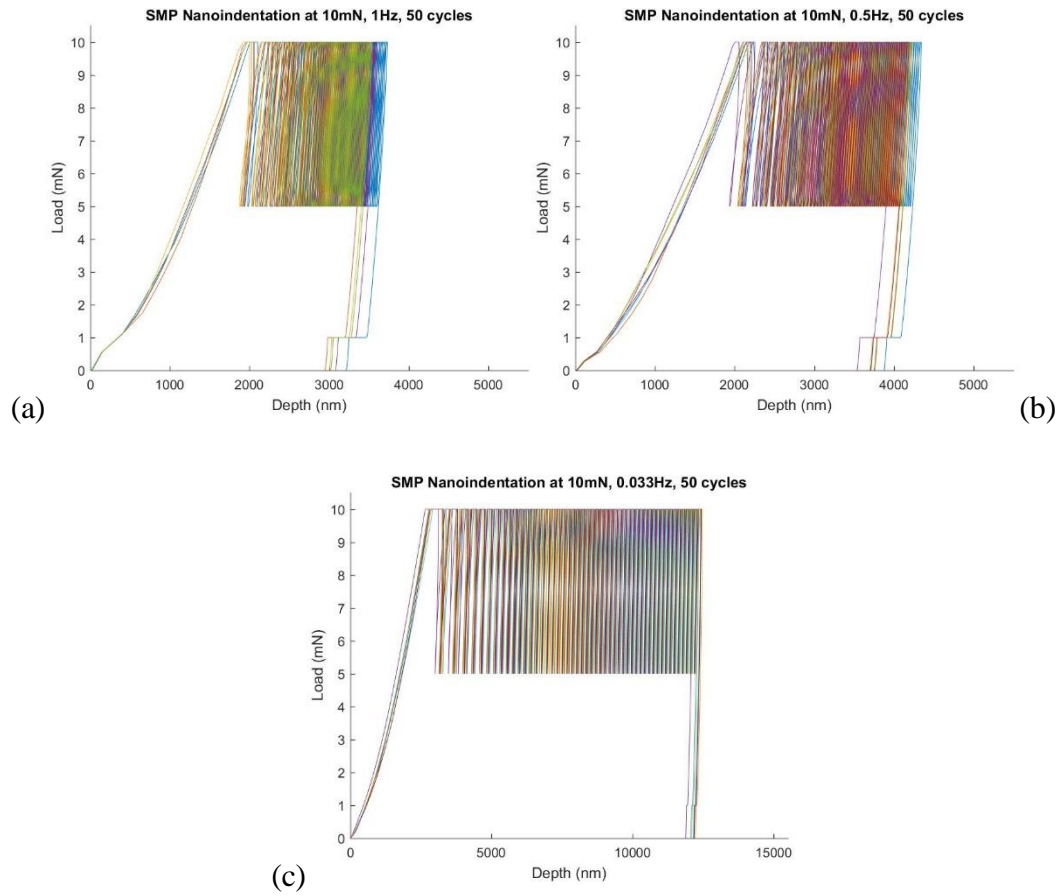


Figure E.4: SMP multiple cycle nanoindentation at 10mN and 50 cycles with varying frequencies of (a) 1Hz (5 curves), (b) 0.5Hz (7 curves), (c) 0.033Hz (7 curves).

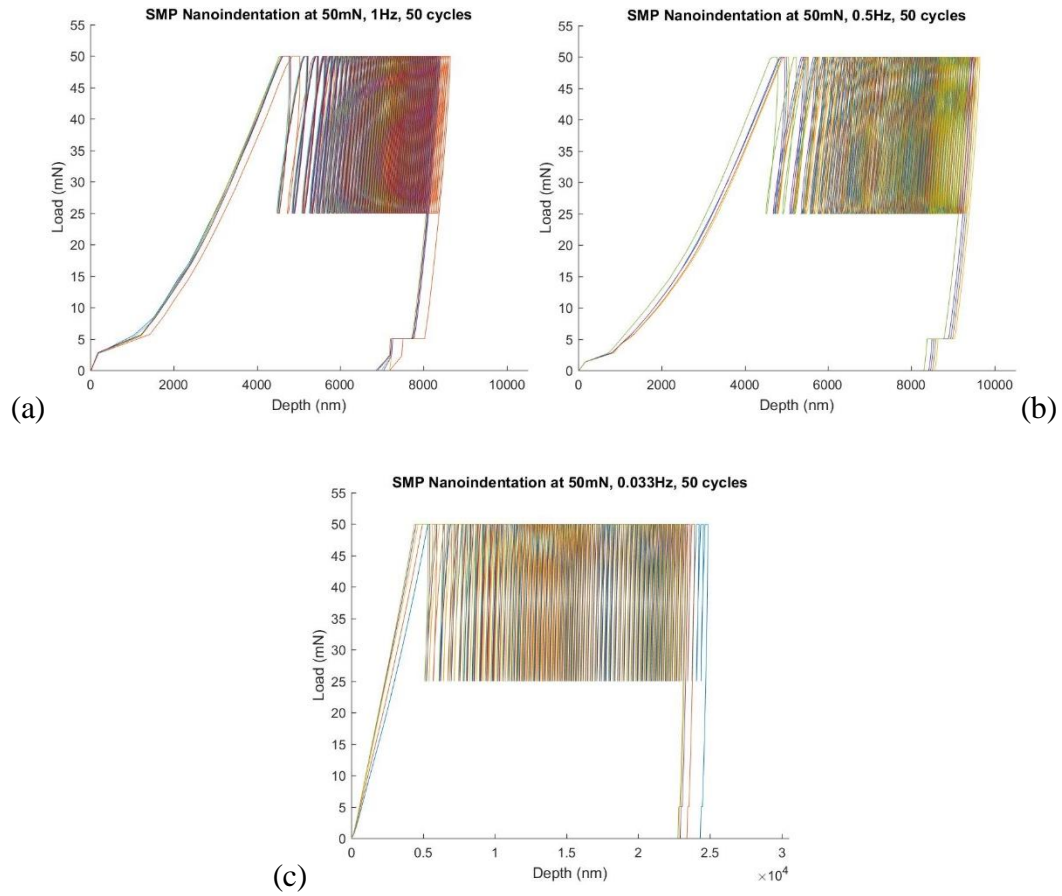


Figure E.5: SMP multiple cycle nanoindentation at 50mN and 50 cycles with varying frequencies of (a) 1Hz (7 curves), (b) 0.5Hz (5 curves), (c) 0.033Hz (5 curves).

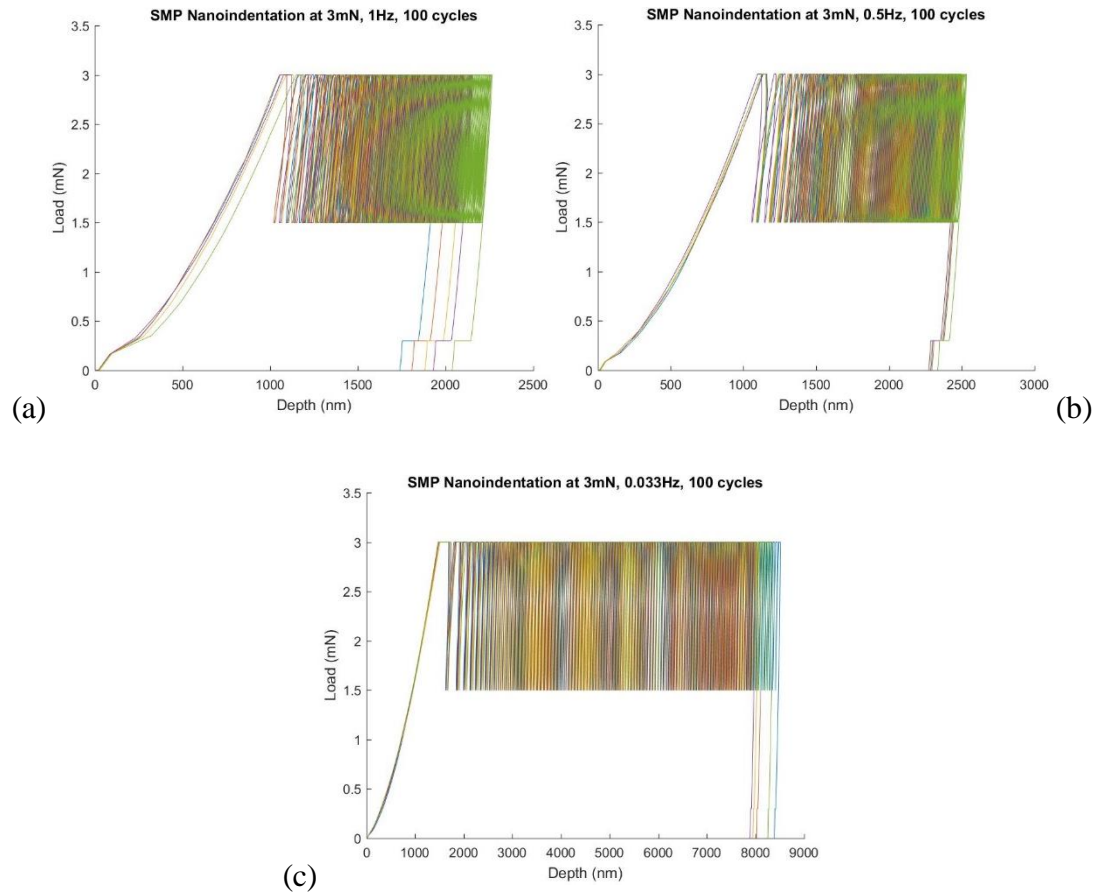


Figure E.6: SMP multiple cycle nanoindentation at 3mN and 100 cycles with varying frequencies of (a) 1Hz (5 curves), (b) 0.5Hz (5 curves), (c) 0.033Hz (5 curves).

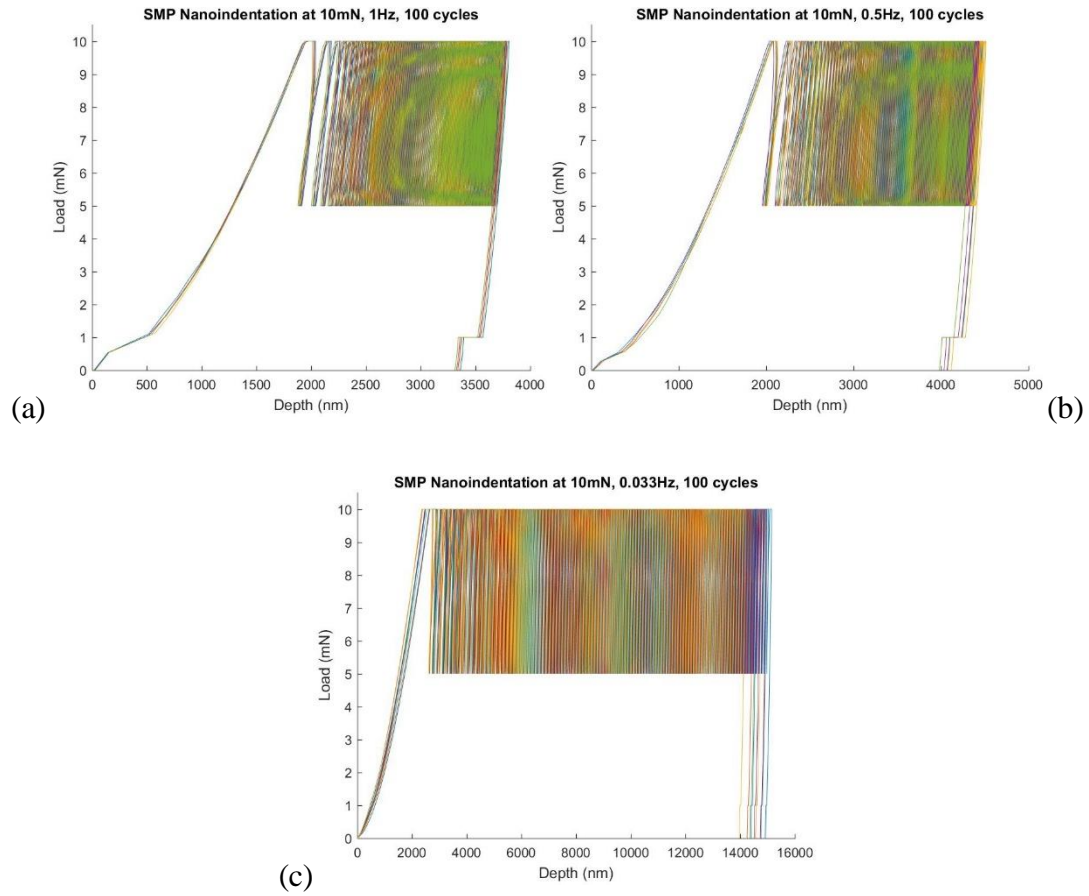


Figure E.7: SMP multiple cycle nanoindentation at 10mN and 100 cycles with varying frequencies of (a) 1Hz (5 curves), (b) 0.5Hz (5 curves), (c) 0.033Hz (10 curves).

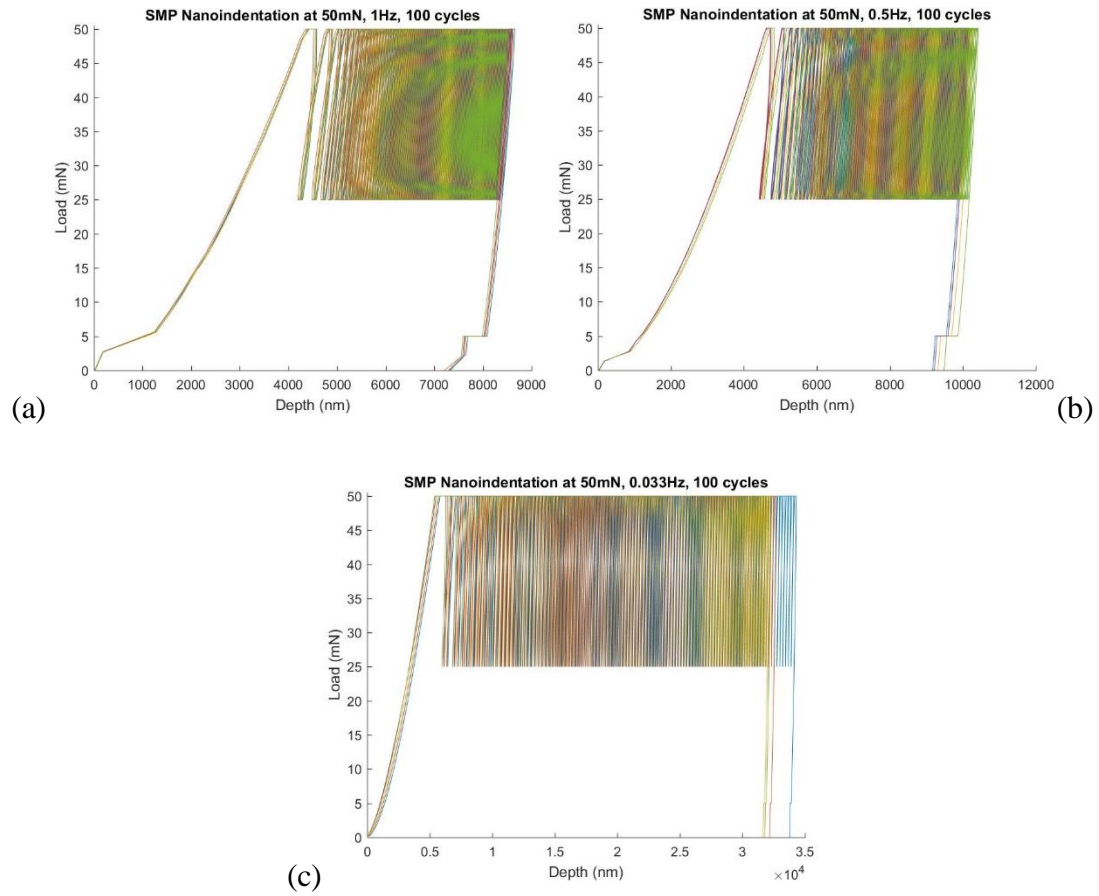


Figure E.8: SMP multiple cycle nanoindentation at 50mN and 100 cycles with varying frequencies of (a) 1Hz (5 curves), (b) 0.5Hz (5 curves), (c) 0.033Hz (10 curves).

REFERENCES

- [1] Quintanilla, J. "Microstructure and Properties of Random Heterogeneous Materials: a Review of Theoretical Results." *Polymer Engineering and Science* Vol. 39 No. 3 (1999): pp. 559-585.
- [2] Kabir, Reashad Bin and Ferdous, Nasrin. "Kevlar-The Super Tough Fiber." *International Journal of Textile Science* Vol. 1 No. 6 (2012): pp. 78-83. DOI 10.5923/j.textile.20120106.04.
- [3] Carmichael, Neil. "Linear Polydimethylsiloxanes CAS No. 63148-62-9 (Second Edition)." Technical Report No. JACC 55. European Centre for Ecotoxicology and Toxicology of Chemicals, Brussels, Belgium. 2011.
- [4] Lin, Chien-Hong, Yeh, Yi-Hsing, Lin, Wen-Ching, and Yang, Ming-Chien. "Novel silicone hydrogel based on PDMS and PEGMA for contact lens application." *Colloids and Surfaces B: Biointerfaces* Vol. 123 (2014): pp. 986-994. DOI 10.1016/j.colsurfb.2014.10.053.
- [5] Lotters, J.C., Olthuis, W., Veltink P.H., and Bergveld, P. "The mechanical properties of the rubber elastic polymer polydimethylsiloxane for sensor applications." *J. Micromech. Microeng.* Vol. 7 No. 3 (1997): pp. 145-147. DOI 10.1088/0960-1317/7/3/017.
- [6] Mather, Patrick T., Luo, Xiaofan, and Rousseau, Ingrid A. "Shape Memory Polymer Research." *Annu. Rev. Mater. Res.* Vol. 39 (2009): pp. 445-471. DOI 10.1146/annurev-matsci-082908-145419.
- [7] Ratna, Debdatta and Karger-Kocsis, J. "Recent advances in shape memory polymers and composites: a review." *J Mater Sci* Vol. 43 No. 1 (2008): pp. 254-269. DOI 10.1007/s10853-007-2176-7.
- [8] Sokolowski, Witold, Metcalfe, Annick, Hayashi, Shunichi, Yahia, L'Hocine, and Raymond, Jean. "Medical applications of shape memory polymers." *Biomed. Mater.* Vol. 2 No. 1 (2007): pp. S23-S27. DOI 10.1088/1748-6041/2/1/S04.
- [9] Ge, Qi, Sakhaei, Amir Hosein, Lee, Howon, Dunn, Conner K., Fang, Nicholas X., and Dunn, Martin L. "Multimaterial 4D Printing with Tailorable Shape Memory Polymers." *Scientific Reports* Vol. 6 No. 31110 (2016): pp. 1-11. DOI 10.1038/srep31110.
- [10] Yang, Chen, Boorugu, Manish, Dopp, Andrew, Ren, Jie, Martin, Raymond, Han, Daehoon, Choi, Wonjoon, and Lee, Howon. "4D Printing Reconfigurable, Deployable and Mechanically Tunable Metamaterials." *Mater. Horiz.* (2019): DOI 10.1039/C9MH00302A.

- [11] Bhushan, Bharat. "Depth-sensing nanoindentation measurement techniques and applications." *Microsyst Technol* Vol. 23 No. 5 (2017): pp. 1595-1649. DOI 10.1007/s00542-017-3372-2.
- [12] Wierenga, P.E. and Franken, A.J.J. "Ultramicroindentation apparatus for the mechanical characterization of thin films." *Journal of Applied Physics* Vol. 55 No. 12 (1984): pp. 4244-4247. DOI 10.1063/1.333026.
- [13] Turla, Prashanth. "Updated Area Function Analysis for Nano Indentation of Micro Fibers." MS Thesis. Rutgers University, New Brunswick, NJ. 2017. DOI 10.7282/T3S185N6.
- [14] McAllister, Quinn P., Gillespie, John W. Jr. and VanLandingham, Mark R. "The sub-micron scale energy dissipative deformation mechanisms of Kevlar fibrils." *J Mater Sci* Vol. 48 No. 18 (2013): pp. 6245-6261. DOI 10.1007/s10853-013-7422-6.
- [15] McAllister, Quinn P. and Gillespie, John W. Jr. "Evaluation of the three-dimensional properties of Kevlar across length scales." *J. Mater. Res.* Vol. 27 No. 14 (2012): pp. 1824-1837. DOI 10.1557/jmr.2012.80.
- [16] Cole, Daniel P. and Strawhecker, Kenneth E. "An improved instrumented indentation technique for single microfibers." *J. Mater. Res.* Vol. 29 No. 9 (2014): pp. 1104-1112. DOI 10.1557/jmr.2014.83.
- [17] Bencomo-Cisneros, J.A., Tejeda-Ochoa, A., García-Estrada, J.A., Herrera-Ramírez, C.A., Hurtado-Macías, A., Martínez-Sánchez, R., and Herrera-Ramírez, J.M. "Characterization of Kevlar-29 fibers by tensile tests and nanoindentation." *Journal of Alloys and Compounds* Vol. 536 No. 1 (2012): pp. S456-S459. DOI 10.1016/j.jallcom.2011.11.031.
- [18] Kawabata, S. "Measurement of the Transverse Mechanical Properties of High-performance Fibres." *J. Text. Inst.* Vol. 81 No. 4 (1990): pp. 432-447.
- [19] Wollbrett-Blitz, Judith, Joannès, Sébastien, Bruant, Rémi, Le Clerc, Christophe, De La Osa, Marc Romero, Bunsell, Anthony, and Marcellan, Alba. "Multiaxial Mechanical Behavior of Aramid Fibers and Identification of Skin/Core Structure from Single Fiber Transverse Compression Testing." *Journal of Polymer Science, Part B: Polymer Physics* Vol. 54 No. 3 (2015): pp. 374-384. DOI 10.1002/polb.23763.
- [20] Fisher-Cripps, Anthony C. "The sharpness of a Berkovich indenter." *J. Mater. Res.* Vol. 25 No. 5 (2010): pp. 927-934. DOI 10.1557/JMR.2010.0111.

- [21] Carillo, Fernando, Gupta, Shikha, Balooch, Mehdi, Marshall, Sally J., Marshall, Grayson W., Pruitt, Lisa, and Puttlitz, Christian M. "Nanoindentation of polydimethylsiloxane elastomers: Effect of crosslinking, work of adhesion, and fluid environment on elastic modulus." *J. Mater. Res.* Vol. 20 No. 10 (2005): pp. 2820-2830. DOI 10.1557/JMR.2005.0354.
- [22] Maji, Debashis and Das, Soumen. "Atomic force microscopy and nanoindentation investigation of polydimethylsiloxane elastomeric substrate compliancy for various sputtered thin film morphologies." *J Biomed Mater Res A* Vol. 106 No. 3 (2017): pp. 725-737. DOI 10.1002/jbm.a.36283.
- [23] Saha, Ranjana and Nix, William D. "Effects of the substrate on the determination of thin film mechanical properties by nanoindentation." *Acta Materialia* Vol. 50 No. 1 (2002): pp. 23-38. DOI 10.1016/S1359-6454(01)00328-7.
- [24] Chudoba, T. and Richter, F. "Investigation of creep behaviour under load during indentation experiments and its influence on hardness and modulus results." *Surface and Coatings Technology* Vol. 148 No. 2-3 (2001): pp. 191-198. DOI 10.1016/S0257-8972(01)01340-8.
- [25] Rho, Jae-Young and Pharr, G.M. "Effects of drying on the mechanical properties of bovine femur measured by nanoindentation." *Journal of Materials Science* Vol. 10 No. 8 (1999): pp. 485-488.
- [26] Oliver, W.C. and Pharr, G.M. "An improved technique for determining hardness and elastic modulus using load and displacement sensing indentation experiments." *J. Mater. Res.* Vol. 7 No. 6 (1992): pp. 1564-1583. DOI 10.1557/JMR.1992.1564.
- [27] Doerner, M.F. and Nix, W.D. "A method for interpreting the data from depth-sensing indentation instruments." *J. Mater. Res.* Vol. 1 No. 4 (1986): pp. 601-609. DOI 10.1557/JMR.1986.0601.
- [28] Schwarzer, N. "The extended Hertzian theory and its uses in analyzing indentation experiments." *Philosophical Magazine* Vol. 86 No. 33-35 (2006): pp. 5179-5197. DOI 10.1080/14786430600690507.
- [29] Vlassak, Joost J. and Nix, W. D. "Measuring the elastic properties of anisotropic materials by means of indentation experiments." *J. Mech. Phys. Solids* Vol. 42 No. 8 (1994): pp. 1223-1245. DOI 10.1016/0022-5096(94)90033-7.
- [30] Nano Test User Manual. *Micro Materials Excellence in Nano-mechanics*. (2015)
- [31] Alisafaei, F. and Han, Chung-Souk. "Indentation Depth Dependent Mechanical Behavior in Polymers." *Advances in Condensed Matter Physics* Vol. 2015 No. 391579 (2015) pp. 1-20. DOI 10.1155/2015/391579.

- [32] Hardiman, M., Vaughan, T.J., and McCarthy, C.T. "The effects of pile-up, viscoelasticity and hydrostatic stress on polymer matrix nanoindentation." *Polymer Testing* Vol. 52 (2016): pp. 157-166. DOI 10.1016/j.polymertesting.2016.04.003.
- [33] Han, Chung-Souk. "Indentation Size Effect in Polymers." *Advances in Materials Science Research* Vol. 10 No. 15 (2011): pp. 393-413.
- [34] Briscoe, B.J., Fiori, L., and Pelillo, E. "Nano-indentation of polymeric surfaces." *J. Phys. D: Appl. Phys.* Vol. 31 No. 19 (1998): pp. 2395-2405. DOI 10.1088/0022-3727/31/19/006.
- [35] Bandyopadhyay, P.P., Chicot, D., Kumar, C.S., Decoopman, X., and Lesage, J. "Influence of sinking-in and piling-up on the mechanical properties determination by indentation: A case study on rolled and DMLS stainless steel." *Materials Science & Engineering A* Vol. 576 (2013): pp. 126-133. DOI 10.1016/j.msea.2013.03.081.
- [36] Cheng, Yang-Tse and Cheng, Che-Min. "Scaling approach to conical indentation in elastic-plastic solids with work hardening." *Journal of Applied Physics* Vol. 84 No. 3 (1998): pp. 1284-1291. DOI 10.1063/1.368196.
- [37] Qu, Zhaoliang, Pei, Yongmao, He, Rujie, and Fang, Daining. "Investigation of Pile-Up Behavior for Thermal Barrier Coatings Under Elevated-Temperature Indentation." *Journal of Applied Mechanics* Vol. 83 No. 4 (2016): pp. 1-6. DOI 10.1115/1.4032467.
- [38] Swadener, J.G., George, E.P., and Pharr G.M. "The correlation of the indentation size effect measured with indenters of various shapes." *Journal of the Mechanics and Physics of Solids* Vol. 50 No. 4 (2002): pp. 681-694. DOI 10.1016/S0022-5096(01)00103-X.
- [39] Fischer-Cripps, Anthony C. "Chapter 2 Nanoindentation Testing." *Nanoindentation*. Springer-Verlag, New York (2011): pp. 21-37.
- [40] TI 750 Ubi User Manual, Hysitron. Revision 9.2.0311.
- [41] Sakharova, N.A, Fernandes, J.V., Antunes, J.M., and Oliveira, M.C. "Comparison between Berkovich, Vickers, and conical indentation tests: A three-dimensional numerical simulation study." *International Journal of Solids and Structures* Vol. 46 No. 5 (2009): pp. 1095-1104. DOI 10.1016/j.ijsolstr.2008.10.032.
- [42] Raju, Hermise and Pelegri, Assimina A. "Experimental Investigation of Transverse Mechanical Properties of High-Performance Kevlar KM2 Single Fiber." *ASME 2017 International Mechanical Engineering Congress and Exposition. IMECE2017-71724*: pp. V014T11A045. Tampa, Florida, November 3-9, 2017. DOI 10.1115/IMECE2017-71724.

- [43] Wang, Zhixin, Volinsky, Alex A., Gallant, Nathan D. "Nanoindentation Study of Polydimethylsiloxane Elastic Modulus Using Berkovich and Flat Punch Tips." *Journal of Applied Polymer Science* Vol. 132 No. 5 (2014): pp. 1-7. DOI 10.1002/app.41384.
- [44] Safranski, David L. and Gall, Ken. "Effect of chemical structure and crosslinking density on the thermo-mechanical properties and toughness of (meth)acrylate shape memory polymer networks." *Polymer* Vol. 49 No. 20 (2008): pp. 4446-4455. DOI 10.1016/j.polymer.2008.07.060.
- [45] Wang, J.S., Zheng, X.J., Zheng, H., Zhu, Z., and Song, S.T. "Evaluation of the substrate effect on indentation behavior of film/substrate system." *Applied Surface Science* Vol. 256 No. 20 (2010): pp. 5998-6002. DOI 10.1016/j.apsusc.2010.03.108.
- [46] Jiang, Wu-Gui, Feng, Xi-Qiao, and Su, Jian-Jun. "Effect of surface roughness on nanoindentation test of thin films." *Engineering Fracture Mechanics* Vol. 75 No. 17 (2008): pp. 4965-4972. DOI 10.1016/j.engfracmech.2008.06.016.
- [47] Jiroušek, Ondřej, Kytýr, Dan, Zlámál, Petr, Doktor, Tomáš, Šepitka, Josef, and Lukeš, Jaroslav. "Use of Modulus Mapping Technique to Investigate Cross-sectional Material Properties of Extracted Single Human Trabeculae." *Chem. Listy* Vol. 106 (2012): pp. 442-445.
- [48] Cheng, Ming, Chen, Weinong, and Weerasooriya, Tusit. "Experimental investigation of the transverse mechanical properties of a single Kevlar® KM2 fiber." *International Journal of Solids and Structures* Vol. 41 No. 22-23 (2004): pp. 6215-6232. DOI 10.1016/j.ijsolstr.2004.05.016.
- [49] Muhammed, Luay and Ismaeel, Luay. "Effect of Shear Modular Ratio (G_F / G_M) and Transverse Shear Modulus on the Twisting Strength of a Fiber- Reinforced Composite Rod." *The Iraqi Journal for Mechanical and Material Engineering* Vol. 13 No. 1 (2013): pp. 129-143.
- [50] Şahin, Korhan, Clawson, Jan Kenneth, Singletary, James, Horner, Suzanne, Zheng, James, Pelegri, Assimina, and Chasiotis, Ioannis. "Limiting role of crystalline domain orientation on the modulus and strength of aramid fibers." *Polymer* Vol. 140 (2018): pp. 96-106. DOI 10.1016/j.polymer.2018.02.018.
- [51] Hadley, D.W., Ward, I.M., and Ward, J. "The transverse compression of anisotropic fibre monofilaments." *Proceedings of the Royal Society A Mathematical Physical and Engineering Sciences* Vol. 285 No. 1401 (1965): pp. 275-286.
- [52] Pinnock, P.R., Ward, I.M., and Wolfe, J.M. "The compression of anisotropic fibre monofilaments. II." *Proceedings of the Royal Society A Mathematical Physical and Engineering Sciences* Vol. 291 No. 1425 (1966): pp. 267-278.

- [53] Singletary, J., Davis, H., and Song, Y. "The transverse compression of PPTA fibers Part II Fiber transverse structure." *Journal of Materials Science* Vol. 35 No. 3 (2000): pp. 583-592. DOI 10.1023/A:1004716108638.
- [54] Singletary, J. and Davis, H. "The transverse compression of PPTA fibers Part I Single fiber transverse compression testing." *Journal of Materials Science* Vol. 35 No. 3 (2000): pp. 573-581. DOI 10.1023/A:1004764024568.
- [55] Roenbeck, Michael R., Sandoz-Rosado, Emil J., Cline, Julia, Wu, Vincent, Moy, Paul, Afshari, Mehdi, Reichert, David, Lustig, Steven R., and Strawhecker, Kenneth E. "Probing the internal structures of Kevlar® fibers and their impacts on mechanical performance." *Polymer* Vol. 128 (2017): pp. 200-210. DOI 10.1016/j.polymer.2017.09.039.
- [56] Pritchard, Robyn H., Lava, Pascal, Debruyne, Dimitri, and Terentjev, Eugene M. "Precise determination of the Poisson ratio in soft materials with 2D digital image correlation." *Soft Matter* Vol. 9 No. 26 (2013): pp. 6037-6045. DOI 10.1039/c3sm50901j.
- [57] Costas, Charitidis. "Nanoscale Deformation and Nanomechanical Properties of Soft Matter Study Cases: Polydimethylsiloxane, Cells and Tissues." *ISRN Nanotechnology* Vol. 2011 No. 719512 (2011): pp. 1-13. DOI 10.5402/2011/719512.
- [58] Dragatogiannis, D.A., Tsikourkitoudi, V.P., and Charitidis, C.A. "Analysis of nanoindentation creep of polydimethylsiloxane." *Plastics, Rubber, and Composites* Vol. 41 No. 8 (2012): pp. 358-363. DOI 10.1179/1743289811Y.0000000062.
- [59] Li, Xiaodong and Bhushan, Bharat. "A review of nanoindentation continuous stiffness measurement technique and its applications." *Materials Characterization* Vol. 48 No. 1 (2002): pp. 11-36. DOI 10.1016/S1044-5803(02)00192-4.